Analysis of Multi-Layered Materials Under High Velocity Impact Using CTH

THESIS

Jason K. Lee, Captain, USAF

AFIT/GAE/ENY/08-M19

DEPARTMENT OF THE AIR FORCE
AIR UNIVERSITY

AIR FORCE INSTITUTE OF TECHNOLOGY

Wright-Patterson Air Force Base, Ohio

The views expressed in this thesis are those of the author and do not reflect the official policy or position of the United States Air Force, Department of Defense, or the United States Government.

AFIT/GAE/ENY/08-M19

Analysis of Multi-Layered Materials Under High Velocity Impact Using CTH

THESIS

Presented to the Faculty

Department of Aeronautics and Astronautics Engineering

Graduate School of Engineering and Management

Air Force Institute of Technology

Air University

Air Education and Training Command

In Partial Fulfillment of the Requirements for the

Degree of Master of Science in Aeronautical Engineering

Jason K. Lee, B.S.A.E.

Captain, USAF

March 2008

AFIT/GAE/ENY/08-M19

Analysis of Multi-Layered Materials Under High Velocity Impact Using CTH

Jason K. Lee, B.S.A.E.
Captain, USAF

Approved:

//signed//	17 Mar 2008
Dr. Anthony Palazotto (Chairman)	date
//signed//	17 Mar 2008
Dr. Larry Byrd (Member)	date
//signed//	17 Mar 2008
Dr. Robert Brockman (Member)	date

Abstract

Multi-layer armor containing ceramic and metallic layers has become more common in the past two decades. Typically, ceramics have high compressive strength which combined with their low density make them highly desirable for armor applications. This research effort numerically simulates high velocity impact of cylindrical projectiles on multi-layer metallic and ceramic targets of finite thickness. The impact of the projectile occurs normal to the surface of the target. The projectiles used are made of either S7 tool steel or tungsten. The targets consist of either rolled homogeneous armor, 4340 steel and boron carbide ceramic or rolled homogeneous armor and boron carbide ceramic. The Eulerian hydrocode CTH, ideal for studying cases of gross global and local deformation, is used to perform an axisymmetric analysis of the projectile and the target. The Johnson-Holmquist constitutive model (JH-2) for brittle materials is used for the ceramic layers, and the Johnson-Cook constitutive model is used for the metallic layers. Various arrangements of ceramic and metallic layers were simulated over a range of velocities to quantitatively determine ballistic limits. Comparison of the ballistic limits for each configuration will determine which ceramic-metal lay-up arrangement is optimal for resisting penetration of the given projectile. A variety of options in CTH are taken into account in this research. This research shows that replacing multiple metallic target layers with B_4C ceramic decreases the resistance of the target to the penetration of the projectile for a target of given thickness.

Acknowledgements

First, I would like to thank my Lord Jesus through whom all things are possible. I would like to express my sincere appreciation for all the support and guidance of my academic and research advisor, Dr. Anthony Palazotto. Additionally, I would like to show my gratitude to the members of my thesis committee, Dr. Larry Byrd of AFRL/RZPS and Dr. Robert Brockman of the University of Dayton, for their time and patience. I am very grateful for all the help with CTH that I have received from Dave Crawford of Sandia National Laboratories. I greatly appreciate all the help that Maj Chad Hale, Capt Reid Larson and Capt Hugh Gardenier have provided me throughout this effort. I am extremely thankful to my parents for all their hard work and sacrifice in life that have allowed me to have this opportunity. Last but not least, I want to thank my wife for her understanding, patience, love and continued support. This thesis has been sponsored by Dr. Kirk Vanden of the Air Force Research Laboratory's Munitions Directorate (AFRL/RWAC) located at Eglin AFB, FL.

Jason K. Lee

Table of Contents

Page

Page

List of Figures

List of Tables

List of Symbols

Symbol		Page
KE	kinetic energy per unit mass	36
A_n	area of the layer	41
σ_I	stress of incident wave	41
σ_R	stress of reflected wave	41
σ_T	stress of transmitted wave	41
ρc	acoustic impedance	41
V	volume	44
F	applied force	44
m	mass	44
P	pressure	46
V_{sp}	specific volume $= 1/\rho$	46
Γ	Grüneisen parameter	47
P_H	Hugoniot pressure	47
E_H	Hugoniot energy	47
T_H	Hugoniot temperature	47
C_v	specific heat	47
ρ_0	initial density	47
P_0	initial pressure	47
E_0	initial energy	47
U_s	shock wave velocity	47
P_T	transition pressure	48
ρ_T	transition density	48
β_T	bulk modulus in the transition region	48
A_T	derivative of the transition pressure with respect to T	48
A_λ	derivative of the transition pressure with respect to λ	48
λ	mass fraction of phase two	48
A_{jc}	J-C viscoplastic model coefficient	50
B_{jc}	J-C viscoplastic model coefficient	50

Symbol		Page
C_{jc}	J-C viscoplastic model coefficient	50
N_{jc}	J-C viscoplastic model coefficient	50
M_{jc}	J-C viscoplastic model coefficient	50
ϵ_p	equivalent plastic strain	50
$\dot{\epsilon}_p^*$	dimensionless plastic strain-rate	50
T^*	homologous temperature	50
T_{abs}	absolute temperature	50
T_{room}	room temperature	50
T_{melt}	melting temperature	50
σ^*	normalized flow stress	51
P^*	normalized pressure	51
σ_{HEL}	flow stress at the Hugoniot elastic limit (JH-2 parameter)	51
P_{HEL}	pressure at the Hugoniot elastic limit (JH-2 parameter)	51
T	min pressure that the ceramic can maintain (JH-2 parameter)	51
D_{jh}	scalar damage variable in JH-2 ceramic model	51
σ_i^*	intact normalized flow stress	51
σ_f^*	fractured normalized flow stress	51
$\dot{\epsilon}_p$	equivalent plastic strain-rate	51
A_{jh}	JH-2 ceramic model coefficient	51
B_{jh}	JH-2 ceramic model coefficient	51
C_{jh}	JH-2 ceramic model coefficient	51
M_{jh}	JH-2 ceramic model coefficient	51
N_{jh}	JH-2 ceramic model coefficient	51
SFMAX	JH-2 ceramic model coefficient	51
ϵ_{pf}	plastic strain at fracture	52
D_1	JH-2 damage model constant	52
D_2	JH-2 damage model constant	52
ρ_{ref}	reference density	52

Symbol		Page
ΔP	bulking pressure	52
G	shear modulus	53
W_d	elastic strain energy due to deviatoric stress	53
$\dot{\epsilon}$	deviatoric strain-rate	54

List of Abbreviations

Analysis of Multi-Layered Materials Under High Velocity Impact Using CTH

I. Introduction

1.1 Background

The Air Force has a significant interest in the area of high velocity impact phenomena. The Air Force Research Laboratory (AFRL) Munitions Directorate at Eglin AFB is constantly performing research using computer simulation and experimental testing to gain knowledge and understanding of this extensive field of study.

The advancement of armor has paralleled the advancement of projectiles [24]. Development of more lethal projectiles is progressing all the time, which is one reason it is necessary to continue to develop more resistant armor that can defeat these threats. With ordinary steel armor, its weight as a result of the armor thickness necessary to defeat these more potent projectiles is much to large to be practical for use whether for body armor or vehicle armor [49].

Ceramic materials are being used in more areas everyday from armor to engine turbine blades. They are usually very strong in compression and weak in tension. Ceramics also tend to be very brittle, but they can have significant strength after fracture when under compression [18, 34]. They are ideal for weight-saving armor systems thanks to their low material density and high compressive strength [31].

1.2 Previous Research

Usually ceramic armor consists of some type of metallic reinforcement on the top and bottom of the ceramic making it basically a layered target. Tedesco and Landis [48] showed that using different materials in layered structures could be beneficial against impact due to blast loadings. They numerically analyzed layered systems to determine how effectively they provide protection against blast effects of conventional

weaponry. A few different layered arrangements were considered. The results indicated that layered media greatly alter the propagation characteristics of stress waves. They showed that the right combination of high and low impedance materials can substantially enhance attenuation of stress waves. The implication here is that the use of layered structures for building protective shelters can reduce and even eliminate interior spalling of shelter walls that result from blast effects.

On the other hand, Zukas and Scheffler [56] and Zukas [55] considered the difference of the effect of projectile impact on a monolithic target compared with the equivalent multi-layered target of the same material through numerical simulation. They determined that layering thin and intermediate thickness targets dramatically weakens them. They also noted that Eulerian hydrocode results can be sensitive to the algorithms used to handle the material interfaces.

Rosenberg and Dekel [36] evaluated the relation between the penetration capability of long rods and their length-to-diameter ratio. This study involves the impact of steel and tungsten projectiles into hardened steel targets. The Johnson-Cook constitutive model was used for the strength model for the target and projectile materials. Both the experimentation and simulation data showed a decrease in the normalized penetration of approximately 15 percent when the length-to-diameter ratio was increased from 10 to 20. A similar result was observed for an increase in length-to-diameter ratio from 20 to 30.

In a study by Gupta and Madhu [14], impact experiments were performed of armor-piercing projectiles striking single and layered targets made of rolled homogeneous armor and aluminum both normal and oblique to the target surface. The striking velocities of the projectiles ranged from 800–880 m/s. The thickness of the targets varied from 4.7–40 mm, while the ratio of the plate thickness to the projectile diameter varied from 0.75–6.5 for single plates and up to 13 for layered plates. This research provides the angles of obliquity for the impacts, the incident and residual velocities and observations of the target damage. Gupta and Madhu determine the

thickness of the targets that yield an incident velocity equal to the ballistic limit, t^*. The ballistic limit is the minimum velocity required for a particular projectile to completely penetrate through a target. The effect of various parameters, such as the target thickness and material, on the residual velocity and t^* are also considered. They also developed relationships to calculate the residual velocity for targets where the thickness is less than t^*. The residual velocity is the remaining velocity of the projectile after it has perforated the target.

There have been many studies done dealing with impact of ceramic targets in the past couple of decades, especially for the use of ceramic armors. In many cases, ceramic armor not only contains reinforcement layers, it also can consist of a casing that completely confines the ceramic. Subramanian and Bless [46], Orphal, et al (1996) [30] and Orphal, et al (1997) [29] studied high velocity impact of tungsten long-rod projectiles into confined AD995 alumina, aluminum nitride and boron carbide targets, respectively. They all characterized the performance of their respective ceramic experimentally using the method of reverse ballistic testing. The ceramic target tested by Subramanian and Bless was cylindrical and had a diameter 30 times the diameter of the projectile. The range of velocities for which the experiments were carried out were 1.5 to 3.5 km/s. In these experiments, radiographs allowed them to obtain the consumption velocity of the penetrator, penetration velocity into the ceramic, and depth of penetration. Subramanian and Bless found that the primary penetration approached 75 percent of the hydrodynamic limit, and the secondary penetration was very small. The target strength, R_t, which is a useful way to express the ability of the target to resist penetration, was reduced from 90 kbar at ordinance velocity to approximately 70 kbar at 3.5 km/s. R_t also was decreased by 30 percent to 50 percent in the tests where the target diameter to projectile diameter ratio was reduced to 15.

Orphal, et al (1996) measured the penetration of tungsten projectiles into aluminum nitride targets for velocities from 1.5 to 4.5 km/s. Orphal, et al (1997) measured the penetration of tungsten projectiles into boron carbide targets for velocities

from 1.5 to 5.0 km/s. The projectiles for all of these experiments had length-to-diameter ratios that ranged from 15 to 20. Experimental measurements taken from X-rays were used to obtain the penetration velocity and the consumption velocities. The results of these experiments showed that target penetration and the rod consumption rate were nearly constant over the entire range of impact velocities. For the range of the impact velocities, the primary penetration was significantly less than ideal hydrodynamic penetration, while the total penetration was equal to or slightly greater than the ideal hydrodynamic penetration for impact velocities greater than about 4 km/s. The mass efficiency for the aluminum nitride and boron carbide targets decreases with increasing impact velocity.

A research effort by Rajendran and Grove [34] modeled the impact behavior of silicon carbide, boron carbide and titanium diboride. Their main purpose was to determine the preliminary ceramic constants for the advanced microphysical ceramic mode1 developed by Rajendran for these three ceramics using experimental data from Kipp and Grady. Once the constants were determined, the advanced ceramic model was used to determine the high velocity wave profiles. They were able to successfully predict plate impact experiments at a velocity around 2.2 km/s using the constants they determined from one-dimensional experiments at a velocity around 1.5 km/s. This microphysical model is capable of simulating the impact behavior of intact ceramics until pulverization occurs.

Grace and Rupert [13] analyzed experimental data from long-rod penetration of semi-infinite ceramic and metallic targets at velocities up to 4500 m/s. The projectiles were made of pure tungsten and have length-to-diameter ratios of 15 and 20. Reverse ballistic tests were performed impacting the rods with confined aluminum nitride, alumina and an aluminum target. Through the entire penetration process, the penetration rates were nearly constant for all impact velocities considered. The depths of penetration were in good agreement with the expected levels based on the measured penetration velocities and rod erosion rates. Significantly more penetration resulted in the aluminum nitride and aluminum targets for impact velocities above

2000 m/s. The analysis was in good agreement with the primary penetration for the aluminum nitride and the aluminum targets. Primary penetration is penetration of the projectile into the target as a result of the interface pressures surpassing the material strength of the projectile and target. This results in a fluid like process where a cavity is produced in the target and erosion of the projectile occurs.

Rosenberg, et al [40] performed a series of two-dimensional simulations consisting of small scale tungsten alloy projectiles striking confined alumina targets. These simulations were then compared to experimental data. These simulations and experiments were accomplished at velocities ranging from 1.25 to 3.0 km/s. The goal of this research was to quantify the ballistic efficiency of the ceramic tiles using the Eulerian processor of the PISCES 2-D ELK code. The experimental results consisted of both the depth of penetration into a thick steel backing and X-ray shadowgraphs during the penetration process. They also examined the performance of the ceramic as it related to the thickness and lateral dimensions. Ultimately, they found that the differential ballistic efficiency of alumina tiles was virtually independent of striking velocity and the ceramic thickness for the velocities and thicknesses considered. They also used a simplified version of the Johnson-Holmquist ceramic model which they found was fairly adequate to account for most of the data.

In an effort by Rosenberg and Dekel [38], two-dimensional numerical simulations were performed to determine the effect that material properties have on the terminal ballistics of long-rod penetrators. This research centered on the material properties of the projectile. They evaluated this effect for a large range of values for nearly all the relevant projectile parameters. The parameters they considered were comprised of the compressive and tensile strengths, elastic moduli, melting temperatures and the maximum equivalent plastic strain (failure strain) of the rod material. Nearly all of the simulations consisted of a tungsten alloy projectile impacting a semi-infinite steel target. When considering depth of penetration, the mechanical and thermal softening mechanisms had the most effect, while the modulus of elasticity and spall strength had very little effect.

In yet another study, Rosenberg and Dekel [37] investigated the role of deformed nose profile on the ballistic performance of long rods into a target. They accomplished this through the use of two-dimensional, axisymmetric numerical simulations and normal perforation experiments. The residual penetrators were recovered from the experiments and examined. Impact of rigid tungsten alloy rods with five different nose shapes were simulated. Three rod materials were used for the normal impact experiments which were a tungsten alloy rod, a copper rod and a titanium alloy rod. After perforation of the finite thickness target, the nose shapes of the residual penetrators were very different from each other. They found from experimentation that adiabatic shear failure sharpens the titanium alloy rod noses along planes oriented 45 percent to the rod axis. At high impact velocities the sharpening causes a wedge shaped nose to be obtained. A mushroom shaped nose is produced for the copper long rods where the nose shape of the tungsten alloy rods lies somewhere in between. They found that the simulations of the projectiles with different nose shapes resulted in penetration depths that varied by as much as a factor of three between the two extremes; therefore, significant differences in their depths of penetration can result due to minimal variations in the nose shapes of long-rods.

In an attempt to better understand secondary penetration of long rods, Rosenberg and Dekel [39] performed numerical simulations using PISCES 2-D ELK. Secondary penetration is the penetration of the projectile that results from the expansion of the cavity due to the energy that is trapped in the target. These simulations dealt with the rod impact velocity, rod length-to-diameter, as well as the densities and strengths of rod and target material. They showed that the entire range for these parameters is not covered by the semi-empirical formulations. According to their work, the main influence on the secondary penetration value is due to the strength of the rod. These values depend greatly on the rod length-to-diameter and the target strength.

Westerling, Lundberg and Lundberg [49] examined the influence of impact velocity and confinement on the resistance of boron carbide targets to penetration of

tungsten long-rod projectiles. They varied the striking velocity of the projectile as well as the thickness of the steel that confined the ceramic target. This was carried out for both experimentation and numerical simulation. They performed all the simulations using the Lagrangian code AUTODYN-2D. They determined that at high-impact velocities the relationship of the impact velocity versus the penetration velocity was approximately equal. Their simulation results matched fairly well with the experimental results.

Chocron, et al [7] performed reverse ballistic experiments where silicon carbide cylinders impacted gold long rods to study the effect of failure kinetics in ceramic penetration. The velocity range which these experiments and simulations were accomplished was 3.5 to 4.5 km/s. Penetration velocity was calculated from the experimental measurements. Even though some of the early experiments impacted off-centered due to the dynamics of the gas gun barrel and sabot, the data appeared to be in good agreement with centered impact. During acceleration of the projectile through the gas gun barrel, the sabot is used to align, support and protect the projectile. CTH was used to numerically simulate the experiments in order to investigate and to quantify the effects of the off-centered impact and the influence of lateral confinement as a function of impact velocity for the ceramic targets. From the computational model, it was observed that the sensitivity to the closeness of the lateral boundary decreased as the striking velocity was increased. Using the model, they also observed that even for impacts near the boundary of the target, the penetration velocity could not be distinguished from centered impact results from the experiments.

Lynch, et al [21] carried out scale size experiments evaluating the effect that confinement has on the penetration of ceramic targets for velocities at 1.8 km/s and 2.6 km/s. These impact events consisted of tungsten alloy long-rod projectiles striking alumina (Al_2O_3) ceramic targets. Two different target configurations were experimented with. One consisted of steel lateral confinement, and the other had no lateral confinement. The outcome of the experiments indicates that the steel confinement performed slightly better in that it decreased the projectile's residual energy at both

velocities. Expressed in terms of impact energy of the penetrator, 60 percent was lost in the steel confined target, while 55–56 percent was lost in the target with no confinement at 2.6 km/s. This trend is also seen at a velocity of 1.8 km/s with 72–73 percent and 68 percent for the confined and unconfined targets, respectively.

When evaluating impact situations at various velocities, it is necessary to have a constitutive model that can provide reasonable results. The Johnson-Holmquist constitutive models are fairly accurate at predicting the behavior of ceramics. Templeton and Bishnoi [18] developed a constitutive model for aluminum nitride for large strain, high-strain rate and high-pressure applications. The Johnson-Holmquist II ceramic model was used, and the coefficients for the model were obtained using test data from the literature. A variety of plate impact and ballistic experiments were simulated using the Johnson-Holmquist II ceramic model constants. The results of the simulation compared well with experimentation. The results were then used to validate the model.

Quan, et al [31] validated the Johnson-Holmquist I ceramic model including the failure parameters for silicon carbide by comparing experimental data and numerical simulations using AUTODYN. The tests consisted of normal and oblique impact of tungsten and molybdenum long-rod projectiles into a confined silicon carbide target. The results showed good agreement between the numerical predictions and the experimental data for normal and low obliquity impacts; however, some deviations occurred for higher obliquity imapct.

1.3 Problem Statement and Objectives

As discussed above, it is very desirable to develop a lightweight armor with the ability to resist penetration of high velocity projectiles. Due to the weakness of ceramics in tension, ceramic armor must contain some sort of backing material to prevent the large deflections that cause tensile failure. Basically, ceramic armor consists of a ceramic layer or layers bonded to metallic layers; therefore, it may be treated similarly to a multi-layer target.

This research uses the Eulerian hydrocode CTH to numerically simulate ballistic impact of a projectile on a variety of different targets. The first phase of the research adopted a problem from Zukas and Scheffler [56] and Zukas [55]. This problem consisted of creating and executing a multi-layer target simulation as a baseline for later comparison to the combined metallic and ceramic target. This problem consists of a projectile impacting multiple metallic layers that all consist of the same material. This problem is also beneficial to gain experience running multi-layer impact problems and determine the CTH parameters to use.

The next phase of the research was to reproduce the results from the research conducted by Westerling, Lundberg and Lundberg [49]. As mentioned above, their work consisted of long-rod projectiles impacting a confined ceramic target. The data obtained from the simulation of this problem was compared to the authors' results in an attempt to verify the CTH model and demonstrate the ability of CTH to handle this type of problem.

In the last portion of this research the goal was to characterize the behavior of a confined ceramic target when impacted by a hemispherical-nosed projectile. CTH was used to simulate impact of a projectile on a target made of a combination of metal and ceramic. The target consists of a metal layer above and below the ceramic material, as well as metallic sides that completely confine the ceramic. As mentioned earlier, ceramics are very strong in compression but also very weak in tension, so the confinement of the ceramic by the metal is used in an attempt to keep the ceramic in compression.

II. Characteristics of Impact Events

This chapter discusses the theory and background behind impact events in order to lay the foundation for what observations are expected from this research. The topics covered include but are not limited to penetration and perforation of projectiles, ballistic limit, failure modes, stress wave propagation and layered materials.

2.1 Introduction to Impact Phenomenon

Two features distinguish impact dynamics from the classical mechanics that involves rigid or deformable bodies under quasi-static loading. The first feature is the importance of inertia effects, which have to be taken into account in all governing equations based on the fundamental conservation laws of mechanics and physics [28]. Hydrodynamic pressure dominates the way solids behave during high velocity impact. Metals act basically like inviscid fluids at the very high pressures associated with impact in the high velocity regime. The material behavior under these conditions and under high loading rates have to be considered [20]. The role of stress wave propagation in the analysis of problems is the second feature. This includes the recognition that most impact events are transient phenomena where steady state conditions do not exist [28].

Solid materials have to deform in order to bear stress. It takes time and requires relative motion for compression to push particles closer together. When an unstressed plate is exposed instantaneously to a pressure, the pressure is initially supported completely by inertia. Then the first layer of particles move towards the second layer causing the compressive stress to intensify and accelerate the second layer at a growing rate. In the same fashion, the second layer acts to accelerate the third layer and so on. Once the stress between adjacent layers becomes equal to the applied pressure, relative motion ceases. At this point, the pressure is supported completely by the compression wave. Particle velocities and the state of stress and strain are changed as these waves propagate through materials. Wave fronts are only a few molecules thick and can be considered as discontinuities in most solid materials [28].

Impact dynamics can produce stress waves that vary greatly in velocity and intensity depending on the velocity at impact. For low impact velocities, the loading will cause stresses below the yield strength of the material, in turn generating elastic stress waves. In the case of high velocity impact, the resulting load intensity causes stresses that surpass the yield strength, which produces an elastic wave, followed by a slower moving plastic wave. A shock wave forms at impact velocities greater than the wave propagation velocity of the material [28]. Wave propagation in traditional applications may be considered to be instantaneous since it occurs so much faster than material deformation, such that when the load is applied, the entire domain is affected immediately. This is not necessarily the case in hypervelocity events where the material response gets close to or surpasses the wave velocity [20].

2.2 Penetration and Perforation

Various classical disciplines are involved in the study of impact phenomena. Many problems fall into the category of structural dynamics in the low-velocity regime ($<$ 250 m/s). For structural dynamics problems, local penetrations and the overall structural deformation are strongly coupled together. The geometry of the structure and the nature of the behavior of the material have a significant part in determining behavior under a transient load for impact well below the ballistic limit. The typical times for the loading and response to occur are on the order of milliseconds.

The structural response becomes secondary to the behavior of the material within a small area, typically 2-3 projectile diameters of the impact area, as the impact velocity increases (0.5-2 km/s). It is accurate to describe this phenomenon in terms of waves. At various phases of the impact process, the influences of velocity, geometry, material constitution, strain rate, localized plastic flow and failure can be observed. Inertia with the additional complexity of material failure dominate the behavior of solid projectiles and targets in this regime. Incremental elastic-plastic relationships are typically used to account for large, highly localized plastic flow. For

this velocity range, the typical times for the loading and response to occur are in the microsecond regime.

If the impact velocity (2-3 km/s) is increased even more, the localized pressures will surpass the material strength by an order of magnitude, effectively meaning that impacting solids can be handled as fluids at the early phases of impact. Only in the late stages of impact is material strength important. The behavior of the impacting bodies is dominated by the hydrodynamic pressure. Problems in this velocity regime are treated with an incremental elastic, perfectly-plastic model in which an accurate value for flow stress is obtained from dynamic experimentation. Spallation is a frequently encountered failure mechanism. Energy deposition takes place at such a high rate for extremely high velocities (> 12 km/s) that an explosive vaporization of colliding materials results. The effects here are dependent on the material thickness of the body being loaded [52, 53].

2.2.1 Physical Phenomenon in Impacting Solids. Consider the events that take place when a cylindrical rod with a hemispherical tip impacts a target. Upon impact of the projectile with the target surface, compressive stress waves are produced in both bodies. These compressive waves move either at the material sound speed, c, of the projectile and target for low velocity impacts or at the shock velocity for hypervelocity impacts. If the velocity of the rod is sufficiently high, relief waves will travel inward from the lateral free surfaces of the projectile and cross at the centerline. This generates a zone of high-tensile stress, which can cause brittle materials to fail. This is a two-dimensional state of stress for normal impacts; however, it is a three-dimensional state of stress for oblique impacts due to the asymmetric bending waves. The bending and tensile stresses can result in the projectile bending, breaking, eroding and ricocheting given the right combination of striking velocity, projectile geometry and material characteristics [52, 54].

In the target, a shear wave follows the initial compression wave. When the initial compressive wave reaches a free surface in the target, it is reflected as a tension

wave in order to satisfy the free surface boundary conditions. If both the tensile stress amplitude and its duration exceed the critical value for the material that makes up the target, material failure by various mechanisms can occur [52,54]. Figure 2.1 shows the effects of the different waves for a projectile impacting a target.

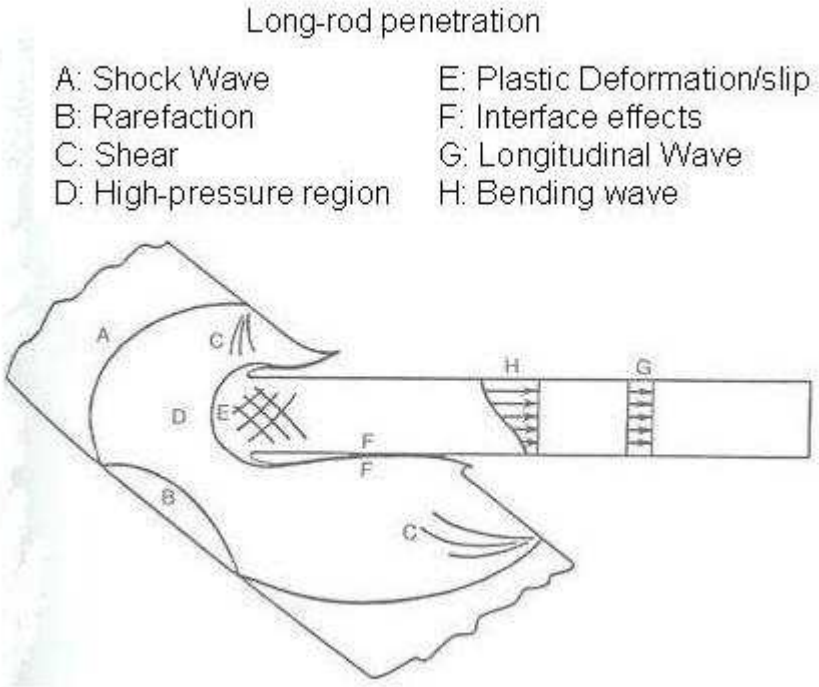

Figure 2.1: Wave Effects in Long-Rod Penetration [51, 54]

2.2.2 Characterization of Impact Events. There are numerous ways to characterize impact events: by incidence angle of impact, configuration and material characteristics of the projectile or the target, or the impact velocity. Figure 2.2 uses the striking velocity to describe the impact. It provides a short classification of impact events as a function of the impact velocity, v_0, and strain rate, $\dot{\epsilon}$. The impact-velocity ranges are only reference points, since deformation processes due to impact are functions of a long list of variables not just impact velocity [3].

Backman and Goldsmith define penetration as the entrance of a projectile into a target without passing all the way through the body. This results in the embedment of

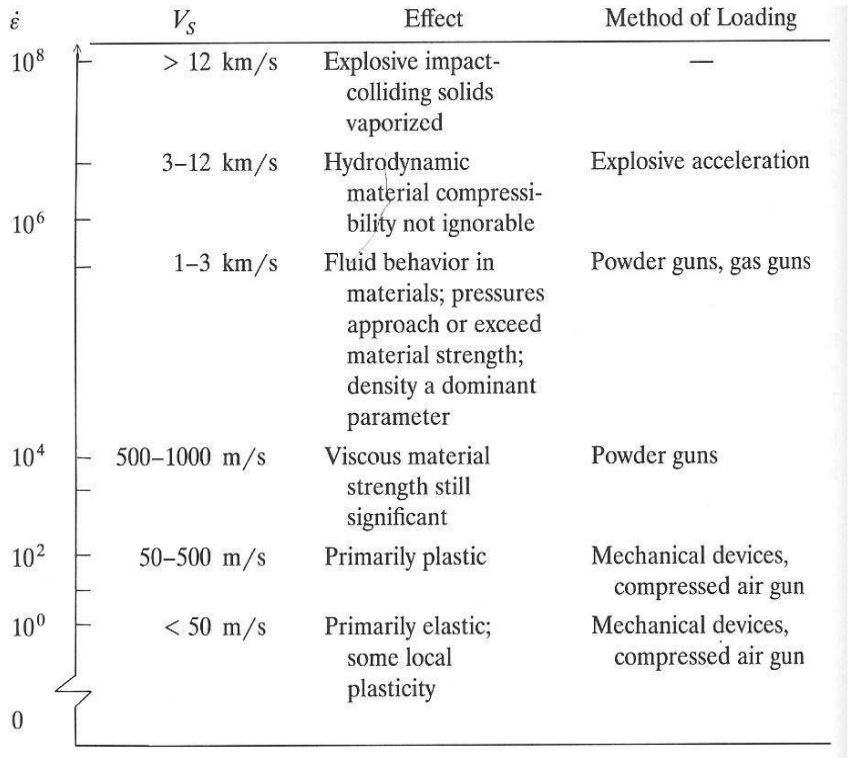

Figure 2.2: Classification of impact response by striking velocity [54]

the striker and the formation of a cavity. If the projectile pierces through the entire target, it is said to have perforated the target. A ricochet is when the projectile impacts the surface and then bounces back or penetrates the surface along a curved trajectory and emerges back through the impacted surface with a reduced velocity [3, 12]. Figure 2.3 is an example of a phase diagram depicting the behavior of a projectile impacting a target as functions of impact velocity and angle of obliquity. Many times both the projectile and the target will experience severe deformation after such an event. There are many types of problems that are of interest when dealing with kinetic energy impact phenomena, such as crashworthiness of vehicles, the design of lightweight body armor and protection of spacecraft from meteoroid impact. A kinetic energy projectile uses the energy of its motion to penetrate and possibly perforate a target.

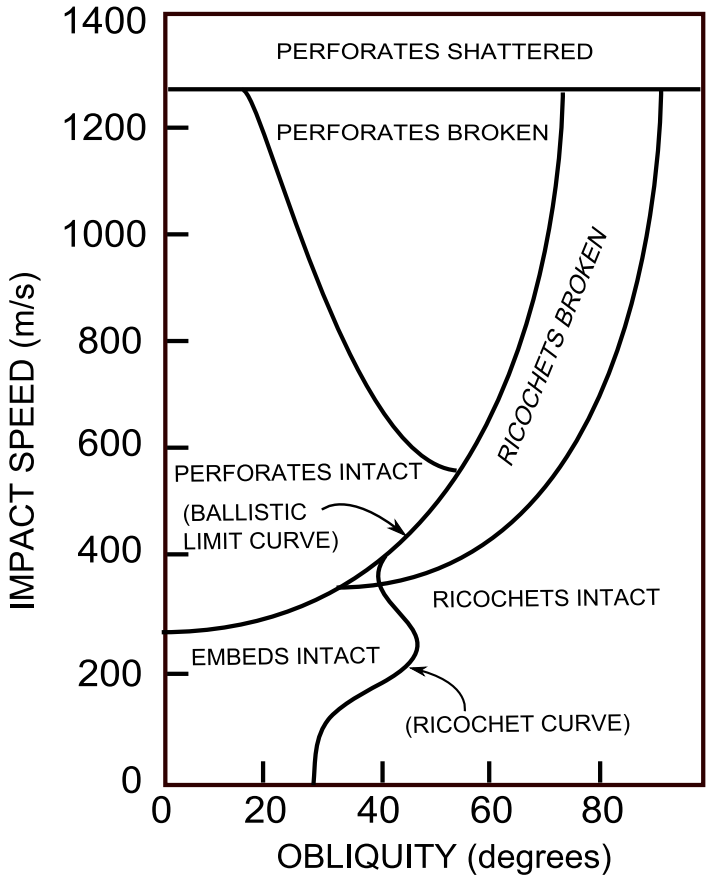

Figure 2.3: Phase Diagram for Projectile Impact [3, 52]

2.2.3 Ballistic Limit. In the study of impact events, one of the issues observed is the determination of the minimum velocity necessary to just perforate a target or some type of protective device. For any velocity less than this, the projectile will fail to perforate the target. Determining this value is of the utmost importance in the design and evaluation of protective structures, such as armor. This velocity is known as the critical impact velocity or the ballistic limit, v_{BL}.

The two classifications of methods that are used to determine v_{BL} are deterministic and probabilistic. The deterministic approach uses the conservation equations and the constitutive models to determine the ballistic limit velocity; however, simplifications that generally require empirical determination of at least one or two of the constants are typically introduced due to the complexities of the governing partial differential equations. In the probabilistic approach, an extensive database containing

the object's impact velocity and either its residual velocity or an account of whether or not it defeats the barrier. The striking velocity at which there is a 50 percent probability of perforation of the barrier is called v_{50}. [52].

2.2.3.1 Impact Below Ballistic Limit. If a cylindrical projectile impacts perpendicular to a target surface at a velocity below the ballistic limit the rod will most likely buckle. There is localized plastic deformation in the rod as the impact velocity is increased. Also the projectile tip mushrooms, with little or no indentation of the target. Even further increases in velocity will result in mushrooming and embedding of the rod, typically with little or no mass loss to the projectile [54]. Figure 2.4 summarizes these situations involving low velocity impact.

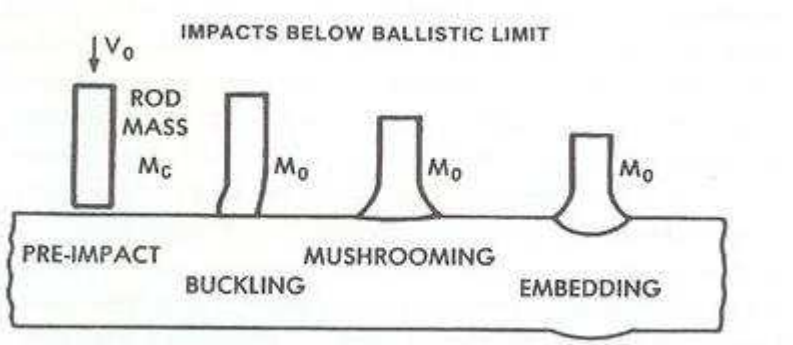

Figure 2.4: Low Velocity Impact Response [19, 54]

2.2.3.2 Impact Above Ballistic Limit. When a cylindrical rod impacts a target above the ballistic limit, an impact flash may be produced due to thermal heating at the moment of impact. High intensity stress waves are generated in the projectile and the target. Penetration of the projectile into the target begin almost instantaneously, as well as cratering of the target. The interface pressures surpass the material strength of the rod and plate resulting in hydrodynamic-like erosion of the projectile nose while the rest of it enters the cavity practically undeformed. Then

the crater grows deeper, and pressure is applied to the surrounding material of the target by the fluid-like expanding flow of the rod front causing the bottom of the crater to expand. In the plate material near the rod tip, tangential to the rod-plate deformation interfacial zone, strong shearing stresses are created. After an amount of time that varies depending on target thickness, material properties and striking velocity, the target will exhibit a bulging and dishing type of deformation of the free surface opposite of the initial impact due to the initial compression wave. When that compressive wave reflects at the free surface as a tensile wave, it can create spall at that boundary. The behavior of the projectile and target due to high velocity impact is depicted in Figure 2.5. Target failure eventually occurs by one or more of the mechanisms which will be covered in Section 2.2.4 [54].

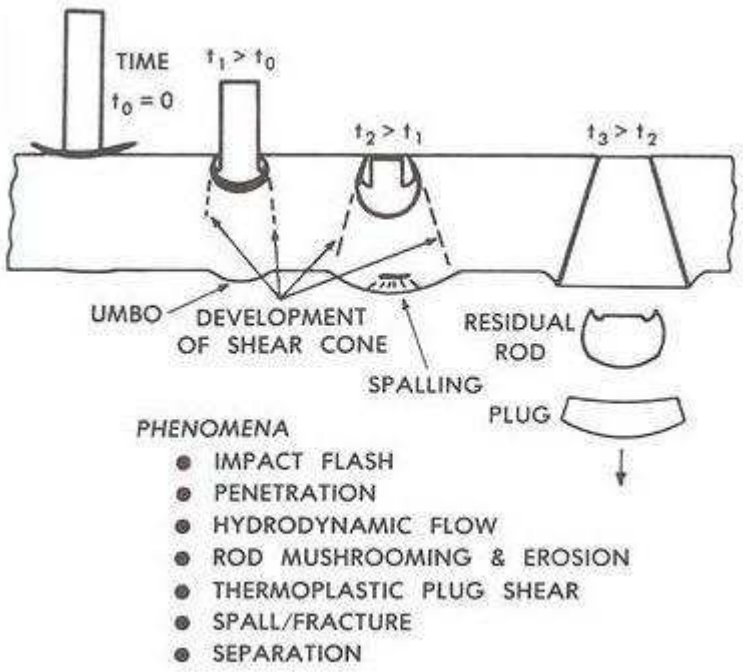

Figure 2.5: Impacts above the ballistic limit [19, 54]

For high velocity impacts into semi-infinite media, erosion completely consumes very short projectiles. Projectiles with length-to-diameter, L/D, ratios less than 2 are considered to be short projectiles. This phenomenon occurs very soon upon entry into

the target. As a result of kinetic energy exerted on the target, secondary penetration and radial hole growth occur. The cavity is generally almost hemispherical in shape. A cylindrical cavity is produced for intermediate rods, L/D $\simeq$ 4. A cavity that resembles a long-necked pitcher is typically observed for long rods, L/D $>$ 8, as seen in Figure 2.6. A cavity that is more cylindrical in shape results from long-rod penetration at ordinance velocities for the case where the rod strength exceeds the target strength [54].

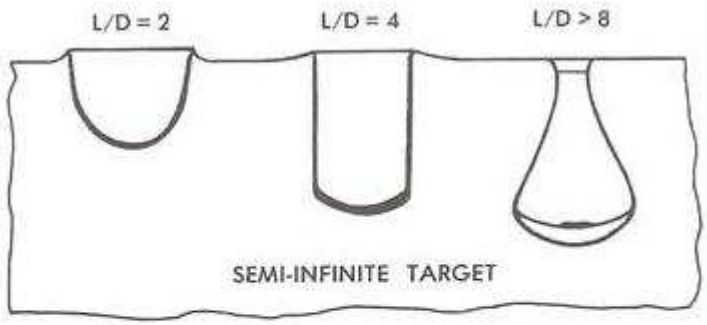

PHENOMENA (HIGH L/D PROJECTILES)

- ENTRANCE
- STEADY STATE PENETRATION
- CAVITY GROWTH
- RELAXATION

Figure 2.6: Hypervelocity impact into semi-infinite targets [19, 54]

2.2.4 Failure Modes. When discussing high velocity impact dynamics, it is important to consider the interaction of the projectile with the target. Targets are commonly classified by their thickness into the following three categories:

- *Semi-infinite* target is one in which the penetration event is not effected by the rear surface.
- *Thick* target exists when only after considerable penetration of the projectile into the target does the lower rear surface effect the penetration event.

- *Intermediate* target is where during almost all of the penetration event the rear surface applies substantial influence on the deformation process.
- *Thin* target is when stress and deformation gradients have negligible effects throughout the target thickness.

There are a variety of ways for impacted materials to fail. The actual failure mechanism is dependent on many parameters, such as striking velocity, material properties, projectile shape, method of target support and relative dimensions of the projectile and the target. Some of the more common failure modes for thin and intermediate thickness targets are shown in Figure 2.7. Any of the failure modes may dominate the failure of a target; however, many times more than one failure mode is present in an impact event. Spalling is when the target fails in tension due to the

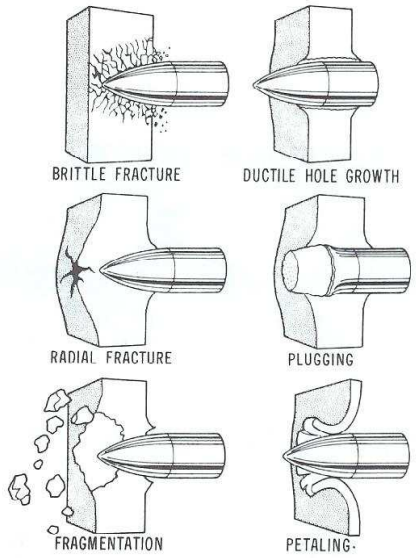

Figure 2.7: Failure Modes in Impacted Plates [Adapted from Backman (1976) and Backman and Goldsmith (1978)] [2, 3, 52]

initial compression wave reflecting off the rear surface of the target, which is common with explosive loading and extreme impact loading. Scabbing is very similar to spalling in appearance; however, in the case of scabbing the fracture is caused by large deformations. Due the initial stress wave surpassing the ultimate strength of the target, fracture can occur in weak, low-density targets, while radial fracture is more

common in materials where the tensile strength is much lower than the compressive strength like ceramics.

Plugging failure occurs when a finite-thickness target is impacted by either a blunt or hemispherical-nosed projectile at a velocity that is near the ballistic limit. The plug tends to be nearly cylindrical and close to the diameter of the projectile. The plug may separate from the target by void formation and growth in shear or by adiabatic shearing. Adiabatic shearing is when narrow bands of intense shear form; this generally is believed to initiate in areas of stress concentrations. If the impact velocity is greater than the ballistic limit by more than 5–10 percent, multiple fragments will be produced instead of a solid plug. Additionally, plugging failure tends to be rather sensitive to the impact angle and shape of the tip of the projectile.

Adiabatic shear failure becomes even more important for penetration of projectiles with sharp noses. For this configuration, the material in the target is typically displaced radially and no plug is developed. However, a change of failure mode occurs for materials that are more susceptible to adiabatic shear failure. For this case, a plug is pushed out along regions of extreme shear regardless of the geometry of the striker.

Intense radial and circumferential tensile stresses following the passage of the initial stress wave cause petaling of a target; these stress fields are produced near the nose of the projectile. Most often petaling is the result of ogival or conical projectiles impacting thin plates at relatively low-impact velocities or by blunt projectiles that are near the minimum velocity for perforation. Petaling results in large plastic flows and permanent bending. The target material strength is reached eventually, and cracks around the projectile tip form in the shape of a star. The forward advancement of the projectile causes the cracked sections to be pushed back forming a petal. Thick targets of low to medium hardness tend to fail through a combination of both ductile failure and spalling [52].

2.3 Wave Propagation in Rods and Plates

An explanation of some of the major features of wave propagation in solids is necessary in order to have a good understanding of impact problems and accurately interpret the results from CTH. Geometry, as well as mechanical properties, determine the way a wave propagates in a solid. Rods and plates are two common geometries that are used to investigate the effects of wave propagation. Waves in rods are considered to create a state of uniaxial stress (Figure 2.8). The stress along the rod axis is the crucial parameter. Elastic longitudinal, shear and torsional waves can all be

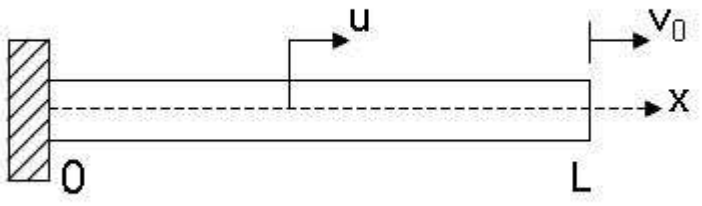

Figure 2.8: Rod Geometry for Wave Propagation [55]

supported by the rod. When the elastic limit is attained, then elastic and plastic waves will propagate; however, for this configuration, exceptionally high stress states are impossible to attain. As the strain rate gets larger, the deformation of the rod is dominated by two-dimensional and three-dimensional effects. The magnitude of the stress that can be carried in the rod is dictated by plasticity and material failure. Figure 2.9 shows idealizations of stress-strain curves that are used for analysis of materials in such configurations.

Higher levels of stress must be reached in order to study other states of materials; therefore, the plate configuration is used. Figure 2.10 shows a large plate being impacted by a thinner plate, often called a flyer plate. Upon impact, waves will propagate through the thickness of the flyer plate and the stationary plate. Waves

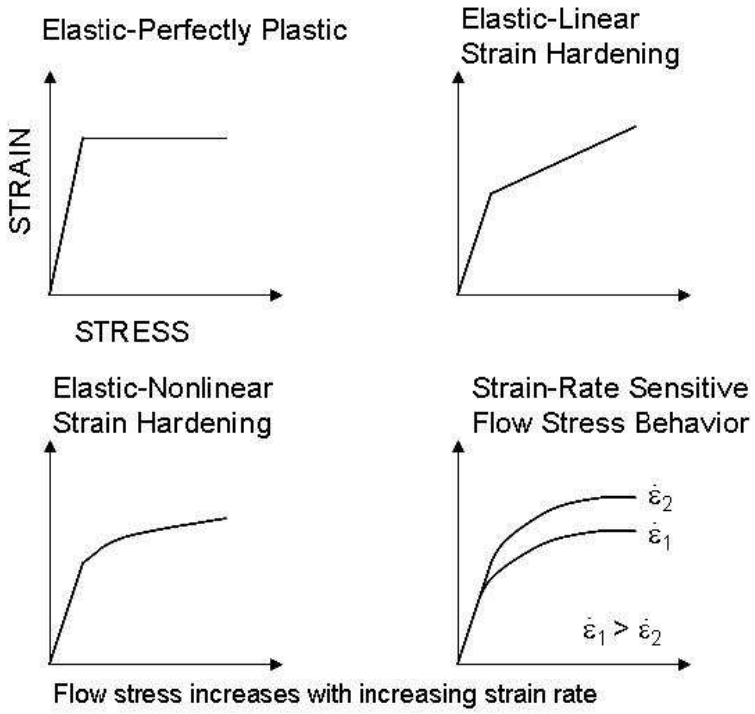

Figure 2.9: Idealized Stress-Strain Behavior for Rod Geometries [55]

will also be generated in the transverse direction. A state of uniaxial strain exists until these waves are reflected from the lateral boundary and travel back to the center.

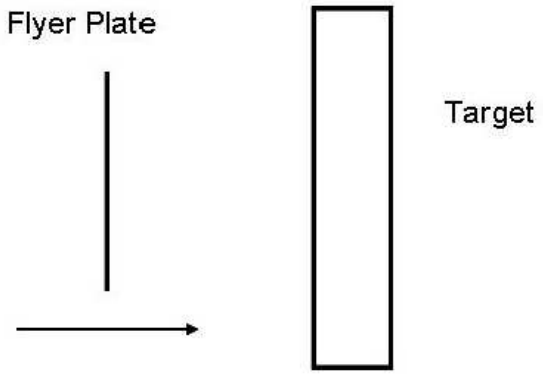

Figure 2.10: Plate Impact Geometry [55]

Consider a thin, cylindrical projectile, long enough so that wave reflections from its rear surface can be ignored, striking a semi-infinite body (Figure 2.11). Assume

that the target and the projectile are made of the same material. There various kinds

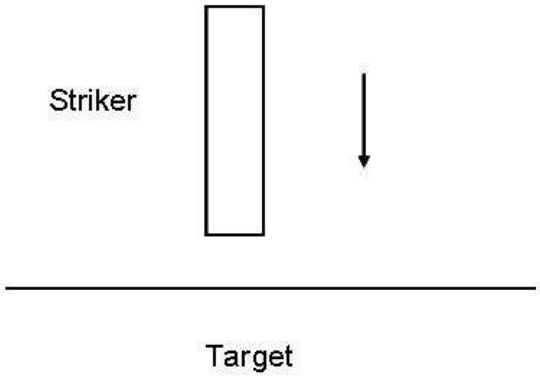

Figure 2.11: Striker Impacting Semi-infinite Surface [55]

of elastic waves that can be generated in solids, depending on how the particle movement in a solid relates to the direction the wave propagates and on the boundary conditions. The word "particle" here does not refer to the movement of atoms. The assumption of a continuum is the basis for elasticity theory. The effect of the individual movement of atoms is only observed in the aggregate, all particles in the material being made up of a sufficiently large amount of atoms such that it is perceived to be a continuum. As shown in Figure 2.12, commonly observed elastic waves are [24, 55]:

- Longitudinal waves: In theses waves the particle motion is back and forth in the direction of wave propagation in such a way that the particle velocity, u_p is parallel to the direction of the wave propagation. In some references, longitudinal waves are referred to as irrotational waves, push, primary, or P waves. They are also known as dilatational waves in infinite and semi-infinite media.
- Distortional waves: The particles move perpendicular to the direction of the wave propagation in this type of wave. The longitudinal strains $\epsilon_{11}, \epsilon_{22}, \epsilon_{33}$ are all zero, and no change in density results. Distortional waves are also called shear waves.
- Surface waves: These waves exist on the surface of a material and move both up and down and back and forth, similar to waves on the surface of water. The

particle movement describes an elliptical trajectory. They are called Raleigh waves in solids.

- Interfacial Waves: When two semi-infinite media with different properties are in contact, waves are formed at their interface. These waves can also be referred to as Stoneley waves.
- Waves in layered media: Special waves can emerge when a body is made up of a variety of materials, such as composites and functionally graded materials. These waves are also known as Love waves which were named after the first person to study them.
- Bending waves: Also called flexural waves, these waves involve propagation of flexure in a one or two-dimensional configuration throughout the body. These waves occur in structural members such as beams, plates and shells.

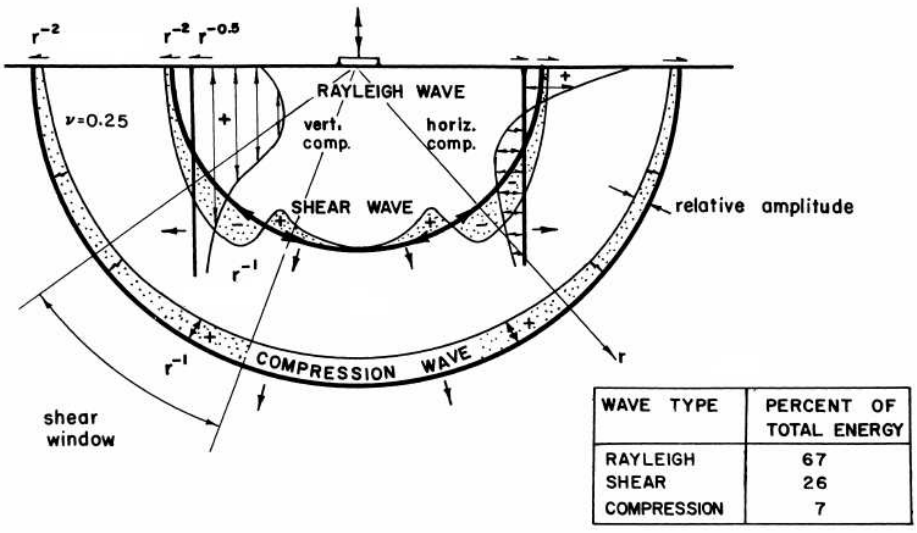

Figure 2.12: Distribution of displacement and energy in compressive, shear, and Rayleigh waves from a harmonic normal load on a semi-infinite half-space for $\nu = 0.25$ [50].

2.3.1 Elastic Waves. The general impact case can be simplified to a uniaxial rod impact case making it feasible to determine the magnitude of the elastic stress

wave applied to the rod. Figure 2.13 shows a moving rigid wall impacting a stationary bar with a constant velocity $v = v_0$ at time $t = 0$. This impact velocity, v_0 is much less than the material sound speed. An elastic wave develops in the rod after impact and propagates at the material sound speed to the right. The velocity of the particles behind the elastic stress wave has accelerated to the impact velocity, v_0 [28].

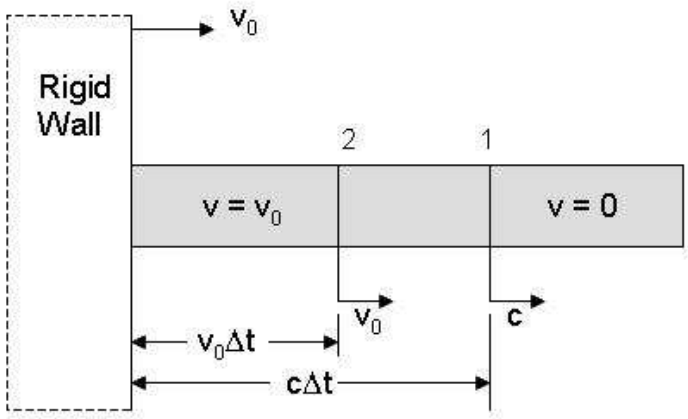

Figure 2.13: Uniaxial rod impact [28]

It can be shown that the material behind the elastic wave is in motion by equating impulse and momentum, which yields the momentum of that material to be

$$Momentum = \rho A c \Delta t v_0 \tag{2.1}$$

where ρ is the density, $c\Delta t$ is the length of the rod behind the wave front, which has a particle velocity of v_0, and A is the cross-sectional area of the rod. The impulse can be calculated by integrating the force over an interval of time. For this uniaxial example, the force is equal to the stress times the area that the stress is acting on. This results in an impulse of

$$Impulse = \int \sigma A dt \tag{2.2}$$

where σ is the compressive stress in the rod that exists because of the propagation of the stress wave. Assuming an infinitesimal time step, the elastic compressive stress wave is determined by applying the conservation of momentum to Equations (2.1) and 2.2) and dividing both sides by the area and the time step [28,35]. This gives the magnitude of the elastic compressive stress wave

$$\sigma = \rho c v_0. \tag{2.3}$$

The material sound speed can be solved for with the use of the wave equation and differential equations. Consider an element of the rod through which the passage of a disturbance is experienced as seen in Figure 2.14. The vertical sides of the element are at positions of x and $x + dx$, respectively. Assuming that tension is positive in the

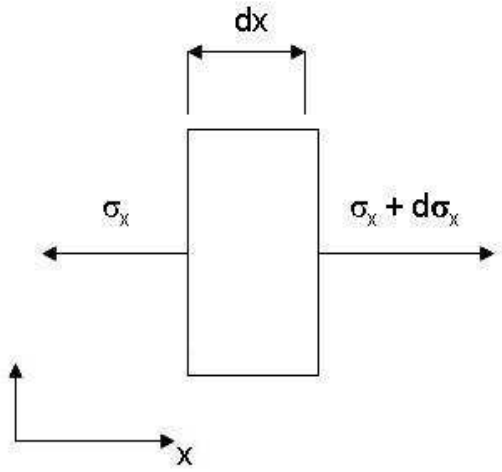

Figure 2.14: Rod element [28]

positive x direction, then the stresses on the left and right edges of the element are

$$-\sigma_x \qquad \text{and} \qquad \sigma_x + \frac{\partial \sigma_x}{\partial x} dx \tag{2.4}$$

respectively. The conservation of momentum for this element with area A is as follows

$$A(-\sigma_x)dxdt + A\left(\sigma_x + \frac{\partial \sigma_x}{\partial x}\right)dxdt = (\rho A)dxdv. \tag{2.5}$$

The impulse applied due to the stress on the vertical edges of the element is given by the left side of Equation (2.5); whereas, the momentum imparted over a time step is given by the right side of Equation (2.5). Dividing both sides by $Adxdt$ gives

$$\frac{\partial \sigma_x}{\partial x} = \rho \frac{\partial v}{\partial t} \tag{2.6}$$

The definitions for one-dimension strain and velocity are

$$\epsilon = \frac{\partial u}{\partial x} \qquad \text{and} \qquad v = \frac{\partial u}{\partial t} \tag{2.7}$$

respectively, where ϵ is the longitudinal strain in the x direction, u is the x displacement and v is the velocity. Using Equation (2.7) it can be shown that

$$\frac{\partial \epsilon}{\partial t} = \frac{\partial v}{\partial x}. \tag{2.8}$$

Assuming that stress is only a function of strain, then Equations (2.6) and (2.8) combined together result in the one-dimensional wave equation,

$$\frac{\partial^2 u}{\partial t^2} - c^2 \frac{\partial^2 u}{\partial x^2} = 0 \tag{2.9}$$

where

$$c^2(\epsilon) = \frac{\partial \sigma / \partial \epsilon}{\rho}. \tag{2.10}$$

For the case where the impact is elastic, the numerator is actually the modulus of elasticity for the material, which results in the following wave velocity

$$c = \sqrt{\frac{E_m}{\rho}} \tag{2.11}$$

where E_m is the modulus of elasticity for the material [5, 28].

It is also important to understand how waves propagate through a medium, as well as how the waves behave at the material boundaries. Nicholas [28] and Zukas [55] discuss wave propagation for a homogeneous metal rod impacting a semi-infinite rigid wall at a velocity of v_0 perpendicular to the wall similar to what is shown in Figure 2.15. It is assumed that there are no three-dimensional effects due to the impact being perpendicular and uniaxial. At the instant just prior to the rod striking the rigid wall, the internal stress throughout the rod is zero and the particle velocities in the rod are all v_0.

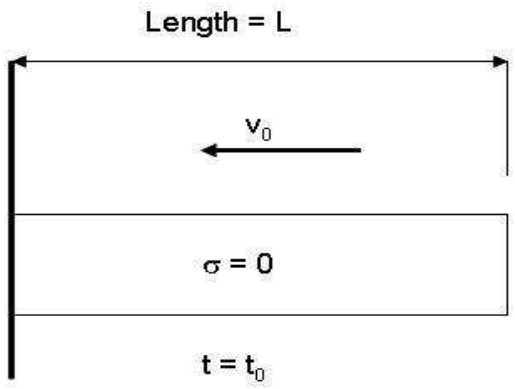

Figure 2.15: Rod impact prior to loading [28, 35]

Right at impact, a compressive stress wave is formed which propagates to the right at the material wave speed (Equation 2.11). Particles to the left of the wave have a constant compressive stress as given by Equation (2.3). In order to preserve continuity at the interface between the rod and the wall, the velocity on either side of the interface boundary must be the same; therefore, the end of the rod that strikes the

rigid wall has to immediately decelerate so that its velocity is zero just like the wall. Figure 2.16 shows this. The material wave velocity limits how quickly a wave can

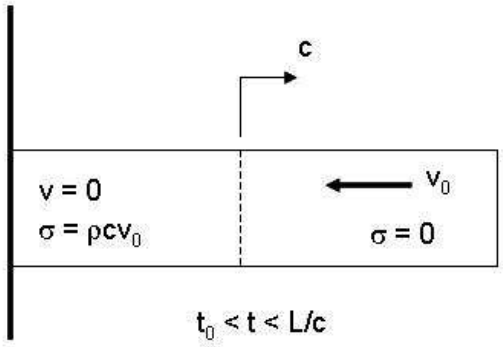

Figure 2.16: Rod impact prior to reflection [28, 35]

propagate through a material. This is why the right side of the rod keeps traveling to the left at the initial velocity, v_0 because it has yet to experience the impact.

At time t = L/c where L is the length of the rod, the wave has propagated through the entire rod and has reached the right end, as seen in Figure 2.17. The entire rod is under constant compressive stress expressed in Equation (2.3). At this brief moment in time, the rod has actually stopped. Due to the conservation of energy, the kinetic energy of the rod has been converted to internal strain energy.

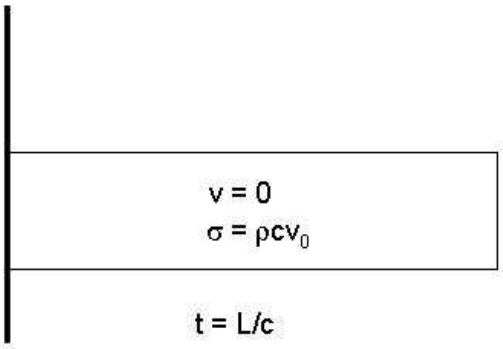

Figure 2.17: Rod impact at reflection [28, 35]

A free surface is unable to support an applied stress; therefore, the stress wave reflects when it reaches the free end of the rod. The reflected wave is now a tensile

wave propagating to the left, leaving the stress behind the wave equal to zero. Since there are no constraints on the right side, the stress wave that was initially traveling to the right continues to move in that direction, while the tension wave continues to the left. This can be seen in Figure 2.18. The tension wave effectively acts as an unloading wave that cancels the effects of the initial compressive wave.

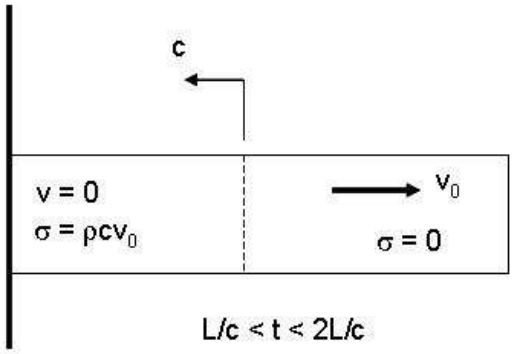

Figure 2.18: Rod impact after reflection [28, 35]

When the tension wave reaches the interface boundary between the rod and the wall, it tries to apply a tensile load to the wall. However, since the rod and wall are not physically joined, the interface cannot support the tensile stress, and the rod rebounds off the wall at the initial striking velocity v_0, see Figure 2.19 [28, 35].

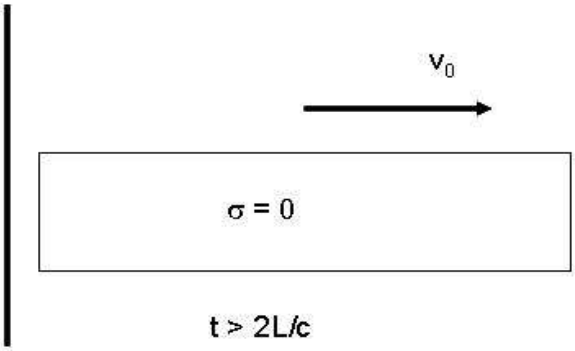

Figure 2.19: Rod impact after unloading [28, 35]

2.3.2 Plastic Waves. The stress-strain curve for most metals is characterized by a linear elastic region at low strains followed by another portion that may or may not be linear as well. The point where the material no longer behaves strictly elastically is called the yield stress or Hugoniot elastic limit (HEL). When a stress exceeding the HEL is reached, the material will plastically deform. In an impact event, an elastic stress wave is initially produced. When the particle stress applied surpasses the yield stress of the material, a plastic stress wave, which is slower than the elastic wave is generated. The propagation of a plastic stress wave can be explained by two different theories that have been developed. These two theories put a different amount of emphasis on the significance of the strain-rate in determining the response of the material. The two theories that depict material behavior as it is plastically deformed are the rate-independent theory and the rate-dependent theory. The rate-independent theory assumes that no matter what strain-rate is applied the material behavior can accurately be depicted using a single dynamic stress-strain curve. This theory was developed from the assumption that a material has a bilinear stress-strain curve similar to the one in Figure 2.20 [26].

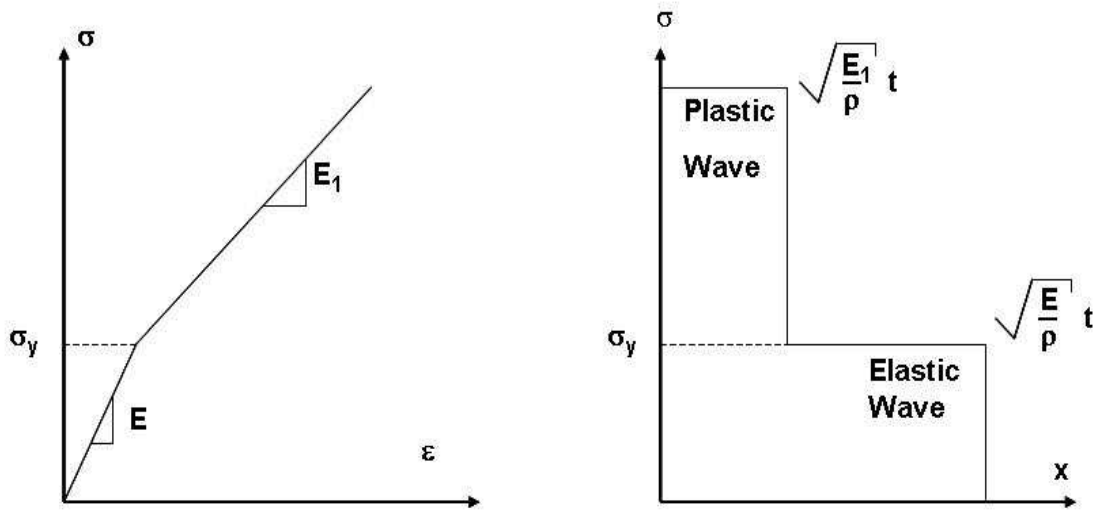

Figure 2.20: Stress-strain relation and wave profile for bilinear material [26]

The rate-independent theory predicts that two distinct waves will be formed in the material. These waves would propagate through the material at velocities based on their respective elastic moduli, as well as plastic regions E and E_1. These plastic regions in turn result in a wave profile like the one seen in Figure 2.20. The elastic stress wave would travel at the speed shown before in Equation (2.11) and a magnitude given by Equation (2.3). The plastic stress wave on the other hand would have a speed of

$$c_p = \sqrt{\frac{E_p}{\rho}} \tag{2.12}$$

where c_p is the plastic wave speed and E_p is the slope of the stress-strain curve in the plastic region. The plastic stress wave will have a magnitude of

$$\sigma_p = \rho c_p v_0 \tag{2.13}$$

where σ_p is the magnitude of the plastic stress wave. In Figure 2.20 an example of a wave profile with both elastic and plastic wave fronts is shown [26].

A different method of analysis for the rate-independent theory makes the assumption that past the yield stress the stress-strain curve is concave upward instead of bilinear, as seen in Figure 2.21. For stress-strain curves where the slope of the plastic region is not linear, a more general form of the plastic wave velocity must be used (Equation 2.14). E_p is replaced by $d\sigma/d\epsilon$ which is the slope of the stress-strain at any particular strain.

$$c_p = \sqrt{\frac{d\sigma/d\epsilon}{\rho}} \tag{2.14}$$

As the strain gets larger than the strain value that corresponds to the yield stress (point A of Figure 2.21), the slope of the curve increases, and therefore, stress wave velocity increases as well. This in turn means that low stress waves will eventually be

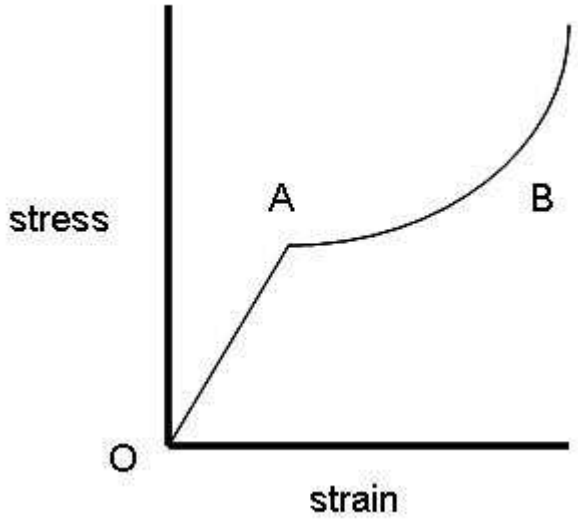

Figure 2.21: Concave-up stress-strain curve [35]

overtaken by the high stress waves. When that occurs, a plastic shock front will be formed; this is depicted in Figure 2.22 [26].

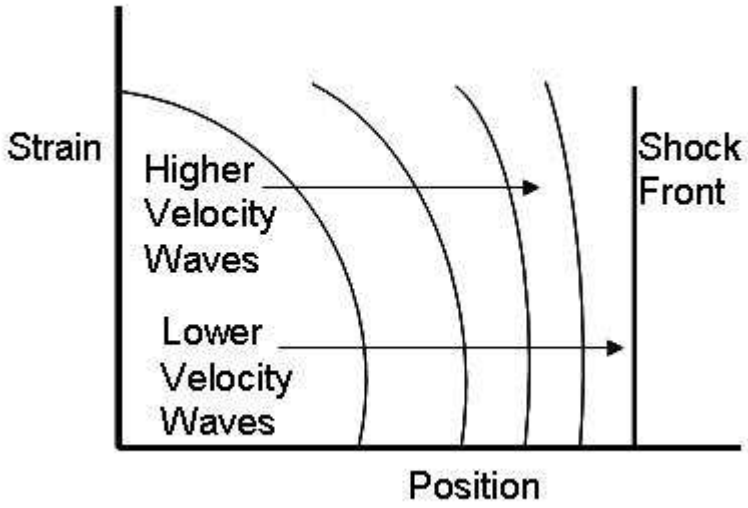

Figure 2.22: Formation of plastic shock front [35]

Certain aspects of wave propagation were not able to be accounted for using the rate-independent theory so the rate-dependent theory was developed to explain

those phenomena. This theory matches more closely with the true plastic stress-strain curves attained from experimentation. The most commonly used rate-dependent expression was proposed by Malvern to describe the dynamic behavior of materials of the form

$$\sigma = f(\epsilon) + aln(1 + b\dot{\epsilon}_p) \tag{2.15}$$

where $f(\epsilon)$ is the stress from a quasi-static stress-strain curve, $\dot{\epsilon}_p$ is the plastic strain-rate and the rate sensitivity is described by the constants a and b. Equation (2.15) can also be written as a function of the overstress, $\sigma - f(\epsilon)$, see Equation (2.16). The overstress is the instantaneous stress minus the value that would occur in a quasi-static test at the same strain value.

$$\dot{\epsilon}_p = \frac{1}{b}\left[exp\left(\frac{\sigma - f(\epsilon)}{a}\right) - 1\right] \tag{2.16}$$

The following equation shows the overstress function in a more general form where an arbitrary function F is present.

$$E\dot{\epsilon}_p = F[\sigma - f(\epsilon)] \tag{2.17}$$

The overstress function developed by Malvern breaks the strain-rate into elastic and plastic components. It also makes the assumption that the elastic strain rate and the stress rate are related by Hooke's Law. Beyond that it allows for a general form of the plastic strain rate function in the following forms

$$E\dot{\epsilon}_p = g(\sigma, \epsilon) \tag{2.18}$$

or

$$E\dot{\epsilon} = \dot{\sigma} + g(\sigma, \epsilon) \tag{2.19}$$

The linear form of the overstress function shown below has been commonly used in simulations concerned with propagation of a plastic wave due to its computational simplicity.

$$g(\sigma, \epsilon) = k[\sigma - f(\epsilon)] \tag{2.20}$$

2.3.2.1 Shock Waves. When the striking velocity is much faster than material sound speed, an elastic stress wave will form followed by a plastic stress wave. This leads to the development of a shock wave. Shock waves are very narrow regions in a continuum in which the velocity, temperature and density vary discontinuously. The differential form of the conservation equations are only valid when state properties are continuous, which as just mentioned is not the case for shock waves. The conservation equations which will be discussed later in Subsection 3.1 can be applied to develop the equations for a shock wave. Consider a semi-infinite material that is stationary, stress free and has no internal energy with a shockwave propagating from the left to the right, similar to Figure 2.23. The physical state ahead of and behind the shock

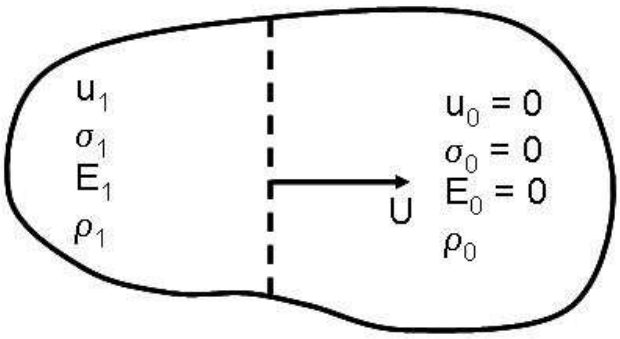

Figure 2.23: Conditions at moving shock front [28]

are identified by subscripts 0 and 1, respectively. The velocity of the shock wave is U, and the particle velocity is u. The mass flow rate into the shock must be equal to the mass flow rate exiting the shock according to the conservation of mass. The particles in front of the shock are assumed to have a velocity, u_0 equal to zero. Mathematically

the conservation of mass can be stated as

$$\rho_0 dA(u_0 - U)\Delta t = \rho_1 dA(U - u_1)\Delta t \tag{2.21}$$

where mass entering the shock from the right is $\rho_0 dA(u_0 - U)\Delta t$, while the mass entering the shock left is $\rho_1 dA(U - u_1)\Delta t$. Keeping mind that the velocity in front of the shock is assumed to be zero, the following equation can be obtained when both sides of Equation (2.21) are divided by the time Δt and the differential area dA.

$$\rho_0 U = \rho_1(U - u_1) \tag{2.22}$$

Next, the conservation of momentum must be applied. The difference between the impulse applied and the momentum change across the shock must be zero, or

$$\sigma_1 dA\Delta t - \rho_0 dAU\Delta t u_1 = 0. \tag{2.23}$$

By once again dividing by the time Δt and the differential area dA, Equation 2.23 can be simplified to yield the definition of stress in regards to shock waves,

$$\sigma_1 = \rho_0 U u_1. \tag{2.24}$$

Finally, the conservation of energy, which states the initial energy plus the work done to go from state 0 to state 1 is equal to the final energy, must be examined for shock waves,

$$TE_0 + W_{0\to 1} = TE_1 \tag{2.25}$$

where TE_0 is the initial total energy, $W_{0\to 1}$ is the work done to go from state 0 to state 1 and TE_1 is the final total energy. The internal energy per unit mass, E, plus the kinetic energy per unit mass, KE, make up the total energy, TE. These terms can

be used to define the total energy at states one and two as follows,

$$TE_0 = E_0 + KE_0 \qquad \text{and} \qquad TE_1 = E_1 + KE_1. \tag{2.26}$$

There are a variety of things that can make up the internal energy per unit mass, such as the release of energy due to a chemical reaction or a material with stored strain energy. Since the initial velocity, u_0 is zero, the kinetic energy at state 0, KE_0 is also zero. However, the kinetic energy at state 1 is

$$KE_1 = \frac{1}{2}(\rho_0 U \Delta t)(u_1)^2 \tag{2.27}$$

where $\rho_0 \Delta t$ is the mass of the material that is moving and u_1 is the velocity at which the mass is moving. Following the passage of the shock wave, the internal energy is

$$(\rho_1(U - u_1)\Delta t)\, E_1 \tag{2.28}$$

where the velocity relative to the shock is used to obtain the mass. Combining Equations (2.26), (2.27) and (2.28) results in the following expression for the total energy after the passage of the shock,

$$TE_1 = (\rho_1(U - u_1)\Delta t)\, E_1 + \frac{1}{2}(\rho_0 U \Delta t)(u_1)^2. \tag{2.29}$$

Since the velocity and kinetic energy in front of the shock are zero; the total energy is

$$TE_0 = (\rho_0 U \Delta t) E_0 \tag{2.30}$$

Work is the force applied times the distance over which it is applied so the work done on the system going from states 0 to 1 is

$$W_{0\to 1} = \sigma_1(u_1 \Delta t). \tag{2.31}$$

The area is excluded from the work equation because all the properties are assumed to be applicable over a common area. The combination of Equations (2.28), (2.30) and (2.31) yields the equation for the conservation of energy for a moving shock wave

$$(\rho_0 U \Delta t) E_0 + \sigma_1 (u_1 \Delta t) = (\rho_1 (U - u_1) \Delta t)\, E_1 + \frac{1}{2} (\rho_0 U \Delta t)(u_1)^2. \tag{2.32}$$

Dividing by time Δt and organizing the equation such that internal energy per unit mass terms are on the same side gives

$$\rho_1 (U - u_1) E_1 - (\rho_0 U) E_0 = \sigma_1 u_1 - \frac{1}{2} (\rho_0 U)(u_1)^2. \tag{2.33}$$

The equations for the conservation of mass (Equation 2.22) and the conservation of momentum (Equation 2.24) can be applied to the second term on the left side of the equation and the second term on the right side of the equation, respectively, resulting in

$$\rho_1 (U - u_1) E_1 - \rho_1 (U - u_1) E_0 = \sigma_1 u_1 - \frac{1}{2} \sigma_1 u_1. \tag{2.34}$$

Dividing through on both sides by $\rho_1 (U - u_1)$ yields

$$E_1 - E_0 = \frac{\frac{1}{2} \sigma_1 u_1}{\rho_1 (U - u_1)}. \tag{2.35}$$

Solving for u_1 in the equation for the conservation of momentum and substituting into the above equation gives

$$E_1 - E_0 = \frac{\frac{1}{2} \sigma_1 \left(\frac{U(\rho_1 - \rho_0)}{\rho_1} \right)}{\rho_1 \left(U - \frac{U(\rho_1 - \rho_0)}{\rho_1} \right)}. \tag{2.36}$$

Dividing through by U and finding a common denominator will result in the following equation

$$E_1 - E_0 = \frac{\frac{1}{2}\sigma_1(\rho_1 - \rho_0)}{\rho_1\rho_0}. \tag{2.37}$$

The more commonly used equation for conservation of energy regarding shock waves can be attained with the following simplification,

$$E_1 - E_0 = \frac{1}{2}\sigma_1\left(\frac{1}{\rho_0} - \frac{1}{\rho_1}\right). \tag{2.38}$$

The three conservation equations are referred to as the Hugoniot equations [28].

The conservation equations by themselves contain five unknowns, U, u, σ, E and ρ; having only three equations and five unknowns is clearly a problem. The use of a Hugoniot curve or an equation-of-state is used to remedy this problem. A Hugoniot curve is a locus of all the attainable shock states that are possible in a material; it relates pressure to volume for a hydrostatic loading condition. The relationship between the hydrostatic pressure and specific volume are described by performing a large number of planar impact experiments. Each point on the Hugoniot curve represents an equilibrium state for a specific experiment. Figure 2.24 shows a generic Hugoniot curve where it is designated by an H. The loading path follows what is called the Rayleigh line (designated in Figure 2.24) from point A where the material initially has a zero pressure but a high velocity to point B when an impact occurs with an initial velocity v_0. It appears that the loading follows a straight line that connects the initial state with the point along the Hugoniot curve relating to the peak pressure of impact (marked as P_H in the figure) instead of the Hugoniot curve. Unloading does not seem to occur along the Hugoniot curve, instead it occurs isentropically along the line marked S. Hugoniot curves are only valid in certain restricted situations, since they are developed under uniaxial strain shock wave conditions, which leads to the use of equations-of-state, which are more general. In most computer codes that solve impact problems, an EOS is used to relate internal energy, pressure and volume.

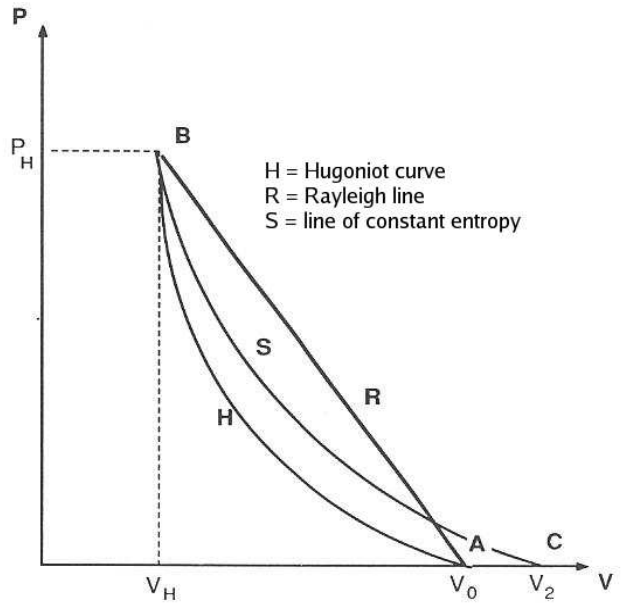

Figure 2.24: Hugoniot curve [35]

An EOS can be developed from experimental and theoretical sources. A couple of experiments that can be used to develop an EOS include planar impact and diamond anvil experiments.

2.4 Stress Wave Propagation in Layered Materials

Layered materials exist in nature, and they can be manufactured through a process that bonds layers of various materials in order to create a composite material with the desirable mechanical, thermal or electrical properties. Because of the interface between each layer, waves traveling through a layered material behave considerably different from waves in a homogeneous material [4]. The density and relative strength at the interface boundary of two different materials affects stress wave propagation. In general, when an incident wave reaches an interface between two different materials, the wave is reflected and transmitted. At the interface, there are two conditions that must hold assuming that the layers remain in constant contact. The first is that the forces in both layers must be equal at the interface. The second condition is that the particle velocities at the interface must be continuous [48, 55]. The first condition

gives the following expression

$$A_1(\sigma_I + \sigma_R) = A_2\sigma_T \tag{2.39}$$

where A_n is the area in which n designates the layer, σ_I designates the incident stresses, σ_R designates the stress of the reflected wave and σ_T designates the stress of the transmitted wave. The 1 denotes the material the incident and reflected waves are in, and the 2 denotes the material the transmitted wave is in. The second condition gives

$$v_I - v_R = v_T, \tag{2.40}$$

or, using the velocity $v = \sigma/\rho c$ where ρ is the density and c once again is the sound speed of the layer. Multiplying density and sound speed (ρc) together introduces a new parameter known as the acoustic impedance. This relation yields

$$\frac{\sigma_I}{\rho_1 c_1} - \frac{\sigma_R}{\rho_1 c_1} = \frac{\sigma_T}{\rho_2 c_2} \tag{2.41}$$

Solving Equations (2.39) and (2.41) simultaneously for the reflected and transmitted stresses as a function of the incident stress results in

$$\sigma_R = \frac{A_2\rho_2 c_2 - A_1\rho_1 c_1}{A_1\rho_1 c_1 + A_2\rho_2 c_2}\sigma_I, \tag{2.42}$$

$$\sigma_T = \frac{2A_1\rho_2 c_2}{A_1\rho_1 c_1 + A_2\rho_2 c_2}\sigma_I. \tag{2.43}$$

Figure 2.25 shows a plane wave impacting a structure that has three layers each with a different acoustic impedance. The three layers have acoustic impedances such that $\rho_1 c_1 = 2\rho_2 c_2 = 4\rho_3 c_3$ starting from the layer on the left and moving right [55]. With an intensity of σ_I, the wave is transmitted through the first layer. When the

wave reaches the interface between materials one and two, part of it is transmitted into the second layer, and part of it is reflected. Figure 2.25 shows this as point (1). The equations below can be used to calculate the stress of the transmitted and reflected waves at the corresponding points,

$$(1)\sigma_{R1} = -1/3\sigma_I \qquad (4)\sigma_{I4} = \sigma_{R3}$$
$$\sigma_{T1} = 2/3\sigma_I \qquad \sigma_{R4} = 2/81\sigma_I$$
$$\sigma_{T4} = -4/81\sigma_I$$

$$(2)\sigma_{I2} = \sigma_{T1} \qquad (5)\sigma_{I5} = \sigma_{R4}$$
$$\sigma_{R2} = -2/9\sigma_I \qquad \sigma_{R5} = 2/243\sigma_I$$
$$\sigma_{T2} = 4/9\sigma_I \qquad \sigma_{T5} = 8/243\sigma_I$$

$$(3)\sigma_{I3} = \sigma_{R2} \qquad (6)\sigma_{I6} = \sigma_{R5}$$
$$\sigma_{R3} = -2/27\sigma_I \qquad \sigma_{R6} = 2/729\sigma_I$$
$$\sigma_{T3} = -8/27\sigma_I \qquad \sigma_{T6} = 4/729\sigma_I$$

These equations are treating the layers as if all cross-sectional areas are equal and therefore drop out of the equations. When the transmitted wave reaches the interface between layers two and three, there is transmission and reflection of the wave. Due to the values of the acoustic impedance, the reflected wave at point two will be a tensile wave. When this tensile wave reaches the interface between material two and one [point (3)], transmission and reflection occurs. Once again due to the values used for acoustic impedance in this example, the transmitted wave becomes a compression wave, and the reflected wave remains a tension wave. The process is repeated at point (4) and the following points until the waves dampen out [55].

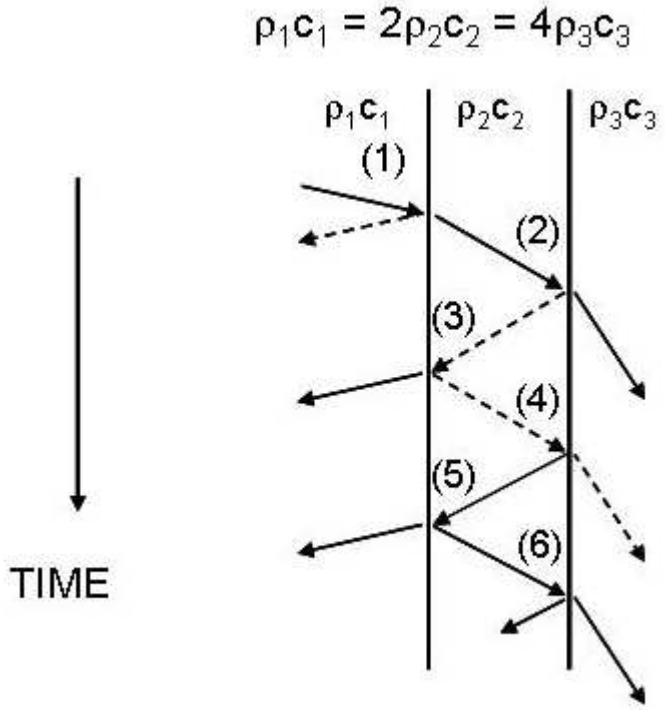

Figure 2.25: Stress wave transmission across laminated plates [55]

III. Fundamental Equations

Finding the solution to a numerical model of a high velocity impact event requires the use of several types of equations. CTH uses the conservation equations in conjunction with the equations-of-state and constitutive equations to model impact dynamics. A basic understanding of these equations and how they are applied in CTH are discussed here.

3.1 Conservation Equations

There are three fundamental principles that are the basis for almost all of the work in the areas of mechanics and dynamics [28]. These three principles are the conservation of mass, the conservation of momentum, and the conservation of energy, and they are presented below.

The Conservation of Mass states that mass can neither be created nor destroyed. Mathematically, it can be stated in the following way

$$\int_V \rho \, dV = const \tag{3.1}$$

where ρ is the density, and V is the volume of the material. The second law of conservation states that the net force equals the rate of change of momentum. The Conservation of Momentum can be written in a variety of forms. Taking mass to be constant, it can be expressed by Newton's second law:

$$F = m \frac{dv}{dt} \tag{3.2}$$

where F is the applied force, m is the mass acted upon, v is the velocity of the mass, and t is the time over which the event takes place. Conservation of Momentum for a closed system of n masses, m_i, not acted on by any external forces states

$$\sum_{i=1}^{n} m_i v_i = const \tag{3.3}$$

One other useful form is known as the impulse-momentum law. This form can be obtained by multiplying dt to both sides of Equation 3.2 and integrating, giving

$$Impulse = \int F\,dt = \int m\,dv = mv_f - mv_i \tag{3.4}$$

where the impulse is applied by the force over some time interval and v_i and v_f are the initial and final velocities of the mass, respectively. This says that the momentum of an object is changed from an initial value mv_i to a final value mv_f when an impulse is imparted. The Conservation of Energy states that the total amount of energy is conserved, although it may change forms. It can be written for a set of j discrete masses in the following form

$$\sum_j E_i + \sum_j \frac{1}{2}\rho v_i^2 = \sum_j E_f + \sum_j \frac{1}{2}\rho v_f^2 + W \tag{3.5}$$

where E is the internal energy, the $\frac{1}{2}\rho v^2$ terms are the kinetic energy, and W is the work done on the system [28].

3.2 Equation of State

An equation of state, (EOS), relates the thermodynamic properties (pressure and internal energy) of a material to its density and temperature. Pressures that are considerably higher than the material strength are dealt with through an EOS. Compressibility effects (changes in density) and irreversible thermodynamic processes such as shock heating are taken care of by the EOS [1]. When modeling impact problems, it is normal to break down stress into two components, hydrostatic stress and deviatoric stress,

$$[\sigma] = [\sigma_h] + [\sigma_d] \tag{3.6}$$

where $[\sigma]$ is the stress tensor, $[\sigma_h]$ is the hydrostatic stress tensor, and $[\sigma_d]$ is the deviatoric stress tensor. For a given parallelepiped of material, the hydrostatic stress

causes a change in volume, and therefore, it is also known as the volumetric stress. The deviatoric stress on the other hand produces a change in shape. Two separate relationships are used to handle these two types of stress in impact problems. The relationship that deals with the hydrostatic stress is known as the equation of state. The other relationship deals with the deviatoric stress and is taken care of by the constitutive equations which are discussed in the next section. Since hydrostatic pressure has very little dependence on strength and plasticity and deviatoric stress is only slightly dependent on pressure, these two relationships are treated separately from one another [27]. The general form of the EOS can be written as

$$E = E(P, V_{sp}) \tag{3.7}$$

where E is the internal energy, P is the pressure, and V_{sp} is the specific volume. Hydrocodes commonly use an alternative form of Equation (3.7) stated in the following way

$$P = P(\rho, E) \tag{3.8}$$

where ρ is the density ($\rho = 1/V$).

Two completely separate EOS packages are available in CTH; they are the Model Interface Guidelines EOS (MIGEOS) and the Analytic EOS (ANEOS). The more up to date package is the MIGEOS package which is recommended for most problems. There are many different MIGEOS models available in CTH. Some of the most common MIGEOS models used are the Sesame tabular EOS, Mie-Grüneisen analytic EOS, Jones-Wilkins-Lee analytic EOS, Phase Transition EOS (PTRAN) and the Ideal Gas EOS.

The Mie-Grüneisen EOS assumes that the Grüneisen parameter Γ is a only a function of density. In CTH, the Mie-Grüneisen model uses the following formulas

$$P(\rho, E) = P_H(\rho) + \Gamma_0 \rho_0 [E - E_H(\rho)] \tag{3.9}$$

$$R(\rho, T) = E_H(\rho) + C_v [T - T_H(\rho)] \tag{3.10}$$

where P_H, E_H and T_H are the Hugoniot pressure, energy and temperature. The Grüneisen parameter Γ_0 and specific heat C_v are taken to be constants. The following two equations are used to determine the Hugoniot pressure and energy

$$P_H = P_0 + \rho_0 U_s u_p = P_0 + \rho_0 U_s^2 \mu \tag{3.11}$$

$$E_H = E_0 + (1/2) u_p^2 = E_0 + (P_H + P_0)\mu / 2\rho_0 \tag{3.12}$$

where ρ_0, P_0 and E_0 are the initial density, pressure and Energy. U_s is the shock wave velocity, u_p is the particle velocity and $\mu = 1 - \rho_0/\rho$.

There are two options in CTH for describing the Hugoniot. The first option is a quadratic equation that relates the shock velocity, U_s, to the particle velocity, u_p,

$$U_s = C_s + S_1 u_p + (S_2/C_s) u_p^2 \tag{3.13}$$

where $C - s$, S_1 and S_2 are constants. Modifying Equation (3.13) to treat nonlinear behavior at low pressures gives the second option for the Hugoniot in CTH. This modified option, which is shown below, expresses the velocity of the shock wave as a function of strain, μ. As a reminder, $\mu = 1 - \rho_0/\rho$.

$$U_s = 2C_s[(1 - S_1\mu + \sqrt{(1 - S_1\mu)^2 - 4S_2\mu^2})]^{-1} - Bexp[-(\mu/\mu^*)^N] \tag{3.14}$$

Equation (3.14) reduces down to Equation (3.13) when B = 0. As μ goes to zero in Equation (3.14), U_s goes to C_s - B; however, as μ gets larger, U_s approaches Equation

(3.13). For a more in depth look at the Mie-Grüneisen EOS in CTH refer to the CTH EOS reference manual [16].

The PTRAN EOS model in CTH is used to model material that transitions from one phase to another phase. In order to simulate these phase transitions, individual models that are applicable at certain phases for a material are combined together. One limitation of the PTRAN model is that it only accounts for two phases. The PTRAN model in CTH denotes the pressure in the transition region by the following equation

$$P(\rho, T, \lambda) = P_T + \beta_T(1 - \rho_T/\rho) + A_T(T - T_{room}) + A_\lambda \lambda. \tag{3.15}$$

P_T and ρ_T are the transition pressure and density of phase one at room temperature, T_{room}. β_T is the bulk modulus in the transition region and A_T and A_λ are derivatives of the transition pressure with respect to T and λ. P_T, β_T, A_T and A_λ are all input parameters. The mass fraction of phase two, λ is selected such that Equation (3.16) for the mixture pressure is satisfied.

$$P(V, T) = -(\partial A/\partial V)_{T,\lambda,\xi,\eta} = \phi_1 P_1(V_1, T_1) + \phi_2 P_2(V_2, T_2) \tag{3.16}$$

where the ϕ_i's are volume fractions,

$$\phi_1 = (1 - \lambda)V_1/V = (1 - \lambda)\xi_1,\ \phi_2 = \lambda V_2/V = \lambda \xi_2,\ \phi_1 + \phi_2 = 1 \tag{3.17}$$

Further explanation of this model can be found in the CTH manual titled Recent Improvements to the CTH EOS Package [17].

This research uses the Sesame EOS which is a tabular EOS that requires interpolation between values in the table [55]. This tabular EOS correlates pressure, density, and energy at various states. There are few major advantages to using a tabular EOS. First, since the EOS variables are already part of the table, there is no need to calculate them. A tabular EOS also allows the exact physical state to be used,

instead of an assumed state, as in the Mie-Grüneisen EOS which uses a quadratic form. Valid results can be found over a much wider density-temperature range when using a tabular EOS as compared with an analytical EOS. If the applied pressures are large enough that a material change of state (i.e. from solid to liquid or liquid to gas) occurs, the tabular EOS advantages can make a significant difference [35].

3.3 Constitutive Equation

A constitutive model is used to characterize the unique behavior of a particular material. The constitutive equations relate the material stress, strain, and deformation gradient to each other [10]. This relation allows us to determine the stress in terms of strain, strain-rate effects (both in loading and unloading), and internal energy (thermal softening) [1]. Thermal variables such as heat and temperature can also be taken in to consideration in constitutive models [10].

Some of the more common constitutive models found in CTH are as follows:

- Johnson-Cook viscoplastic model
- Zerilli-Armstrong viscoplastic model
- Johnson-Holmquist ceramic models I & II
- Steinberg-Guinan-Lund viscoplastic model
- Bammann-Chiesa-Johnson viscoplastic model

The Johnson-Cook and Zerilli-Armstrong constitutive models are used for predicting the deviatoric stresses for ductile materials and include the effects of strain-hardening, temperature and strain-rate on the yield stress [43]. Johnson and Holmquist have developed two constitutive models to compute the yield stress of hard, brittle materials like ceramics under dynamic loading conditions. The Johnson-Cook viscoplastic model and the Johnson-Holmquist II ceramic model will be considered in more depth in the following subsections.

3.3.1 Johnson-Cook Constitutive Model. Many times, high velocity impact events are accompanied by increases in temperature due to adiabatic heating. The constitutive relation needs to take into account the temperature effects on the flow stress in order to precisely determine the response of the material. The Johnson-Cook model attempts to account for strain, strain-rate and temperature effects. This is an empirical model that contains the constants A_{jc}, B_{jc}, C_{jc}, N_{jc}, and M_{jc}. The Johnson-Cook constitutive equation is written as

$$\sigma = [A_{jc} + B_{jc}(\epsilon_p)^{N_{jc}}][1 + C_{jc} ln(\dot{\epsilon}_p^*)][1 - (T^*)^{M_{jc}}], \tag{3.18}$$

where σ represents the stress, ϵ_p represents the equivalent plastic strain, $\dot{\epsilon}_p^* = \dot{\epsilon}_p/\dot{\epsilon}_0$ represents the dimensionless plastic strain-rate for $\dot{\epsilon}_0 = 1.0s^{-1}$, and T^* represents the homologous temperature,

$$T^* = \frac{(T_{abs} - T_{room})}{(T_{melt} - T_{room})}, \tag{3.19}$$

where T_{abs} is the absolute temperature, T_{room} is room temperature and T_{melt} is the melting temperature. Johnson and Cook took experimental data and basically developed an equation that attempts to fit the data curves. Equation (3.18) is not based on theory; the five constants are determined from the experimental results [27, 55].

3.3.2 Johnson-Holmquist Two Model for Ceramics. Both the Johnson-Holmquist I (JH-1) and Johnson Holmquist II (JH-2) ceramic models are included in CTH version six. The ceramic material that was used in this research was implemented in the Viscoplasticity Data File in version six for the JH-2 model and not the JH-1 model. Therefore, the JH-2 constitutive model was the ceramic model selected for this research. The Johnson-Holmquist ceramic models incorporate a viscoplastic model, a damage model and an EOS. The stress response is determined using Mohr-Coulomb-type yield surfaces described in terms of a scalar damage parameter. The pressure as a function of density and the damage variable is also determined using the

ceramic models. The JH-2 ceramic model was developed by modifying the JH-1 model to account for the gradual-softening behavior that is witnessed when ceramic materials are exposed to flyer-plate impact. The JH-2 ceramic model is commonly used to calculate the depth-of-penetration (DOP) of long rod projectiles into ceramics [45].

The JH-2 strength model makes use of the normalized parameters $\sigma^* = \sigma/\sigma_{HEL}$, $P^* = P/P_{HEL}$, and $T^* = -T/P_{HEL}$ where σ_{HEL} and P_{HEL} are the flow stress and the pressure respectively at the HEL, and T is the minimum pressure that the ceramic can maintain. For a known input quantity of HEL, CTH can find the values of σ_{HEL} and P_{HEL}. In order to be consistent with the way fracture stresses are provided in CTH, the convention for the variable T states that it must be negative. Other codes may differ from this convention [45].

A power-law function can be used to express the normalized flow stress in the following way:

$$\sigma^* = \sigma_i^* - D_{jh}(\sigma_i^* - \sigma_f^*), \tag{3.20}$$

where D_{jh} is the scalar damage variable which can vary from zero for the intact strength to one for the fully fractured strength and σ_i^* and σ_f^* are the intact and fractured normalized flow stresses which are found from the following equations

$$\sigma_i^* = A_{jh}(P^* + T^*)^{N_{jh}}(1 + C_{jh} ln\dot{\epsilon}^*) \tag{3.21}$$

$$\sigma_f^* = min\{B_{jh}(P^*)^{M_{jh}}(1 + C_{jh} ln\dot{\epsilon}^*), SFMAX/\sigma_{HEL}\} \tag{3.22}$$

where $\dot{\epsilon}^* = max\{\dot{\epsilon}_p, 1.0s^{-1}\}$, $\dot{\epsilon}_p$ is the equivalent plastic strain-rate in units of s^{-1}, and A_{jh}, B_{jh}, C_{jh}, M_{jh}, N_{jh} and SFMAX are material constants. The JH-2 model differs from the JH-1 model in that the flow stress changes continuously as damage is incurred in the ceramic [11,45]. The progression of the damage parameter D for every ceramic particle as a function of loading history is found from the damage model.

The equation for the damage model is

$$\dot{D} = \dot{\epsilon}_p / \epsilon_{pf}(P) \tag{3.23}$$

where ϵ_{pf} is the plastic strain at fracture as a function of pressure. ϵ_{pf} can be expressed as the following power-law equation

$$\epsilon_{pf}(P) = D_1(P^* + T^*)^{D_2} \tag{3.24}$$

where D_1 and D_2 are constants [45].

The compression ratio is defined as

$$\mu = \frac{\rho}{\rho_{ref}} - 1 \tag{3.25}$$

where ρ is the density and ρ_{ref} is the reference density. Before failure occurs (D < 1) the relationship between the pressure and volume is

$$P = \begin{cases} K_1\mu + K_2\mu^2 + K_3\mu^3, & \mu > 0 \\ K_1\mu, & \mu \leq 0 \end{cases} \tag{3.26}$$

where K_1, K_2 and K_3 are constants. K_1 is also referred to as the bulk modulus. Once failure has occurred (D $= 1$), the relationship is

$$P = \begin{cases} K_1\mu + K_2\mu^2 + K_3\mu^3 + \Delta P, & \mu > 0 \\ K_1\mu + \Delta P, & \mu \leq 0 \end{cases} \tag{3.27}$$

where ΔP is the bulking pressure. The amount of elastic energy released by the material during failure determines the bulking pressure. With regard to the pressure-volume function, it is assumed that at least a portion of the elastic energy is converted to free energy. In order to calculate the amount of energy released, it is assumed that until failure occurs the deformations are small and that linear elasticity theory can

be used to compute the deviatoric stress as follows

$$[\sigma_d] = 2Ge_{ij} \tag{3.28}$$

where σ_d is the deviatoric stress tensor, G is the shear modulus and e_{ij} is the deviatoric strain tensor. The elastic strain energy that results due to the deviatoric stress, W_d can be calculated from

$$W_d = \frac{1}{2}[\sigma_d] \cdot e_{ij} \tag{3.29}$$

Substituting in Equation (3.28) yields

$$W_d = \frac{1}{4G}|\sigma_{\mathbf{d}}|^2. \tag{3.30}$$

Immediately upon failure, the state of stress goes from the non-failed criteria to the failed criteria. It can be shown that the change in the elastic energy due to deviatoric stress is

$$\Delta W_d \equiv W_d^- - W_d^+ = \frac{(\sigma^-(P^-, \dot{\epsilon}^-))^2 - (Y^+(P^+, \dot{\epsilon}^+))^2}{6G} \tag{3.31}$$

where the - identifies a parameter as having occurred before failure, and the + indentifies a parameter as having occurred after failure. The strain energy release and the bulking pressure can be related in the following way

$$\Delta P\mu^- + \frac{(\Delta P)^2}{2K_1} = \beta \Delta W_d \tag{3.32}$$

where μ^- is the compression just before failure and β is a constant that ranges from 0 to 1. The extent to which the energy released is converted to free energy in the pressure-volume relation is determined by β. Solving Equation (3.32) for ΔP results

in

$$\Delta P = -K_1\mu^- + \sqrt{(K_1\mu^-)^2 + 2\beta K_1 \Delta W_d}. \tag{3.33}$$

In addition to Equations (3.31) and (3.33), the following two equations

$$\Delta P = P^- + P^+ \tag{3.34}$$

and

$$\dot{\epsilon}^+ = \dot{\epsilon}^- \tag{3.35}$$

make up a set of nonlinear algebraic equations where ΔP and ΔW_d are unknowns. The jump in pressure which exists at the moment of failure is assumed to not affect the deviatoric strain-rate, $\dot{\epsilon}$. This assumption results in Equation (3.35). These four equations must be solved iteratively [42].

3.3.3 Johnson-Cook Fracture Model. One method in CTH for failure prediction of metals is achieved using a scalar damage model called the Johnson-Cook fracture model. The Johnson-Cook fracture model and the Johnson-Cook constitutive model are completely independent of one another. "It uses a failure criterion based on equivalent plastic strain, taking into account the pressure, temperature, and strain-rate along the loading path for each material particle [44]." A scalar damage parameter is used in the fracture model as well. In the previous versions of CTH, a stress-based failure criterion existed that did not include any kind of damage parameter. Consider that an elastic-perfectly plastic body experiences movement with constant temperature, T, constant pressure, P, constant deviatoric strain-rate tensor, $\dot{e}_{ij}$ and yield stress, Y. The equivalent deviatoric strain-rate can be stated in the

following way

$$\dot{\epsilon} = \sqrt{\frac{2\dot{e}_{ij}\dot{e}_{ij}}{3}} \tag{3.36}$$

The equation for the equivalent plastic strain-rate is written in terms of the plastic strain-rate tensor $\dot{e}^p_{ij}$ as seen in Equation (3.37)

$$\dot{\epsilon}_p = \sqrt{\frac{2\dot{e}^p_{ij}\dot{e}^p_{ij}}{3}}. \tag{3.37}$$

The equivalent plastic strain at fracture is determined by Johnson and Cook to be

$$\epsilon_{pf}(p, Y, T, \dot{\epsilon}) = [D_1 + D_2 exp(-D_3 p/Y)][1 + D_4 ln(max(1, \dot{\epsilon}))][1 + D_5 T^*] \tag{3.38}$$

where D_1 through D_5 are constants and T^* is the homologous temperature, defined by Equation (3.19). The units of the equivalent deviatoric strain- rate is s^{-1}. Similarly to the JH-2 model, the Johnson-Cook fracture model also has a damage parameter D that accounts for the accumulation of damage and is defined as

$$D = \int \frac{d\epsilon_p}{\epsilon_{pf}(P, Y, T, \dot{\epsilon})} \tag{3.39}$$

When the damage parameter equals one, failure occurs. The Johnson-Cook fracture model assumes that plastic strains are deviatoric; therefore, it is only able to determine failure concerning shear deformation. CTH also simulates the failure caused by excessive hydrostatic tension. This is done in CTH by comparing the current pressure to a fracture pressure, p^f_0. This value is provided by the user, and it must match the value entered for the PFRAC of the material in the FRACTS input block. The assumption that after failure the yield stress goes to zero and that hydrostatic tension cannot be maintained in the material is made in CTH. This means that in CTH the behavior of the failed material is similar to that of a fluid [44].

IV. Characteristics of CTH

Hydrocodes are computer programs that can model wave propagation through solid materials brought about by high velocity impact. Zukas [55] explains that the initial computer codes designed for impact problems relied on the assumption of hydrodynamic behavior and therefore were called "hydrocodes". The hydrodynamic assumption simply says that if the impact velocity produces pressures high enough to exceed the material strengths of the colliding objects, then their material strengths can be ignored, and they can be modeled as fluids. Today the computer codes used for high velocity impact problems are able to account for the material strengths; however, they are still called hydrocodes. With significantly greater ability to model materials, modern hydrocodes are being used to simulate an extensive range of high velocity impact problems such as orbital debris impacting spacecraft [55]. Hydrocodes are typically categorized into two main groups: Lagrangian and Eulerian. These two categories of hydrocodes are discussed in the following sections.

4.1 Lagrangian Hydrocodes

In a Lagrangian hydrocode the mesh is embedded with the material, meaning that the mesh moves and distorts together with the motion of the material. This allows for the material boundaries and interfaces to be clearly identified. Due to the material and the grid deforming together, the Lagrangian hydrocodes can easily determine time histories. Lagrangian codes do not deal with any transport algorithms, which tends to make them more straightforward conceptually than their Eulerian counterparts. When dealing with high velocity impact problems, Lagrangian codes sometimes have serious problems brought about by large distortions in the mesh which makes the time step very small, basically terminating the problem [1].

4.2 Eulerian Hydrocodes

In an Eulerian hydrocode the mesh is fixed in space, and the material flows through the mesh in response to the boundary and initial conditions. Therefore, the

mesh must be large enough to include all the physical space necessary to contain the event including the area that was initially empty to which material may propagate as the solution is carried out [25]. Figure 4.1 shows a comparison of what a Lagrangian and Eulerian mesh might look like for a cylindrical projectile impacting a plate. Because of their fixed mesh Eulerian hydrocodes can model problems where

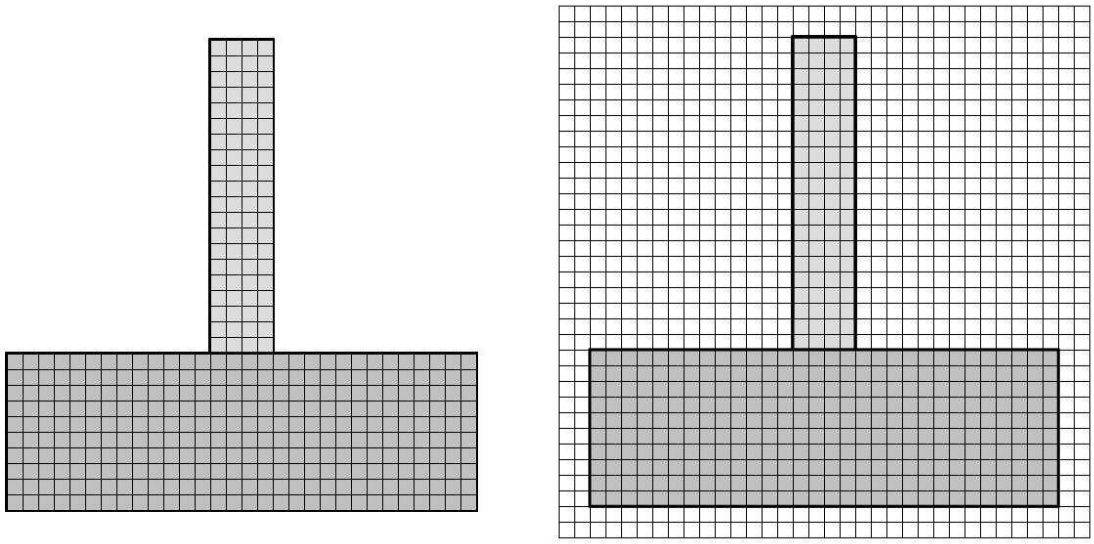

(a) Lagrangian mesh

(b) Eulerian mesh

Figure 4.1: Comparison of meshes for Lagrangian and Eulerian Hydrocodes

large deformations take place without generating mesh distortion problems [55]. The instantaneous state of the material can be determined using Eulerian codes, but no time history data can be gathered without incorporating an additional procedure since the material is flowing through a fixed mesh. Eulerian Hydrocodes can determine mass, momentum, and energy flow across cell boundaries. This allows Eulerian codes to solve problems involving mixing of material; however, this ability can make it difficult to clearly identify material boundaries and interfaces. This research is utilizing the Eulerian hydrocode CTH (version 6.01).

4.3 CTH

CTH is a hydrocode that was designed by Sandia National Laboratories (SNL) to model multidimensional, multi-material, large deformation, strong shock wave physics [22]. In 1969 SNL created a one-dimensional radiation-diffusion hydrodynamic code called Coupled Hydrodynamics and Radiation Transport Diffusion (CHARTD). This developed into the two-dimensional version in 1975 called CHARTD Squared, (CSQ). CSQ led to the three-dimensional version called CSQ to the Three Halves, (CTH) which was initially developed in 1987 and continues to be updated [8]. CTH can analyze several types of problems, such as penetration and perforation, compression, high explosive detonation and initiation phenomena, and hypervelocity impact. In CTH there are six geometry options available: one-dimensional rectangular, cylindrical and spherical geometries; two-dimensional rectangular and cylindrical geometries; and three-dimensional rectangular geometry. A computational cell in CTH can be occupied by void and up to twenty materials [22].

As previously discussed, CTH is an Eulerian hydrocode. In CTH a two-step process is used to solve the conservation equations. The first step is a Lagrangian step in which the Lagrangian forms of the governing equations are integrated across the time step. The mesh deforms with the material, and there is no flow of mass across cell boundaries. The Lagrangian step is followed by a remap step in which the deformed mesh is mapped back to the Eulerian mesh [15]. Further discussion about this two-step process is included in the following sections. All the quantities calculated when solving a problem in CTH are assumed to be constant across each individual cell, and centered within the cell, except velocity. The material velocity, however, is assumed to act on the cell face. All current models in CTH decompose the total stress tensor into the spherical and deviatoric parts. The spherical part of the stress tensor is the equation of state and the deviatoric part of the stress is the constitutive model [8, 22].

4.3.1 Lagrangian Step. Throughout the Lagrangian step, the conservation of mass, momentum and energy must be satisfied. There is no mass flow across the cell boundaries; therefore, conservation of mass is trivially satisfied. The momentum and energy integral equations are replaced by their explicit finite volume representations. While it is possible to solve these finite volume equations, the time step must be chosen such that it is small enough to prevent a wave from crossing a cell in one time step [15, 22].

4.3.2 Remap Step. The appropriate volume, mass, momentum and energy is transferred during the remap step from the deformed mesh to the Eulerian mesh. First the change in the volume from the old to the new cells is calculated. Then it is determined which materials in the old cells are to be moved with the volume change by the use of an interface tracking algorithm. After that, the mass and internal energy of each material is moved between the old and the new cells. Lastly, taking the information from the interface tracking algorithm the momentum and kinetic energies, which are both dependent on mass, are moved between cells. Using a technique called operator splitting, the multi-dimensional differential equations are replaced by several one-dimensional equations [15, 22]. Szmerekovsky [47] covers operator splitting in further detail in his 2004 dissertation.

4.3.3 Material Interface. CTH was originally designed to simulate problems with very high pressures and the presence of strong shock waves. In these types of problems the shear stress tends to be very small compared to the normal stress meaning that material strength is typically unimportant. This justifies the use of relatively crude treatment of interfaces. For problems where a material's ability to sustain shear stresses and tension becomes critical other treatments for the interfaces of materials are necessary. CTH has a few options to handle the interfaces between two materials.

The default option is "no-slip" in which the materials are treated as if they are joined together. The "no-slip" condition is the least complicated of the three options

and requires that the materials at the interface fail under shear in order for slip to occur.

The other two options permit sliding to occur at interfaces by allowing the materials to retain their strength properties, yet move independent of one another. One of these options is the "slide line" option which allows the materials along the interface to keep their strength in tension and compression, but in order to let the materials slide, it sets their shear strength to zero. This technique tends to generate instabilities which yields erroneous results especially in higher impact velocities.

The other option that allows for sliding to occur at the interface is called the Boundary Layer Interface (BLINT) algorithm. This method is currently recommended for two-dimensional axisymmetric problems where the penetration and perforation takes place at velocities below 1.5 km/s. This algorithm is beneficial when simulating munitions designed to defeat armor. The material interface must first be defined. Then the boundary layers need to be defined which consists of the hard and soft boundary layers. The soft boundary layer also includes a slip layer which is used to simulate a frictionless sliding interface. The cells within the slip layer have their flow stresses set to zero even if friction is present. The frictional forces are included as body forces within the cell boundary layers instead of being included through deviatoric stresses. There are also other parameters that are available with this option. For a more in depth look at the BLINT algorithm refer to the appropriate CTH reference manual [41] and the thesis by Capt Nguyen [25].

4.3.4 Boundary Conditions. The conditions of each cell are solved by the finite volume approximations using the conditions from the cells surrounding the cell of interest. However, if the cell being solved for is on the mesh boundary, then it has at least one side that is not surrounded by another cell. Boundary conditions are used for these cells in order to have enough information to solve the finite volume equations [20]. The boundary conditions control the mass, momentum and energy fluxes across the boundaries [32].

There are 4 main boundary conditions available in CTH. The type 0 boundary condition is a symmetry boundary condition that is used to model symmetry and rigid boundaries. This boundary condition should always be used as the origin for cylindrical and spherical geometries. In the boundary cell, all cell centered parameters are set to the values of the adjacent cell in the mesh interior. The velocity between the boundary cell and the mesh interior is set to zero and the associated kinetic energy is converted to internal energy. No flux across the boundaries is permitted with the symmetry boundary conditions.

The type 1 boundary condition is a sound speed based absorbing boundary condition in which mass is allowed to flow in and out of the mesh. This boundary condition is used to approximate an infinite or semi-infinite medium. It can account for fragments moving through the mesh boundaries; however, it was not designed to handle this well.

Type 2 is called the outflow boundary condition. This boundary condition puts an empty cell on the boundary and fills it with void. The void fraction is defined as one in the boundary cell such that the boundary pressure equals the user prescribed void pressure. Mass is allowed to leave the mesh, but no mass can enter the mesh.

The last of the main boundary conditions is the Type 3 boundary condition. This boundary condition, known as the extrapolation boundary condition, linearly extrapolates the boundary pressure from the interior of the mesh. If the extrapolated pressure is tensile, then it is set to zero. Mass is permitted to flow into and out of the mesh. The pressure-extrapolating absorbing boundary condition is better at absorbing fragments and projectiles leaving the mesh [23, 32].

4.3.5 Convection Input. CTH is not able to conserve both momentum and kinetic energy during the remap step; therefore, CTH provides a few different options that the user can specify to take care of this problem. With all four options conservation of momentum is satisfied. Option 0, which is the default, discards the kinetic energy and convects internal energy. It uses the slope determined from the

internal energy density and the slope mass density to convect the internal energy. Option -1 is a variant of option 0 which also discards the kinetic energy and convects the internal energy; however, the internal energy is convected by utilizing the slope of the internal energy versus the mass. In the final two options the total energy is convected while the kinetic energy is subtracted off after the remap step. In option -2 the kinetic energy is described by cell-centered velocities. Option -3 on the other hand characterizes a cell-centered kinetic energy and then subtracts it off. According to the reference manual, option 0 generally provides good results for most problems so this option was used in this research. [32].

There are three material tracking interface algorithms available in CTH. The volume fraction data is used to calculate the material interfaces. The default method uses what is called the Simple Line Interface Construction (SLIC) algorithm. SLIC takes into account the materials that are present in the cell directly ahead of and behind the donor cell. The tendency to orient interfaces parallel and perpendicular to the direction of the flow exists with this method. The interfaces can then be distorted at an angle to the direction of the flow. Another option for tracking the material interfaces is known as the High Resolution Interface Tracking (HRIT) algorithm. This algorithm considers the materials that are present in all of the neighboring cells. HRIT is the recommended option for two-dimensional problems. The third interface available in CTH is known as the Sandia Modified Young's Interface (S-MYRA) tracking algorithm. It also takes into account the materials present in all the neighboring cells. S-MYRA can be used in two and three-dimensional problems; however, it is the recommended option for three-dimensional problems [32].

4.3.6 Mixed Material Cells. Multiple pressures and temperatures can exist in a given cell due to mixing of materials during an impact event. CTH has the ability to deal with this through the use of a few different options which are designated in CTH by the identifier MMP. The default option for this identifier is MMP0 which allows each material to have its own temperature and pressure. This selection does

not contain a mechanism that allows pressure relaxation. Based upon the material volume fractions in the cell, this option distributes the volume and energy, which can cause problems when materials in a mixed cell have differences in compressibility. The next choice available with the MMP identifier is MMP1 which treats mixed cells similar to the MMP1. However, MMP1 bases the distribution of the volume and energy on the material volume fraction cubed divided by the material mass in the cell. MMP2 option is the third option available which allocates that the work done on a cell of mixed material is dependent specifically on the compressibility of the materials in that cell. This method allows for relaxing of the pressure between materials in a cell. MMP2 should give better results than the first two options for some problems; however, numerically, it is less robust. The final selection related to the MMP identifier is MMP3 where the work done on a mixed material cell allocated is proportional to the volume fraction of the material. This option also allows for pressure relaxation between materials in a cell. It does this in such a way that does not permit materials with very small volume fractions to change volume [32].

Another issue dealing with mixed material cells that needs to be taken into consideration is how to determine the strength of the mixed materials. CTH provides three models for calculating the material strength in mixed cells. The identifier MIX is used to designate all three options. The first model referred to as MIX=1 uses the sum of the volume fraction weighted yield strengths of the mixed materials to the cell yield strength. Mixed cells containing a single material and void will have a decreased yield strength with this option because the material volume fraction is less than one. The next model in CTH is MIX=3 which uses the volume averaged yield strengths divided by sum of the volume fractions of the materials that are able to support shear. In this case, mixed cells with only one material and void will have the yield strength of the material. This option gives the best results for many problems. The final option is MIX=5 which sets the yield strength to zero in mixed cells except for the case of a cell that consists of one material and void. For this specific case,

a volume weighted average is used similar to MIX=1. When modeling frictionless interfaces where BLINT is not used, MIX=5 is typically the preferred model [32].

4.3.7 Artificial Viscosity. It is assumed that there are no jumps in the physical properties within a continuum; however, in simulations where a shock wave is formed, there are in effect instantaneous discontinuities in density, pressure and velocity. In order to allow CTH to handle discontinuities caused by shock waves in the Lagrangian time step, artificial viscosity is utilized. Artificial viscosities are numerically defined artificial values added to the pressures in order to smear the discontinuities caused by shock waves in continuum based codes over several mesh widths. The artificial viscosity does distort the solution; however the solution is only affected near the shock front and the accuracy of the calculation is preserved [55].

A vector subset of the full viscosity tensor with linear and quadratic terms including the diagonal elements xx, yy, and zz is the form used to control shocks. A singular point in the update of the stress deviators at the axis-of-symmetry for the two-dimensional cylindrical geometry option is controlled by a third linear viscosity term. Non-physical oscillations sometimes seen in normal penetration simulations can often be controlled by the shear viscosity term [15].

4.3.8 Graphical Data. CTH depends greatly on plots to display post-processing data. CTH contains two types of basic graphics post-processors. One type is CTHPLT which is used to produce material plots. CTHPLT can generate one, two and three-dimensional plots in black and white or color. The material plots consist of either contour or vector plots of various properties versus position for a given time. The other type is HISPLT which outputs time-history plots. HISPLT requires Lagrangian tracer points be defined during the pre-processing phase. Time-history plots consists of plots of as variety of properties at the predefined tracer points versus time. This means that some foresight and knowledge is necessary in order to determine the area of interest for the placement of the tracer points.

V. CTH Solution Method

This chapter presents the numerical set-up for the CTH input files that were run which consists of: three sample runs, multi-layer target runs, and ceramic armor runs. Included in this chapter are the materials used, EOS and constitutive models, impact velocities, mesh, projectile and target geometries and any CTH algorithms that were taken into consideration.

The development of a multi-layer ceramic and metallic armor began with evaluating a few specific features of CTH by running three sample input files from SNL. These input files focused on the JH-2 ceramic model, the Johnson-Cook fracture model and the boundary layer algorithm. These example problems were chosen because they all contained some vital model or algorithm that was being used to accurately model the multi-layer target of interest. These problems were attempted merely to become familiar with CTH and some of the algorithms that are available. Once some confidence was gained on how to set-up and run CTH input files, the multi-layer target problem from Zukas & Scheffler [56] and Zukas [55] was attempted. This was followed by a confined ceramic problem from Westerling, Lundberg & Lundberg [49]. This problem was followed by the ceramic armor problem which was the focus of this research effort. All of these previous runs were performed in order to develop the method for modeling the ceramic armor problem.

All of the simulations performed were simulated using a two-dimensional, cylindrical axisymmetric model where only half of the geometry and mesh were modeled, and then the results were mirrored during the post-processing phase. In the convection block of each of the input files, the option convection=0 was used as it typically gives good results for most problems. Since the HRIT algorithm is recommended by SNL for two-dimensional simulations it was used in the following problems. The MMP3 option was applied to designate multiple pressures and temperatures in mixed material cells because it provides good results for many different impact problems, is fairly robust and allows for pressure relaxation. Since the MIX=3 option gives the best results for most problems it was used in most of the cases; however, the MIX=5

option was used in a few runs where the BLINT algorithm was not used to model a frictionless interface as a comparison to the MIX=3 option. For every simulation run, the initial reference temperature was 2.56798095E-02 electron volts or 298 K (1 eV = 11604.5 K). The consideration of the Boundary Layer Interface algorithm and the boundary conditions is discussed in Chapter VI.

5.1 Multi-Layer Target Example

The multi-layer example from Zukas and Scheffler [56] and Zukas [55] considered here involves a cylindrical projectile made of S7 tool steel impacting a multi-layered, cylindrical target made of rolled homogeneous armor (RHA) at 1164 m/s. Figure 5.1 shows one configuration of the target consisting of six layers. Simulations were also performed for the same target divided into one, two and four layers as well.

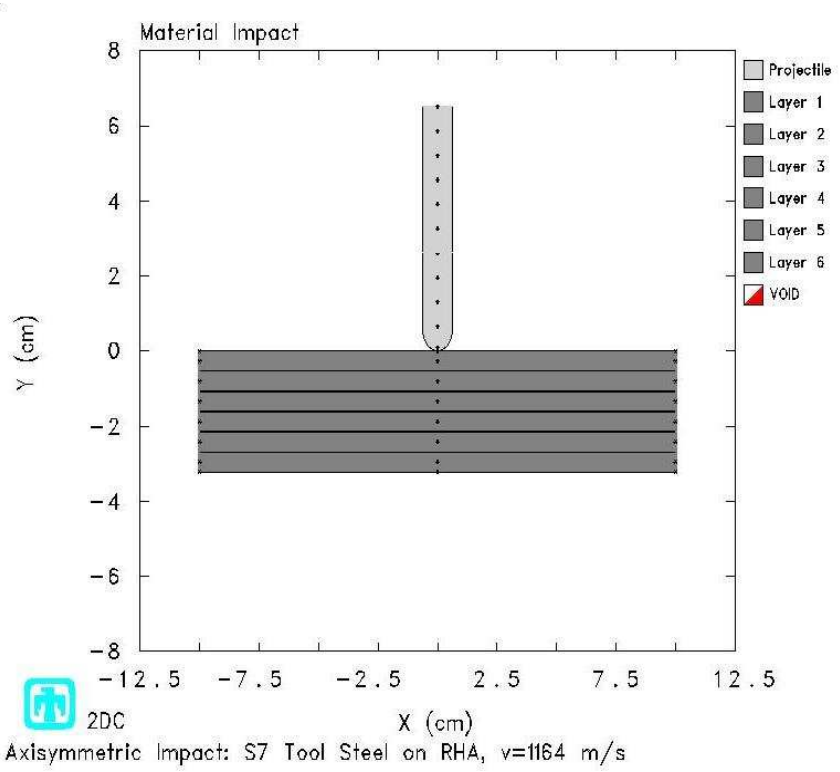

Figure 5.1: Impact of S7 tool steel projectile on a multi-layer target made of RHA

5.1.1 Dimensions. The projectile has a hemispherical nose and a mass of approximately 65 grams. It has a diameter of 1.3 cm and a L/D of 5 giving it a length of 6.5 cm. The RHA target has an overall thickness of 3.18 cm and a diameter of about 20 cm. The total target thickness is 3.18 cm. The dimensions for this problem are depicted in Figure 5.2. This figure shows the six-layer target configuration in which each layer has an equal thickness of 0.53 cm. The one, two and four-layer configurations all have the same total target thickness, but the individual layers have different thicknesses. The individual layers in a given target configuration are of equal thickness. This means that the thickness of the layers in the four-layer and two-layer targets are 0.795 cm and 1.59 cm, respectively, and the thickness of the layer in the one-layer target is obviously equal to the total target thickness of 3.18 cm.

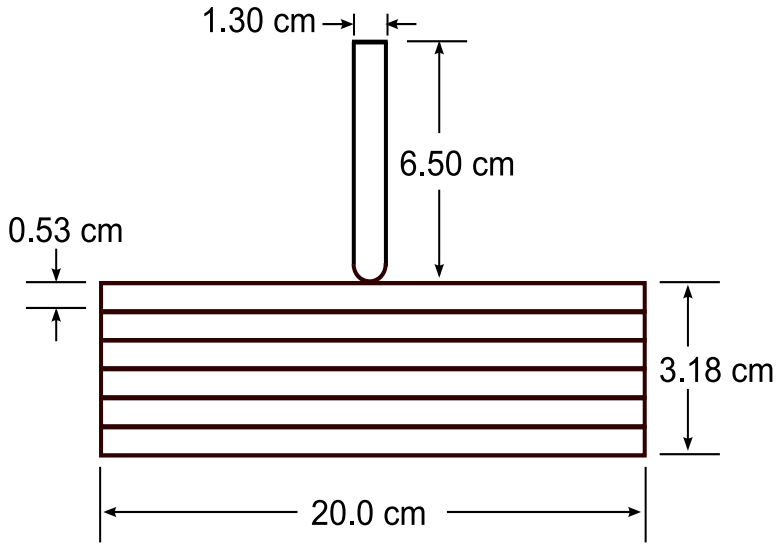

Figure 5.2: Dimensions for steel projectile impact on a multi-layer RHA target

5.1.2 Mesh. The mesh as modeled here consists of cells that are 0.04 cm wide by 0.04 cm long. There are a total of 95,250 cells where 92,250 are real cells in the mesh and 3,000 are boundary cells. Of the 92250 real cells in the mesh, 19,875 cells are in the target, approximately 2,641 are in the projectile and the remaining 69,734 cells make up what is left of the mesh.

In order to model sliding between the layers using the Eulerian code CTH, Zukas and Scheffler add a gap between each layer of 0.01 cm. This same method was employed in the simulations here using CTH. When a free surface between layers exists, stress waves cannot transmit across; however, this gap is kept so that it is smaller than the size of the cells in the mesh, effectively including free surfaces created by the gaps in mixed cells. This will allow the stress waves to pass between the plates as if they were actually in contact.

5.1.3 EOS and Constitutive Models. In version 6.01 of CTH, there is no EOS available for S7 tool steel. The closest material available is iron which is very close to S7 tool steel in terms of equation-of-state. Therefore, the SESAME EOS for iron was substituted in for S7 tool steel in these simulations. CTH does have a RHA identifier available for the SESAME EOS; however, when this identifier is applied, it directs CTH to use the properties for iron as can be seen in Table 5.1 by the fact that the elastic properties listed for both S7 tool steel and RHA are the same. As for the constitutive models, CTH does contain the Johnson-Cook viscoplastic model for both S7 tool steel and RHA. In CTH versions prior to 8.0, using the Johnson-Cook viscoplastic model for a material could result in the Tmelt value being replaced by a default value that may or may not correspond well with reality. For the steel materials used in these problem, CTH defaulted to a Tmelt equal to 1.284E-01 eV. To prevent this from happening Tmelt was set to 1 eV for all problems using the Johnson-Cook viscoplastic model. Table 5.2 shows the Johnson-Cook constitutive model coefficients for the projectile and the target.

Table 5.1: Elastic properties for S7 tool steel and RHA

Material Property	S7 tool steel	RHA
Density (g/cm^3)	7.8724	7.8724
Sound Speed (km/s)	4.6058	4.6058
Poisson's Ratio	0.283	0.283
Elastic Modulus (dyne/cm^2)	1.6700E+12	1.6700E+12
Shear Modulus (dyne/cm^2)	6.5082E+11	6.5082E+11

Table 5.2: Johnson-Cook viscoplastic coefficients for S7 tool steel and RHA

Coefficient	S7 tool steel	RHA
A (dyne/cm^2)	1.5401E+10	1.8320E+10
B (dyne/cm^2)	4.7679E+09	1.6850E+10
C	1.2000E-02	4.3500E-03
m	1.0000E+00	8.0000E-01
n	1.8000E-01	7.5400E-01
T_{melt} (eV)	1.5407E-01	1.5365E-01

The coefficients for the Johnson-Cook fracture model for the projectile and target are shown in Table 5.3. Using these material properties, constitutive models and EOS, this impact problem was simulated and then compared with the results produced from the Lagrangian code ZeuS [55, 56].

Table 5.3: Johnson-Cook fracture coefficients for S7 tool steel and RHA

Coefficient	S7 tool steel	RHA
D_1	-8.0000E-01	-1.0000E+00
D_2	2.1000E+00	1.2500E+00
D_3	-5.0000E-01	-5.0000E-01
D_4	2.0000E-03	1.0000E-03
D_5	6.1000E-01	9.8000E-01
T_{melt} (eV)	1.5665E-01	1.5500E-01
p_0^f (dyne/cm^2)	-2.000E+10	-1.500E+10

5.1.4 Multi-Layer Target Example without Gaps. The ceramics that are used in armor are typically bonded to a metal. Taking this into consideration, the problem above was modified by removing the gap between the plates. Now, instead of the plates being free to slide, they act as if they are bonded together like the ceramic armor. Both of these cases were run for a various velocities in order to determine the ballistic limit for each. The same material properties, EOS, constitutive models and CTH parameters utilized for the model with gaps between the layers were used for these runs as well.

5.2 Confined Ceramic Example

From an earlier discussion, it is known that ceramics in general are strong in compression and weak in tension; therefore, it becomes important to confine the ceramic with a material that is strong in tension. In order to show that CTH can model projectile impact of a confined ceramic target with reasonable accuracy, one portion of the problem considered by Westerling, Lundberg and Lundberg [49] was modeled. This problem consists of a cylindrical tungsten projectile impacting a cylindrical boron carbide (B_4C) ceramic target that is completely encased by a tempered steel tube that has material properties comparable to 4340 steel. This simulation is run for a variety of velocities ranging from 1454 - 2555 m/s.

This problem was modeled using experimentation and numerical simulation. In the experiment, the reverse-impact technique was used where the target is fired horizontally from a gas gun into the projectile. For the purposes of the simulation performed here, the projectile impacts vertically downward on the target (Figure 5.3). The simulation of this problem was performed using the Lagrangian Hydrocode AUTODYN-2D.

5.2.1 Dimensions. The case looked at here uses a thickness equal to 0.2 cm for the steel confinement on the sides. The top and bottom steel plugs have a thickness of 4 mm each and a diameter of 1.9 cm. The 0.2 cm thick steel tube that confines the ceramic is 4.76 cm in length; this oversize length is so that the front and rear plugs are also covered. The B_4C ceramic has a diameter equal to the diameter of the metal plugs and a length of 3.96 cm. The projectile has a diameter of 0.2 cm and a length of 15 cm. Figure 5.4 shows the dimensions for both the projectile and the target.

5.2.2 Mesh. Initially, the schematic shown in Figure 5.5 was used to depict the size of the cells in different regions of the mesh; this diagram is not to scale. As would be expected, the finest part of the mesh is in the impact zone where the mesh is

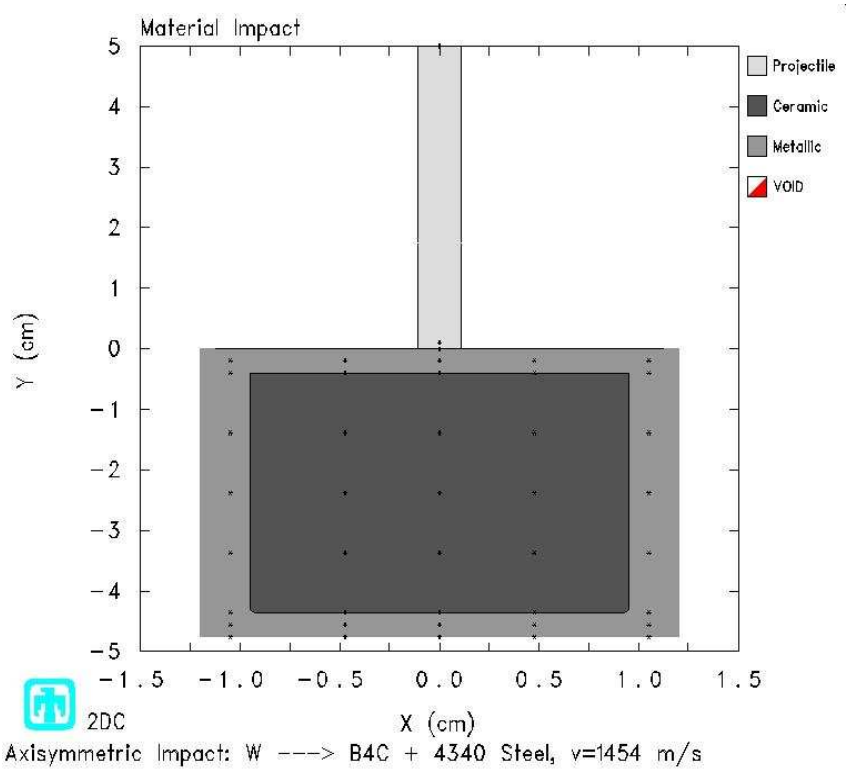

Figure 5.3: Impact of tungsten projectile on a boron carbide target confined by steel

0.01 cm wide by 0.01 cm long. Away from the impact zone, the mesh is more coarse. There are a total of 17,952 cells where 16,492 are real cells in the mesh and 1,460 are boundary cells. The regions of constant cell sizes result in a large mismatch in cell size where the different regions come together. This can cause some local problems where these different cell sizes meet. In order to avoid this error, CTH allows you to designate the width of the first and last cells in a mesh region. Then CTH gradually transitions from the width of the first cell to the last cell in a manner that prohibits the cells from having large mismatches in width. A good rule of thumb is that the ratio of the width of a cell compared to an adjacent cell should be approximately 0.95 to 1.05 [9]. The updated mesh used for this problem is generated by employing the method just discussed. It transitions from a cell width of 0.01 cm to 0.05 cm in the x direction going from left to right. In the y direction, the cell width starts at 0.1 cm at the bottom of the target, reduces to 0.01 cm at the area of impact, and then increases

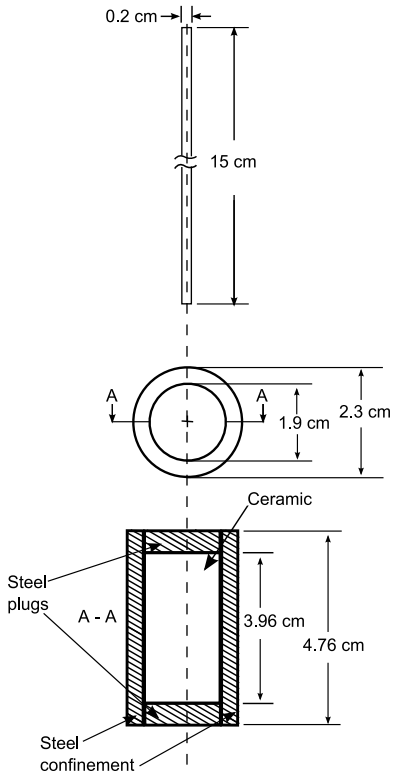

Figure 5.4: Dimensions of tungsten projectile impact on a confined boron carbide target [49]

to 0.05 cm at the top of the projectile. There are a total of 51,540 cells where 49,358 are real cells in the mesh and 2,182 are boundary cells.

5.2.3 EOS and Constitutive Models. For the tungsten projectile, the respective SESAME tabular EOS was used. The 4340 steel SESAME EOS was used for the steel confinement which uses the properties for iron. For the B_4C, the JH-2 model for ceramics was used for the EOS, the constitutive model and the damage model. The JH-2 parameters for B_4C are shown in Table 5.4. Table 5.5 shows the elastic properties for tungsten, 4340 steel and B_4C. The Johnson-Cook viscoplastic model are used for tungsten and 4340 tempered steel. Table 5.6 lists the Johnson-Cook constitutive model coefficients for the projectile and the target.

Johnson-Cook fracture models were used to model the damage for the tungsten projectile and the steel confinement. The coefficients for the Johnson-Cook fracture

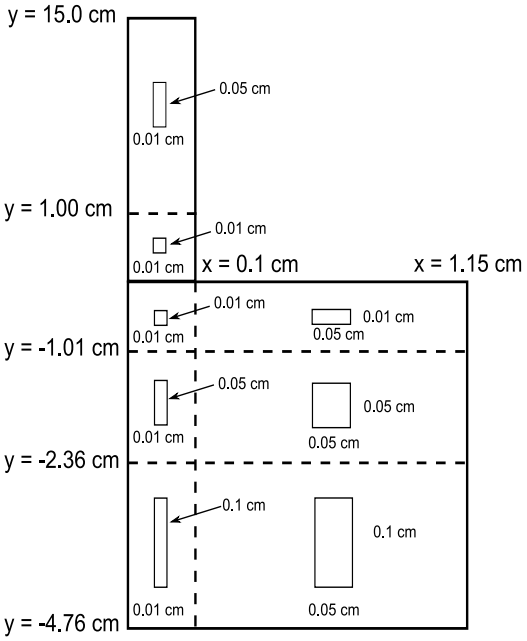

Figure 5.5: Mesh for tungsten projectile impacting a confined boron carbide target

Table 5.4: JH-2 coefficients for boron carbide

Coefficient	boron carbide
A	9.270E-01
B	7.000E-01
C	5.000E-03
M	8.500E-01
N	6.700E-01
D_1	1.000E-03
D_2	5.000E-01
β	1.000E+00
C_v (erg/[eV $\cdot$ g])	2.570E+11
HEL (dyne/cm^2)	1.900E+11
K_1 (dyne/cm^2)	2.330E+12
K_2 (dyne/cm^2)	-5.930E+12
K_3 (dyne/cm^2)	28.000E+12
p^f (dyne/cm^2)	-2.600E+09
SFMAX (dyne/cm^2)	3.088E+10

model for the both these materials are shown in Table 5.7. The material properties, constitutive models and EOS shown here in these tables were used to simulate the

Table 5.5: Elastic properties for tungsten, 4340 steel, and boron carbide

Material Property	Tungsten	4340 Steel	Boron Carbide
density (g/cm^3)	17.6000	7.8724	2.5100
Sound Speed (km/s)	3.9921	4.6058	14.0077
Poisson's Ratio	0.280	0.283	0.250
Elastic Modulus (dyne/cm^2)	3.0686E+12	1.6700E+12	4.9250E+12
Shear Modulus (dyne/cm^2)	1.1987E+12	6.5082E+11	1.9700E+12

Table 5.6: Johnson-Cook viscoplastic coefficients for tungsten and 4340 steel

Coefficient	Tungsten	4340 Steel
A (dyne/cm^2	1.5070E+10	2.1000E+10
B (dyne/cm^2	1.7664E+09	1.7500E+10
C	1.6000E-02	2.8000E-03
m	1.0000E+00	7.5000E-01
n	1.2000E-01	6.5000E-01
T_{melt} (eV)	1.5062E-01	1.5365E-01

aforementioned impact problem. The results were then compared with both the experimental and simulation data that Westerling, Lundberg & Lundberg [49] produced.

Table 5.7: Johnson-Cook fracture coefficients for tungsten and 4340 steel

Coefficient	Tungsten	4340 Steel
D_1	0.000E+00	-8.000E-01
D_2	3.300E-01	2.100E+00
D_3	-1.500E+00	-5.000E-01
D_4	0.000E+00	2.000E-03
D_5	0.000E+00	6.100E-01
T_{melt} (eV)	1.284E-01	1.284E-01
p_0^f (dyne/cm^2)	-2.000E+10	-2.000E+10

5.3 Ceramic Armor

This simulation is an extension of the multi-layer and the confined ceramic problems discussed previously. It consists of a cylindrical S7 tool steel projectile with a hemispherical tip striking a cylindrical target composed of boron carbide ceramic and a rolled homogeneous armor casing. Various arrangements of the RHA and B_4C were evaluated at several different velocities. Initially, the target consisted one layer of B_4C

that was confined completely by RHA. The three additional arrangements of armor have two, three and four times more ceramic than the first arrangement; however, the overall thickness of each target is the same. All four target configurations are shown in Figures 5.6 (a)–(d).

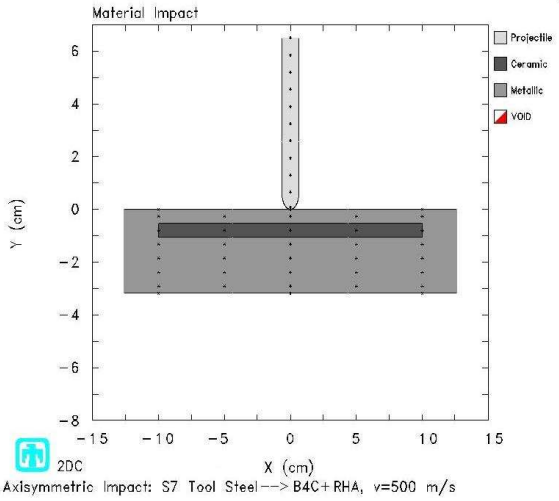

(a) One-layer ceramic armor

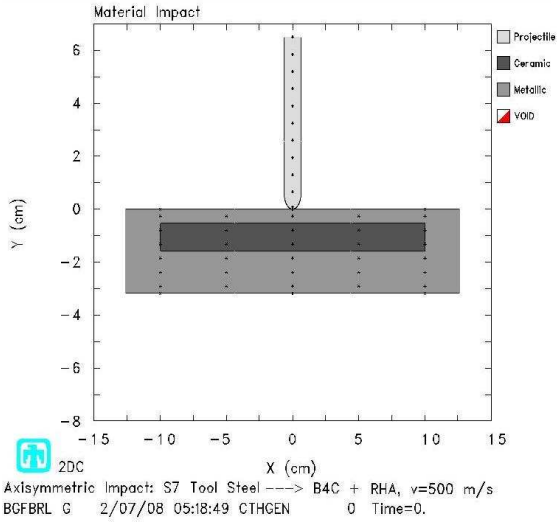

(b) Two-layer ceramic armor

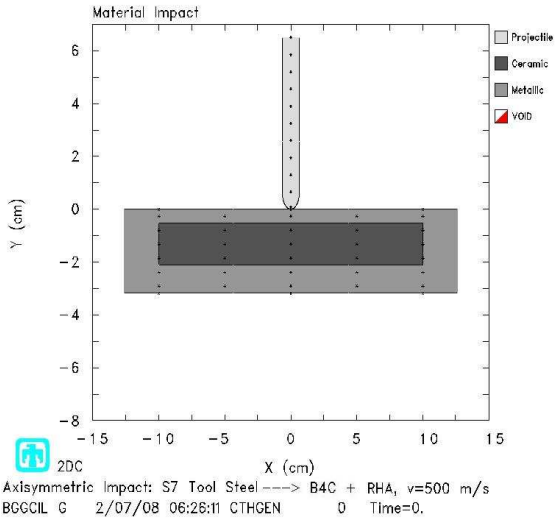

(c) Three-layer ceramic armor

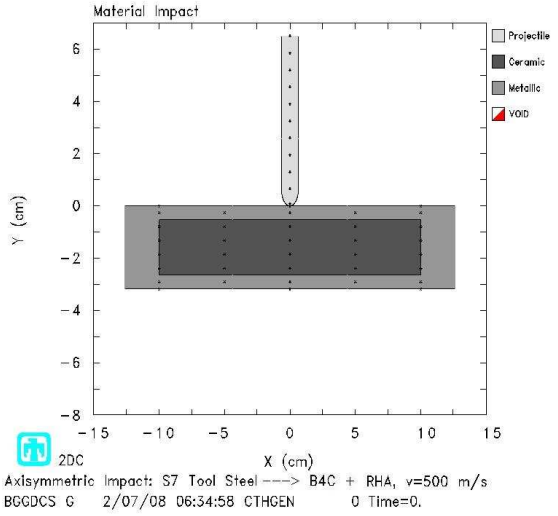

(d) Four-layer ceramic armor

Figure 5.6: Impact of S7 tool steel projectile on a boron carbide target confined by steel

5.3.1 Dimensions. Initially as shown in Figure 5.7, the dimensions are given for the armor arrangement that consists of one layer of ceramic (same arrangement as Figure 5.6 (a)) that is 0.53 cm in thickness and 20 cm in diameter. Like the multi-layer problem the overall thickness of the target is 3.18 cm. The top plug of RHA is also 0.53 cm thick. The overall target diameter is now larger due to the side confinement tube which is 2.56 cm wide and covers both the top and bottom plugs. The projectile consists of a hemispherical tip and has the same dimensions as in the multi-layer problem. For the other arrangements of the armor, the amount of ceramic was increased by 0.53 cm for each additional layer while the overall thickness of the target remained the same.

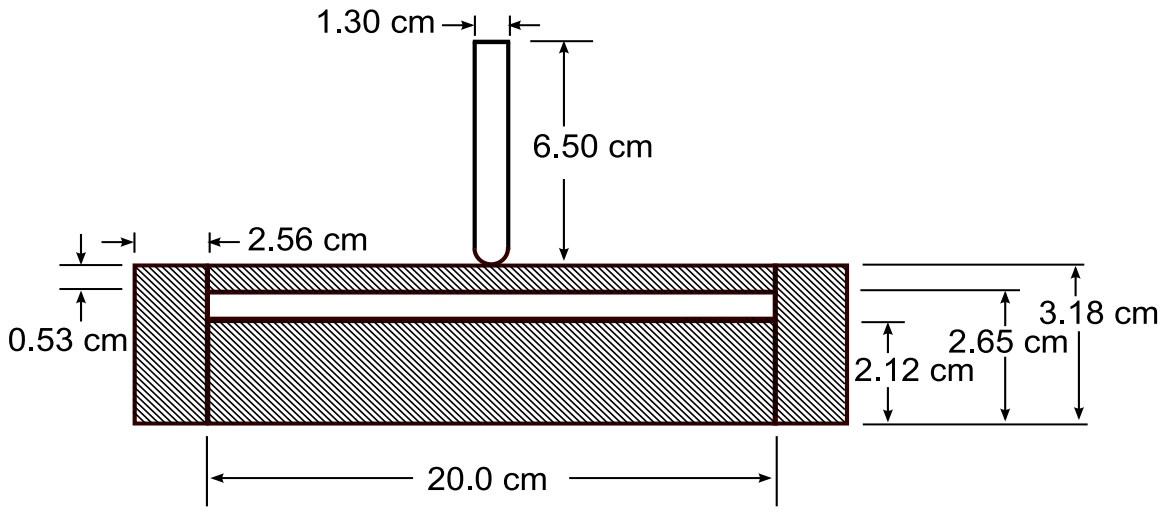

Figure 5.7: Dimensions of S7 tool steel projectile impact on a confined boron carbide target

5.3.2 Mesh. The mesh is shown schematically in Figure 5.8; this figure is not drawn to scale. The area of the initial impact is again where the finest part of the mesh is located. In this area the mesh is 0.01 cm wide by 0.01 cm long. Farther from the region of the impact, the mesh is more coarse. There are a total of 126,900 cells where 123,432 are real cells in the mesh and 3,468 are boundary cells. Of the 123,432 real cells in the mesh, approximately 41,255 cells are in the target, 15,210 are in the projectile and almost 66,967 cells make up the remainder of the mesh. As previously

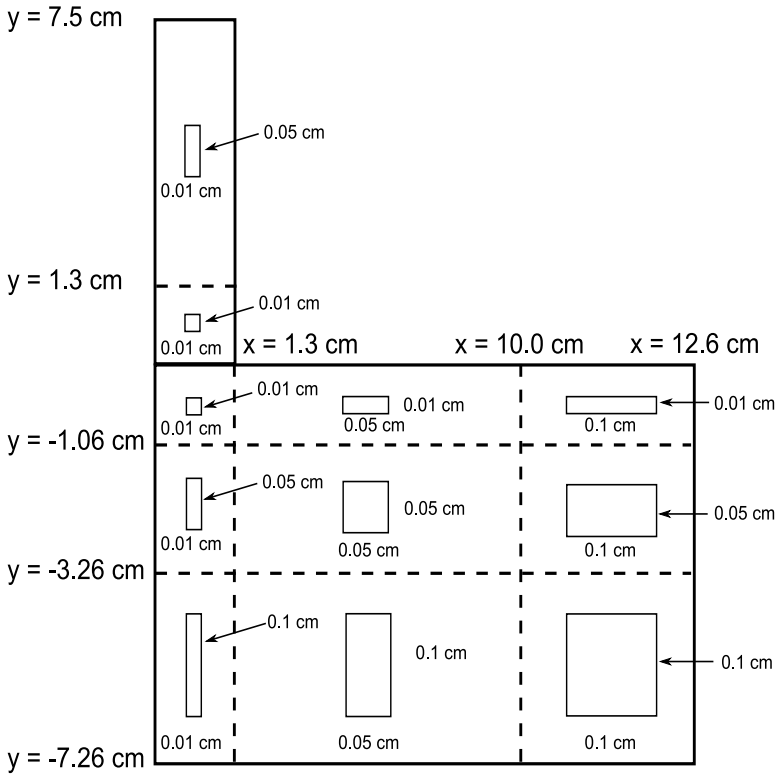

Figure 5.8: Mesh of S7 tool steel projectile impact on a confined boron carbide target

discussed, large mismatches in cell size can exist where mesh regions of constant cell sizes meet. Errors caused by these mesh mismatches can result. Typically, these errors will be confined to the area of the poor meshing so that the overall global results will be fairly accurate; however, there are other factors that play into the resulting effect of the mesh errors.

The method of meshing that allows a smooth transition between mesh regions is the ideal approach as discussed in Section 5.2.2. The mesh recommended for this problem transitions from a cell width of 0.01 cm to 0.1 cm in the x direction going from left to right. In the y direction, the cell width starts at 0.1 cm below the target, reduces to 0.01 cm at the area of impact, and then increases to 0.05 cm at the top of the projectile. This would result in 329,724 real cells contained in the mesh, and 9,836 boundary cells exist giving a total of 339,560 cells. This mesh is shown in the sample

input file in Appendix A.3. Due to the amount of computational time required to run these simulations, these problems were not run again with this new mesh.

5.3.3 EOS and Constitutive Models. The SESAME EOS for iron was once again used for S7 tool steel. The RHA SESAME EOS state was used for the steel confinement; however, as mentioned previously, this EOS actually uses the same values as those used for iron. For the B_4C ceramic, the JH-2 model was still used to describe the behavior of the material. The JH-2 parameters for B_4C are shown in Table 5.4. As a reminder, the elastic properties for the S7 tool steel, RHA and B_4C are listed in Tables 5.1 and 5.5. Just like before, the Johnson-Cook viscoplastic models for S7 tool steel and RHA were used. Table 5.2 shows the Johnson-Cook constitutive model coefficients for the S7 tool steel and RHA. Johnson-Cook fracture model coefficients for the S7 tool steel projectile and the RHA steel confinement are shown in Table 5.3. The material properties, constitutive models and EOS shown in these tables were used for all of the arrangements of the ceramic armor simulations.

VI. Analysis and Results

This chapter presents the results for the simulations laid out in the previous chapter. These simulations will be discussed in terms of depth of penetration and residual velocity. Graphics will be shown of material impact and pressure, as well as time dependent plots of position and residual velocity of the projectile tip.Most of the graphics shown here are produced using the post processors CTHPLT and HISPLT.

6.1 Multi-Layer Target Example

6.1.1 Boundary Layer Algorithm. One numerical scheme that needed to be considered was the Boundary Layer Interface algorithm. As stated earlier, the BLINT algorithm should provide good results for penetration and perforation problems where the impact velocity is below about 1.5 km/s. The multi-layer target problem that was laid out in the previous chapter was run using BLINT in which the projectile was identified as the hard material in this algorithm, and the target was identified as the soft material. According to the results from the ZeuS code used by Zukas and Scheffler [56], for a impact velocity of 1164 m/s, the target made up of six layers should have a normalized residual velocity of about 0.54. In this case, they have normalized the residual velocity by dividing it by the impact velocity, which leads to a residual velocity of approximately 629 m/s. When this simulation was performed using the BLINT algorithm in CTH, some spall was created at the bottom of the target; however the projectile failed to perforate the target. The projectile only penetrated into the second layer, refer to Figures 6.1. Figure 6.2 shows the vertical position of the projectile tip throughout the penetration process.

There are a few additional options available for use with BLINT. For a Coulomb friction coefficient other than 0, it is necessary to specify this value when using BLINT. Through experimentation, Bowden and Freitag [6] determined that as the relative velocity on a metal-to-metal interface increases, the resistance to sliding decreases. Some minimum frictional coefficient greater than zero and varying from 0.20 for steel

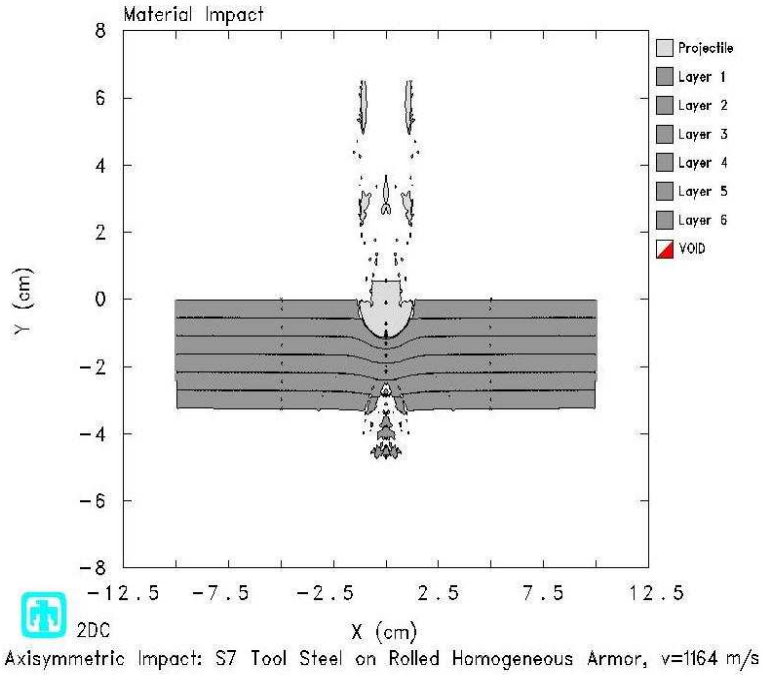

Figure 6.1: S7 tool steel projectile impacting RHA target with gaps at 1164 m/s using BLINT algorithm(180 μs)

on aluminum to 0.05 for steel on bismuth was proposed based on the data [6,25]. Using this information as a guideline, the simulation was rerun with a frictional coefficient equal to 0.20; however, the outcome was virtually identical as seen from Figures 6.3 and 6.4.

Another option to consider in BLINT is referred to as CORR. This option has been introduced to reduce numerical noise and errors that can lead to permanent deformation of the penetrator. CORR increases the yield strength of the projectile material by a factor that is dependent on the thickness of the boundary layer. This increase in projectile strength accounts for the increase in the effective cross-sectional area caused by the use of a slip layer in the calculation. This scheme only applies to axisymmetric problems simulating normal impact of a penetrator on a target. For the penetration and perforation problem where the penetrator remains nearly undeformed, this option is recommended [33, 41].

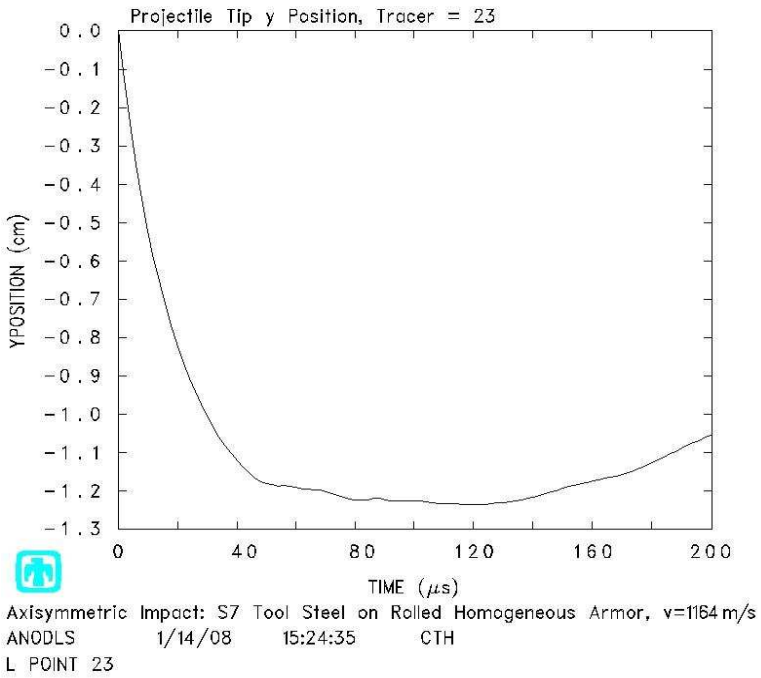

Figure 6.2: Vertical position of projectile tip impacting RHA target with gaps at 1164 m/s using BLINT algorithm

Figures 6.5 and 6.6 show the results of using the CORR option. The projectile penetrates approximately the same amount as in the first two cases. There are, however, a couple of noticeable differences from the earlier results. First of all, the shape of the spall fragmentation is slightly different. But even more apparent is the way the projectile deformed. Instead of the impacted end of the projectile being hemispherical in shape and resembling a mushroom cap like the previous two cases, it almost completes a full sphere, except towards the top on either side of what is left of the projectile shaft there are little points protruding. There were also fewer fragments coming off the projectile in this case.

The last option that was considered dealing with the BLINT algorithm is known as NOFREEZE. Typically, the tangential component of velocity in the slip layer is frozen (set equal to zero) if CTH detects flow within the slip layer opposite to the velocity of the material in the hard boundary layer. This is accomplished to prevent the projectile from melting through the target at low velocities when the projectile is

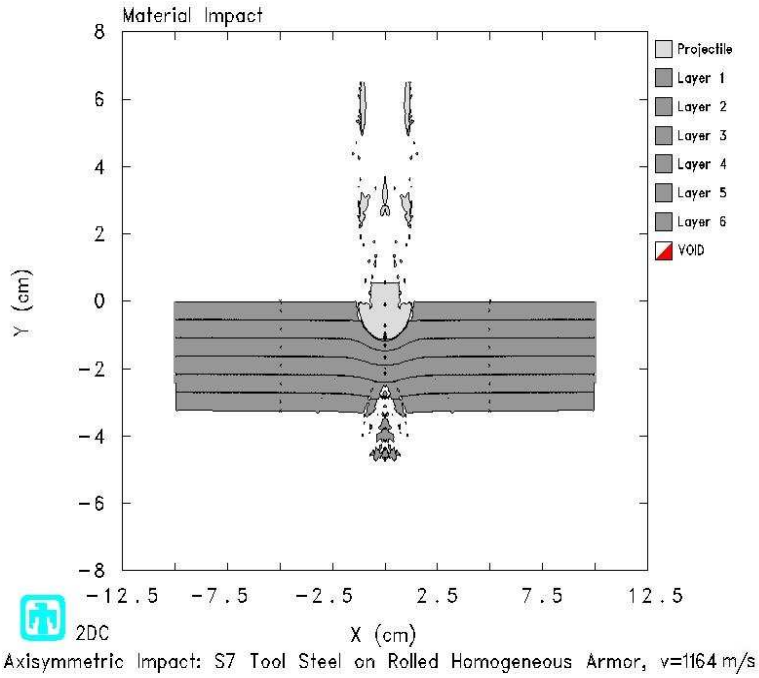

Figure 6.3: S7 tool steel projectile impacting RHA target with gaps at 1164 m/s using Coulomb friction of 0.2 in BLINT algorithm (180 μs)

coming to a rest. NOFREEZE turns off this freezing scheme. This can sometimes be useful in simulations where the target consists of multiple layers of different materials. This option is taken into account in the ceramic armor simulations where where multiple materials are being used in the target and the velocities are low enough to warrant the use of the BLINT algorithm.

Next this simulation was run without using the BLINT option in order to evaluate whether using BLINT made a difference or not for this problem. From Figures 6.7 and 6.8, it is observed that the projectile penetrated even less than in the previous cases.

As discussed earlier in Subsection 4.3.6, MIX=5 is recommended for modeling frictionless interfaces when BLINT is not being used. Therefore, this change was made and the problem was rerun. Figure 6.9 shows the progression of the projectile in time as it actually penetrates all the way through the plate. The corresponding pressures at these times are shown in Figures 6.10 through 6.13. In CTH, compression

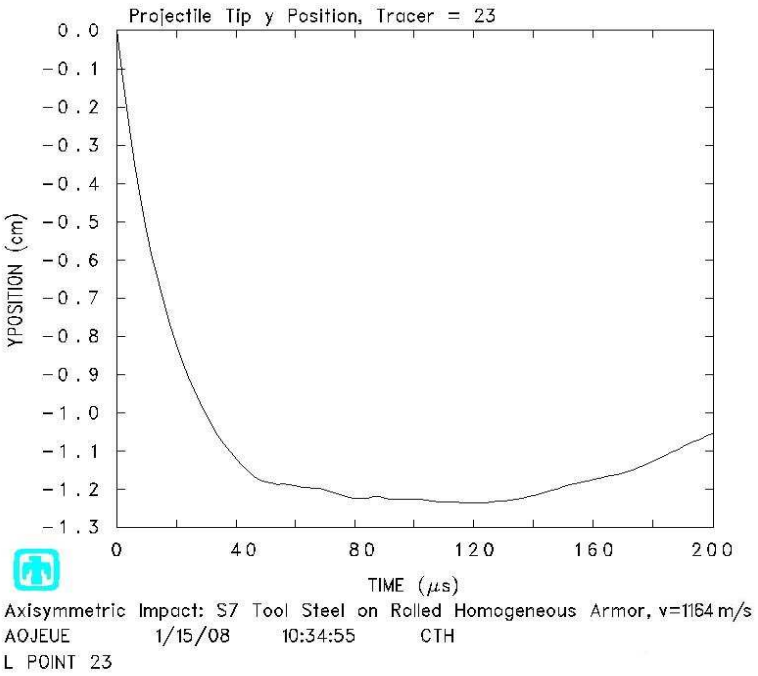

Figure 6.4: Vertical position of projectile tip impacting RHA target with gaps at 1164 m/s using BLINT algorithm with μ=0.2

is treated as a positive pressure, and tension is treated as a negative pressure. All the pressure plots in these simulations, show the pressure in $dyne/cm^2$.

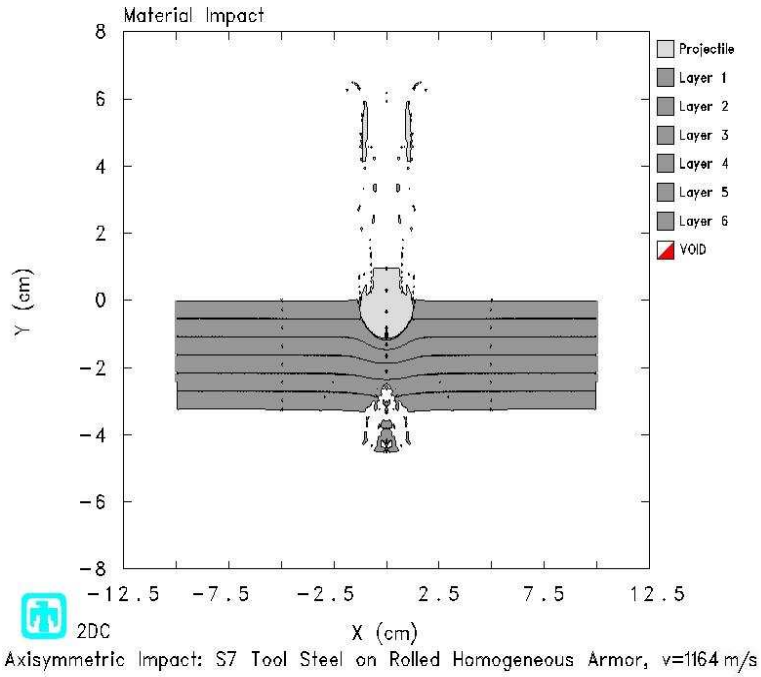

Figure 6.5: S7 tool steel projectile impacting RHA target with gaps at 1164 m/s using CORR option in BLINT algorithm (180 μs)

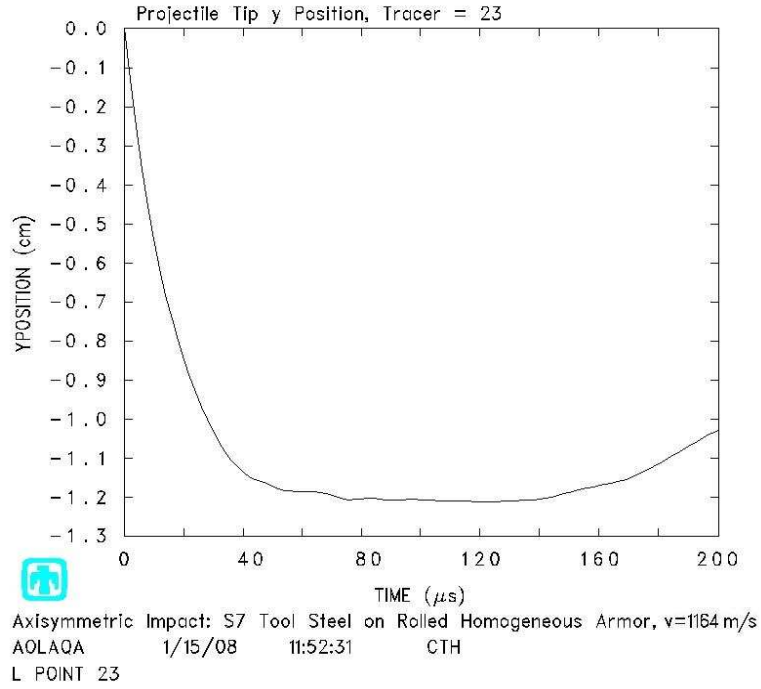

Figure 6.6: Vertical position of projectile tip impacting RHA target with gaps at 1164 m/s using CORR option in BLINT algorithm

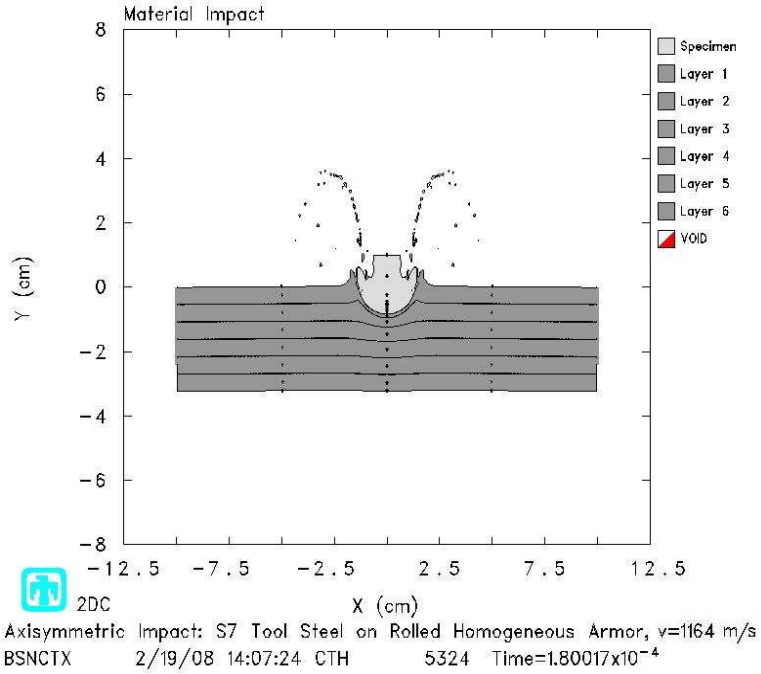

Figure 6.7: S7 tool steel projectile impacting RHA target with gaps at 1164 m/s with MIX=3

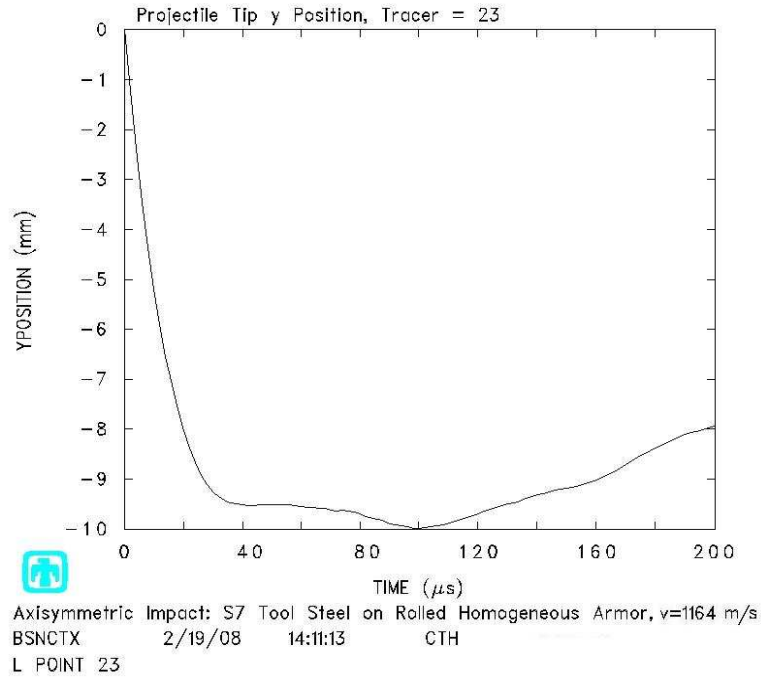

Figure 6.8: Vertical position of projectile tip impacting RHA target with gaps at 1164 m/s with MIX=3

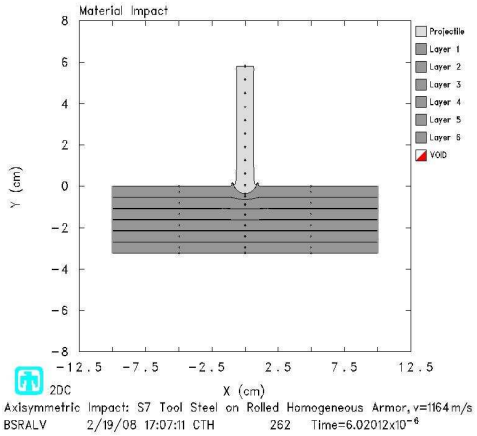

(a) 6 μs

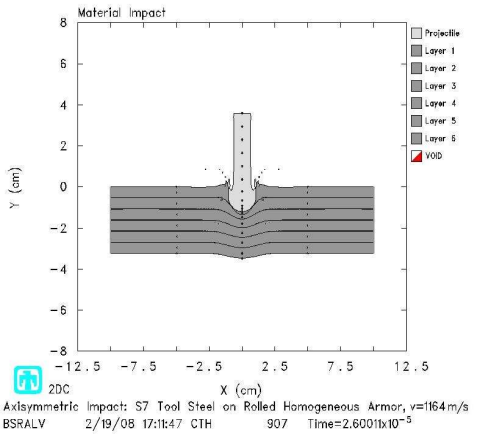

(b) 26 μs

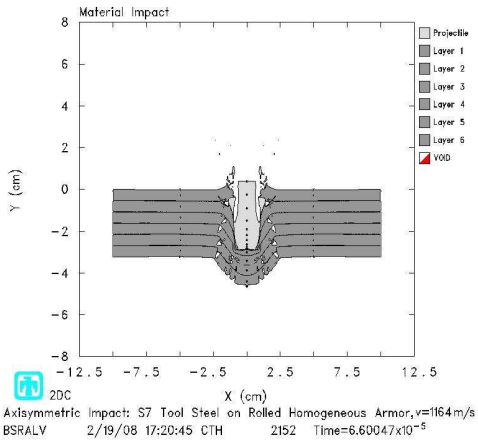

(c) 66 μs

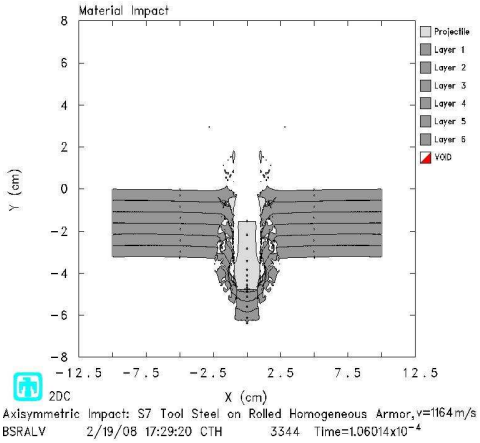

(d) 106 μs

Figure 6.9: Material impact for S7 tool steel projectile and RHA target without using the BLINT algorithm (MIX=5)

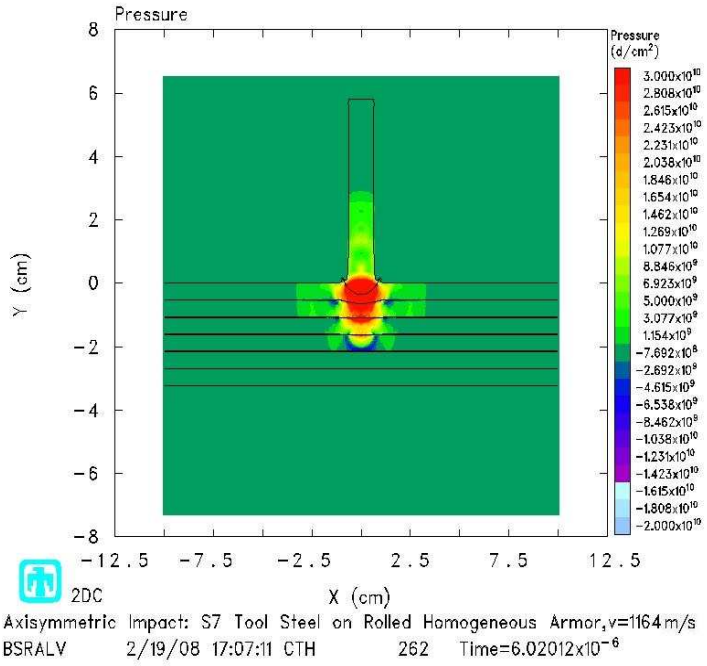

Figure 6.10: Pressure for S7 tool steel projectile impacting RHA target at 1164 m/s without using the BLINT algorithm (6 μs)

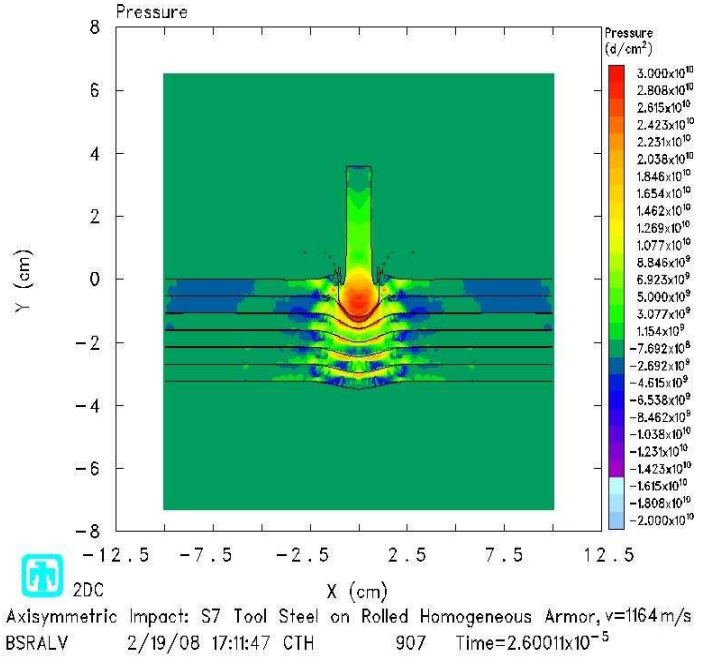

Figure 6.11: Pressure for S7 tool steel projectile impacting RHA target at 1164 m/s without using the BLINT algorithm (26 μs)

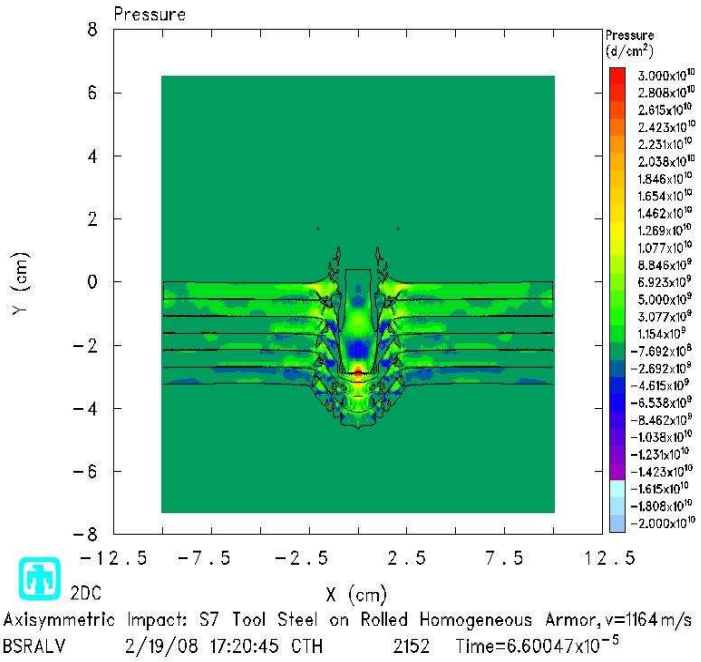

Figure 6.12: Pressure for S7 tool steel projectile impacting RHA target at 1164 m/s without using the BLINT algorithm (66 μs)

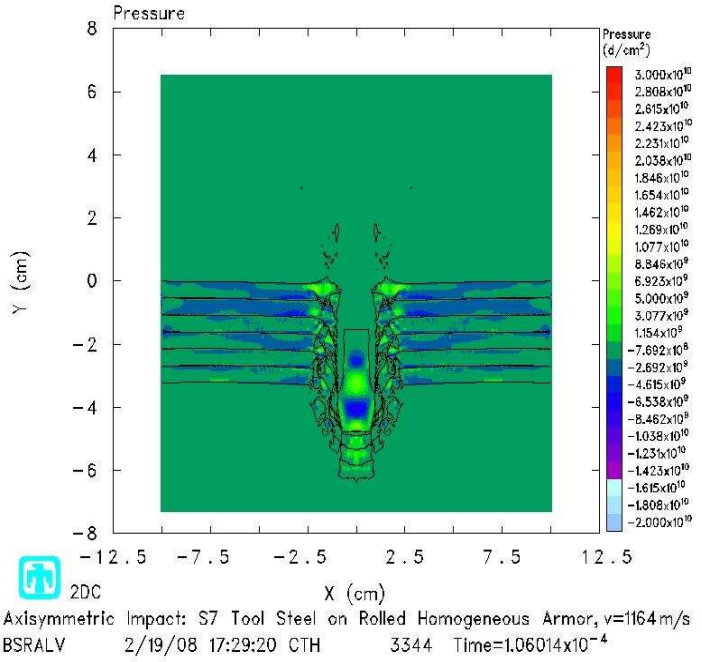

Figure 6.13: Pressure for S7 tool steel projectile impacting RHA target at 1164 m/s without using the BLINT algorithm (106 μs)

Upon perforating the plate, the projectile has a residual velocity of approximately 450 m/s shown in Figure 6.14. There is one issue with this graph that must be discussed. The Lagrangian point for the tip of the projectile was chosen to be at (x,y) = (0,0) which is fine for considering position; however, when looking at velocity, the initial velocity shows up as half of what it actually was in the input file. Since the projectile tip begins initially at the target interface, then the target and the projectile both share the point (0,0). Therefore, the velocity at this point is initially the average of the velocities of the projectile and the target. The target is initially at rest, and the projectile has an impact velocity of 1164 m/s. This results in an initial velocity of 582 m/s, which agrees with what is shown on the graph. After the impact the velocity of the projectile and target at that point are equal so that the rest of the graph is the actual velocity at that point. The way to get around this is to add a tracer point vertically displaced into the projectile just enough that CTH registers the initial velocity of only the projectile. This velocity should be very close to the velocity actually at the tip. This method for obtaining the velocity graphs were used in both the confined ceramic and the ceramic armor simulations.

Zukas and Scheffler provide the normalized residual velocities for one, two, four and six layer targets with the same overall thickness in the form of a graph. In an effort to compare to the ZeuS data, the target model above was modified to account for these other layer variations. From these simulations the residual velocities based on the number of layers was determined. Those values were then normalized and compared to the solutions for the ZeuS code that Zukas and Scheffler came up with. This comparison is shown both in tabular format in Table 6.1 and graphically in Figure 6.15.

There are a few obvious observations that can be made from these results. It can be seen that the normalized residual velocities output from CTH are smaller than those given from the ZeuS code. In fact, in the CTH results, the penetrator does not perforate the targets for the one and two-layer arrangements. However, as expected, layering of the target significantly reduced the strength of the target and therefore

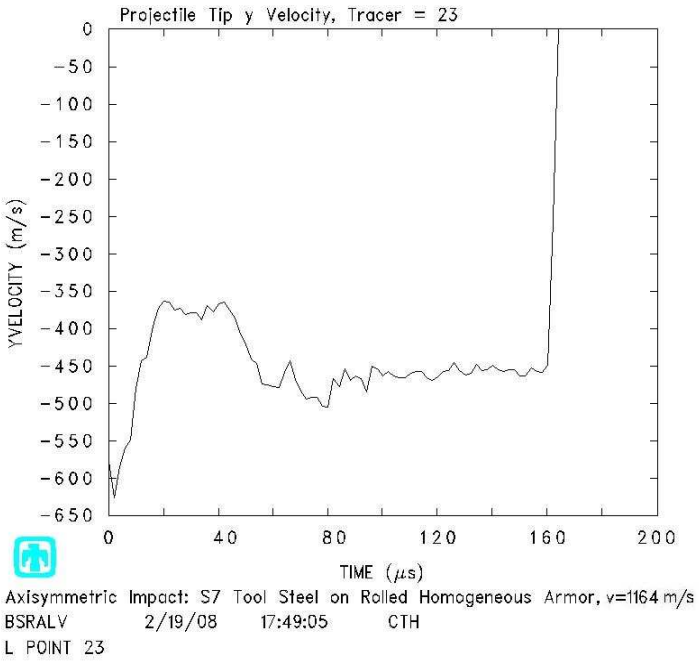

Figure 6.14: Velocity vs Time for the S7 tool steel projectile tip for velocity equal to 1164 m/s (tracer point located at projectile tip

Table 6.1: Dependency of residual and normalized residual velocities on the number of layers (for an impact velocity equal to 1164 m/s)

Number of Layers	Residual Velocity (m/s)	Normalized Residual Velocity (CTH)	Normalized Residual Velocity (ZeuS)
1	0	0.000	0.200
2	0	0.000	0.300
4	250	0.215	0.470
6	475	0.408	0.540

the target's ability to resist the penetration of the projectile which is consistent with the results from Zukas and Scheffler.

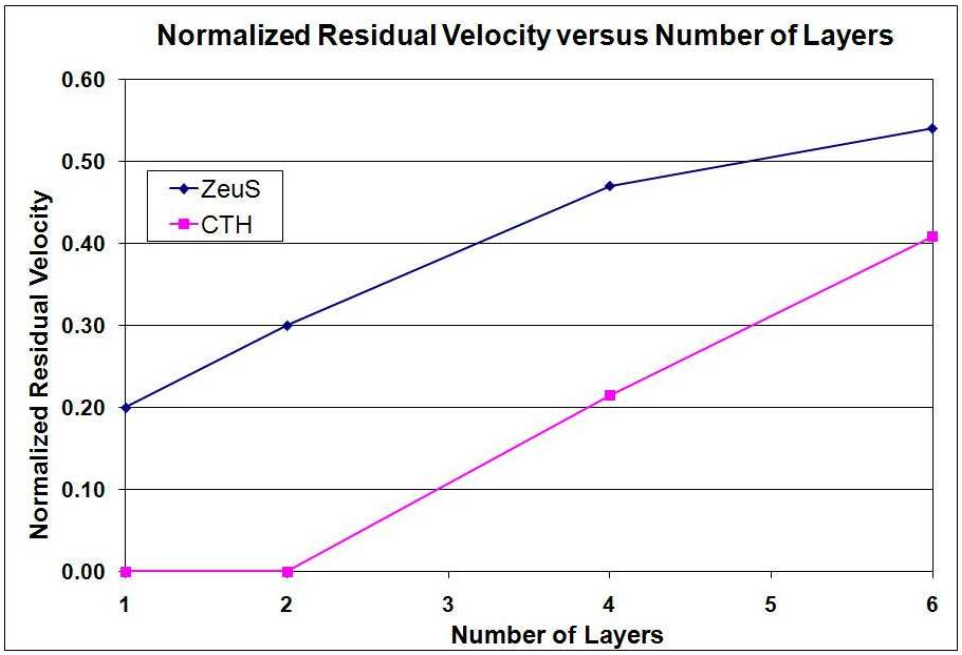

Figure 6.15: Normalized residual velocity versus number of layers for a striking velocity of 1164 m/s

6.1.2 Boundary Conditions. Since all of the simulations in this research are axisymmetric cylindrical models, the boundary condition on the left hand side was modeled as a symmetry condition (Type 0). The right hand boundary condition in all the models was treated as a finite boundary and therefore was modeled using Type 2. The upper and lower boundary conditions were also modeled as finite boundaries (Type 2) that would still allow the target fragments and projectile to exit the mesh.

Even with the boundaries determined for the main simulations, a study of the effect of changing the right side boundary condition was performed. For this study, the Type 0 (symmetry or rigid boundary condition), Type 1 (semi-infinite boundary condition) and the Type 2 (finite boundary condition) were all applied to the right boundary and then compared to one another. The pressure plots are shown for these three boundary conditions in Figures 6.16 through 6.33.

The following realizations about the three CTH boundary conditions were observed from the pressure plots. From Figure 6.18 to Figure 6.19 the pressure wave in the top portion of the target toward the far side boundary changes from compression

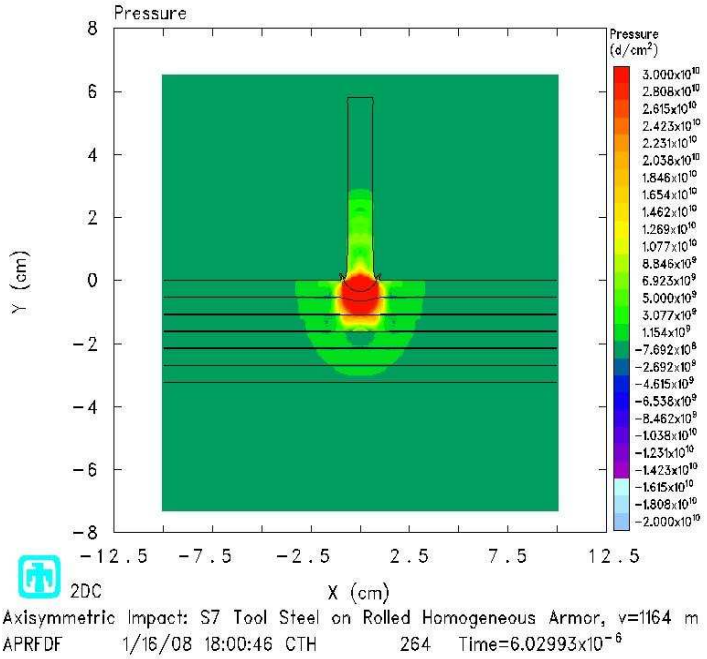

Figure 6.16: Pressure for S7 tool steel projectile impacting RHA target at 1164 m/s with Type 0 boundary condition on right side (6 μs)

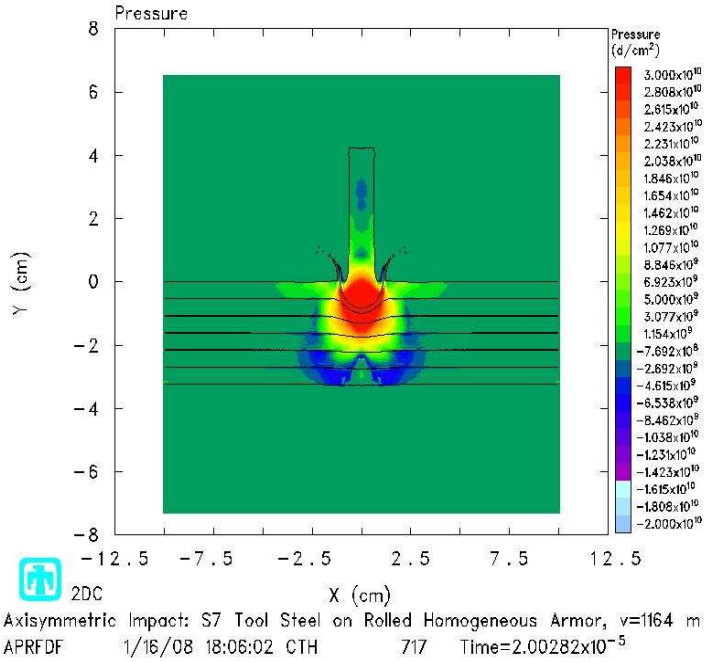

Figure 6.17: Pressure for S7 tool steel projectile impacting RHA target at 1164 m/s with Type 0 boundary condition on right side (20 μs)

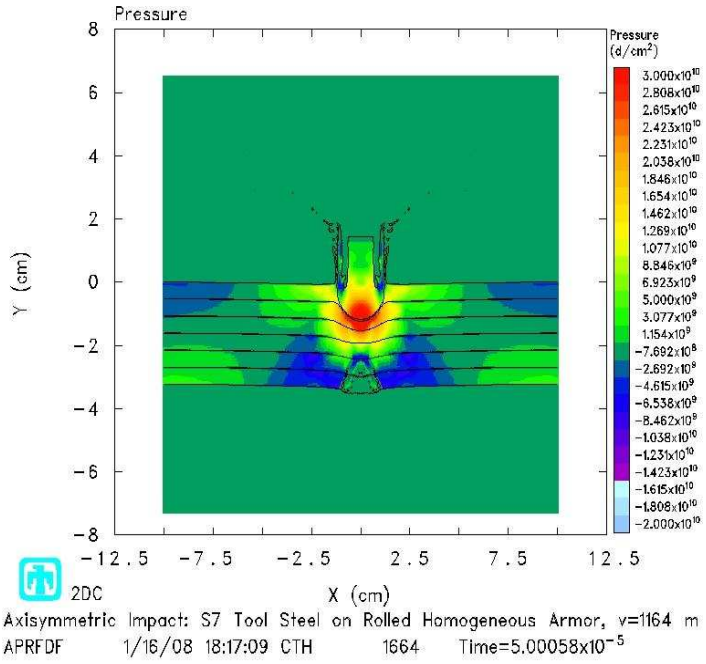

Figure 6.18: Pressure for S7 tool steel projectile impacting RHA target at 1164 m/s with Type 0 boundary condition on right side (50 μs)

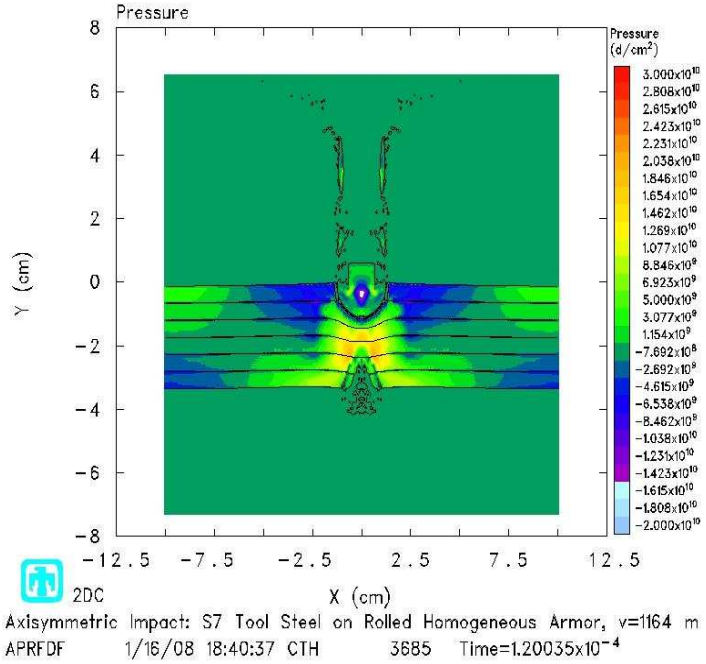

Figure 6.19: Pressure for S7 tool steel projectile impacting RHA target at 1164 m/s with Type 0 boundary condition on right side (120 μs)

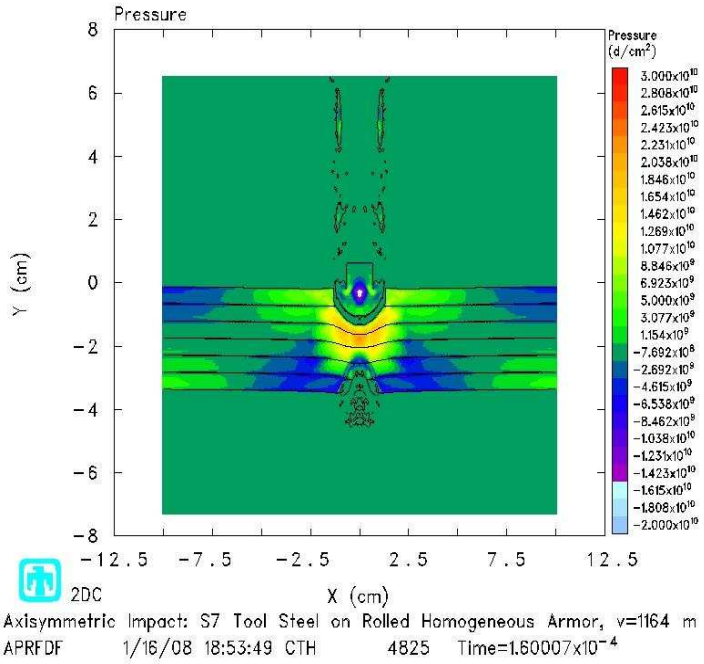

Figure 6.20: Pressure for S7 tool steel projectile impacting RHA target at 1164 m/s with Type 0 boundary condition on right side (160 μs)

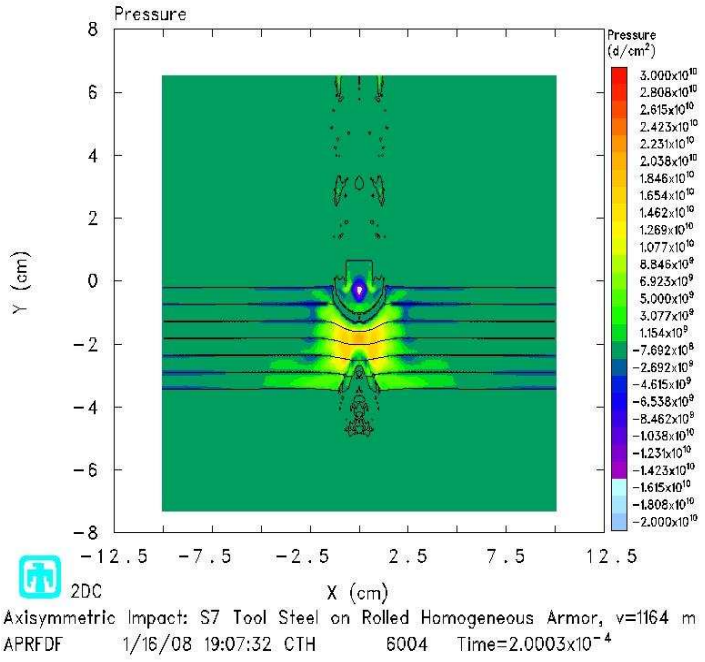

Figure 6.21: Pressure for S7 tool steel projectile impacting RHA target at 1164 m/s with Type 0 boundary condition on right side (200 μs)

to tension and back to compression in Figure 6.20. The opposite is happening on the bottom portion of the target at the side boundaries. There the wave is changing from tension to compression and back to tension. The Type 0 boundary condition is behaving like an absolutely rigid surface (infinite impedance). Upon looking closer at Figure 6.21, it is seen that the top surface of the target is no longer at y=0. This is due to the fact that the Type 0 boundary condition zeros the normal velocity component at the boundary while the tangential velocity component is unaffected.

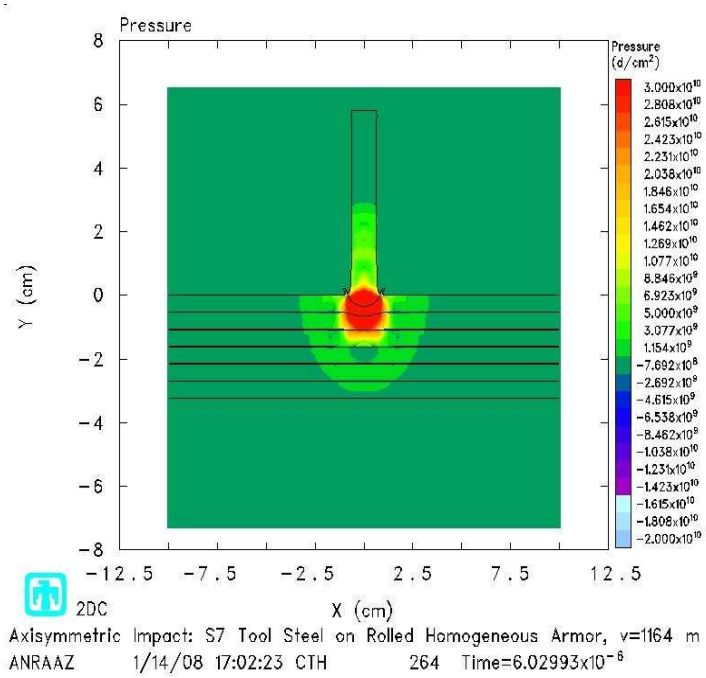

Figure 6.22: Pressure for S7 tool steel projectile impacting RHA target at 1164 m/s with Type 1 boundary condition on right side (6 μs)

It is observed for the Type 1 boundary condition that as the wave propagates out to the right side boundary, it just continues to transmit. There is no reflected wave which confirms that this boundary condition is good for modeling infinite and semi-infinite boundaries.

For the Type 2 boundary condition, it is noticed that as the compression wave in the upper target layers contacts the side boundary it reflects back as a tension wave. As the tension wave in the bottom layers of the target impacts the side boundary,

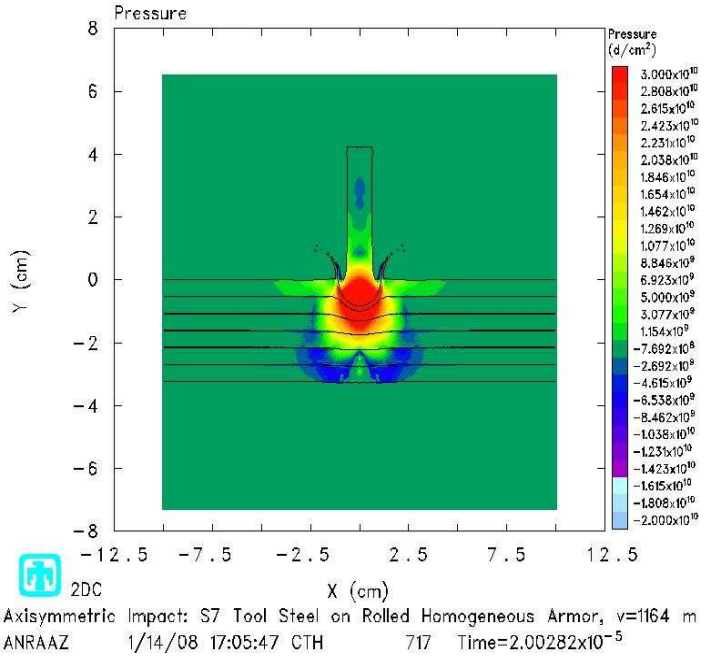

Figure 6.23: Pressure for S7 tool steel projectile impacting RHA target at 1164 m/s with Type 1 boundary condition on right side (20 μs)

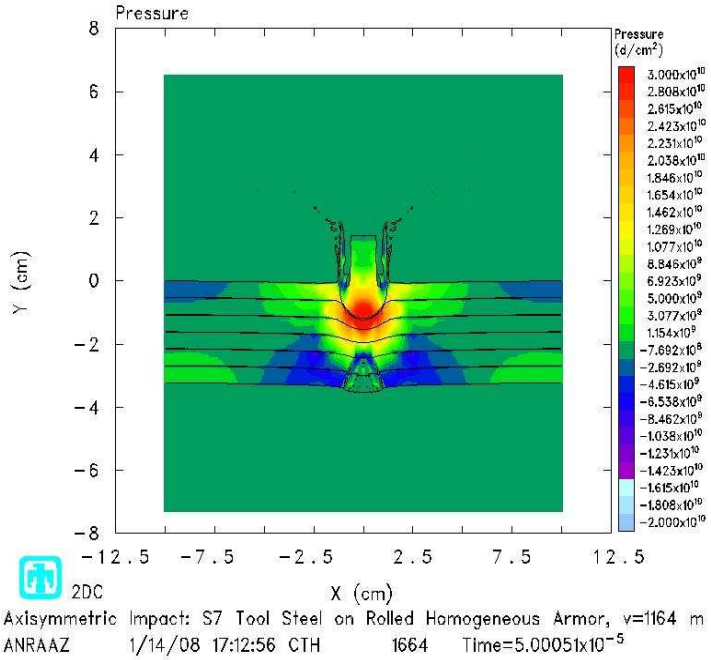

Figure 6.24: Pressure for S7 tool steel projectile impacting RHA target at 1164 m/s with Type 1 boundary condition on right side (50 μs)

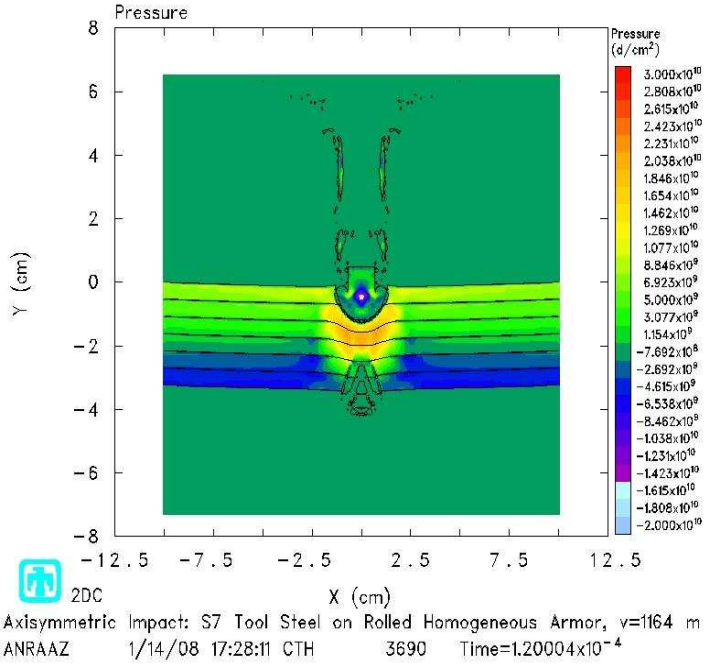

Figure 6.25: Pressure for S7 tool steel projectile impacting RHA target at 1164 m/s with Type 1 boundary condition on right side (120 μs)

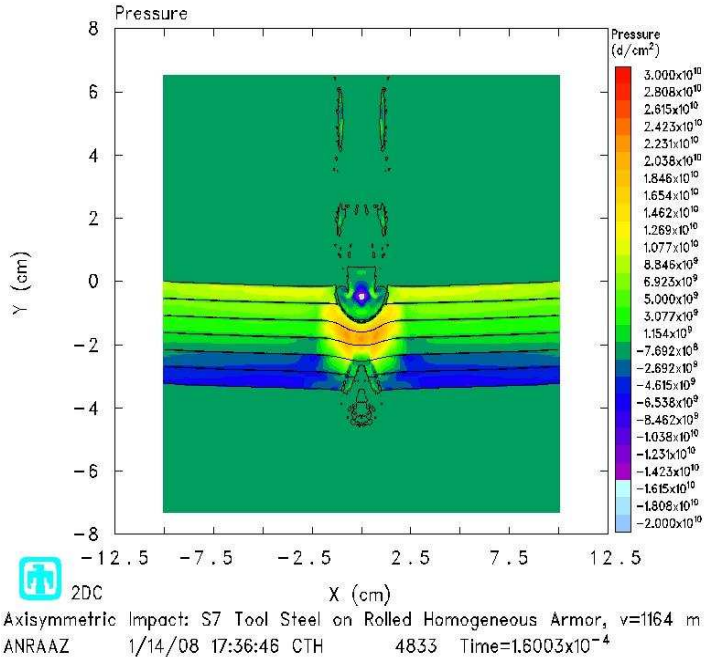

Figure 6.26: Pressure for S7 tool steel projectile impacting RHA target at 1164 m/s with Type 1 boundary condition on right side (160 μs)

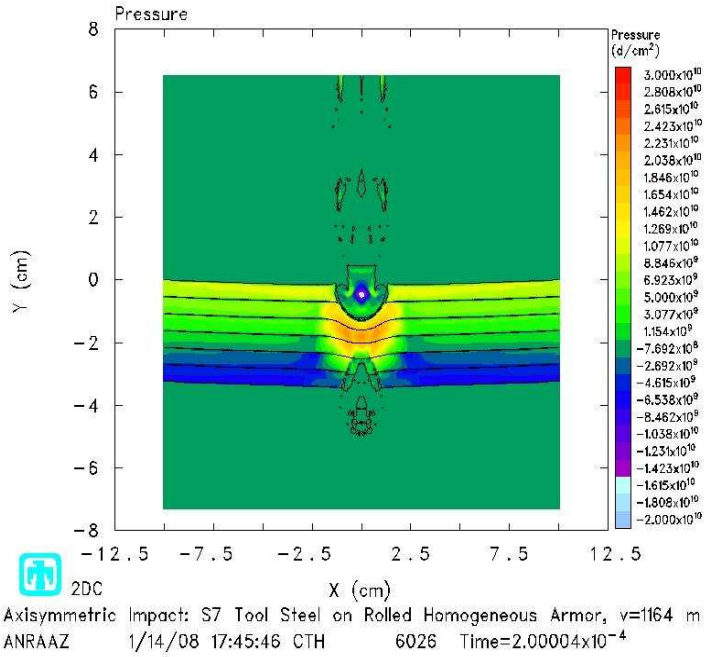

Figure 6.27: Pressure for S7 tool steel projectile impacting RHA target at 1164 m/s with Type 1 boundary condition on right side (200 μs)

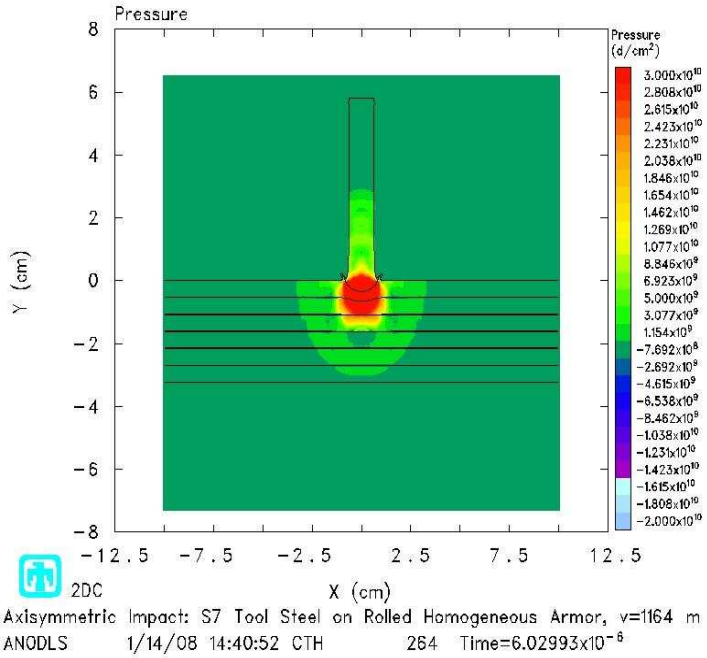

Figure 6.28: Pressure for S7 tool steel projectile impacting RHA target at 1164 m/s with Type 2 boundary condition on right side (6 μs)

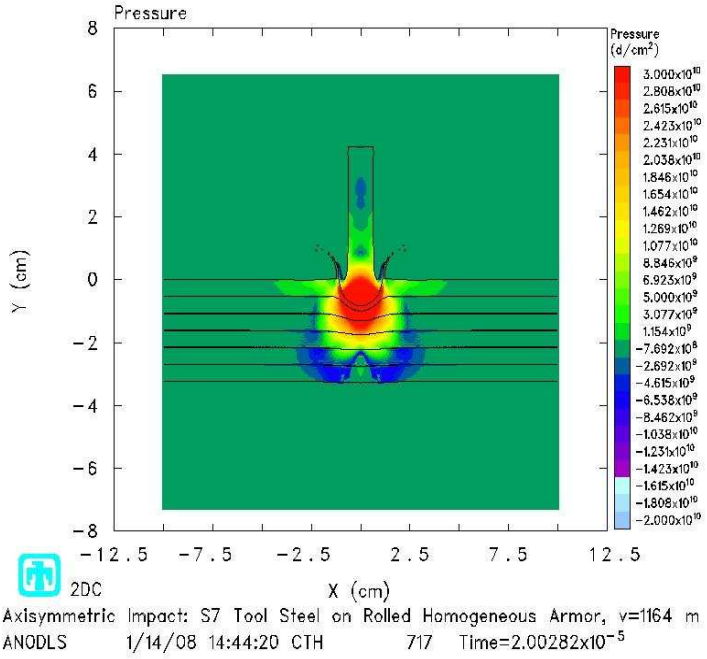

Figure 6.29: Pressure for S7 tool steel projectile impacting RHA target at 1164 m/s with Type 2 boundary condition on right side (20 μs)

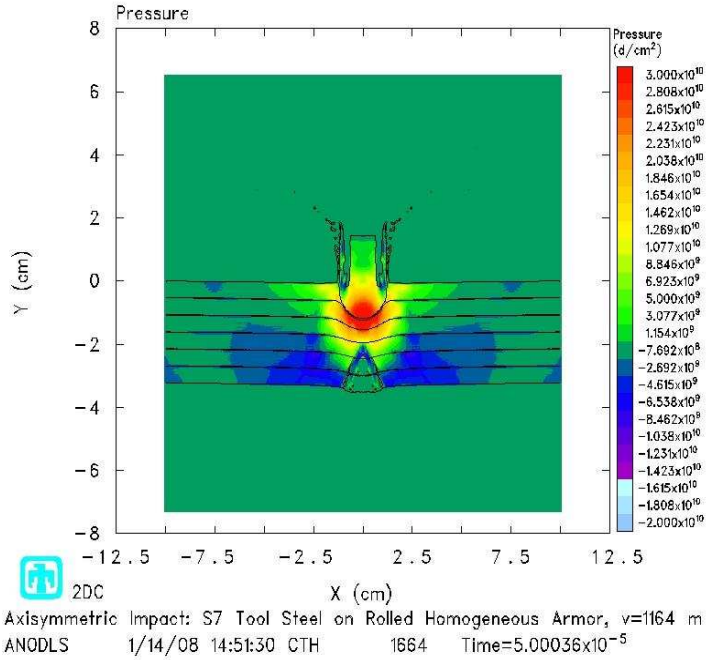

Figure 6.30: Pressure for S7 tool steel projectile impacting RHA target at 1164 m/s with Type 2 boundary condition on right side (50 μs)

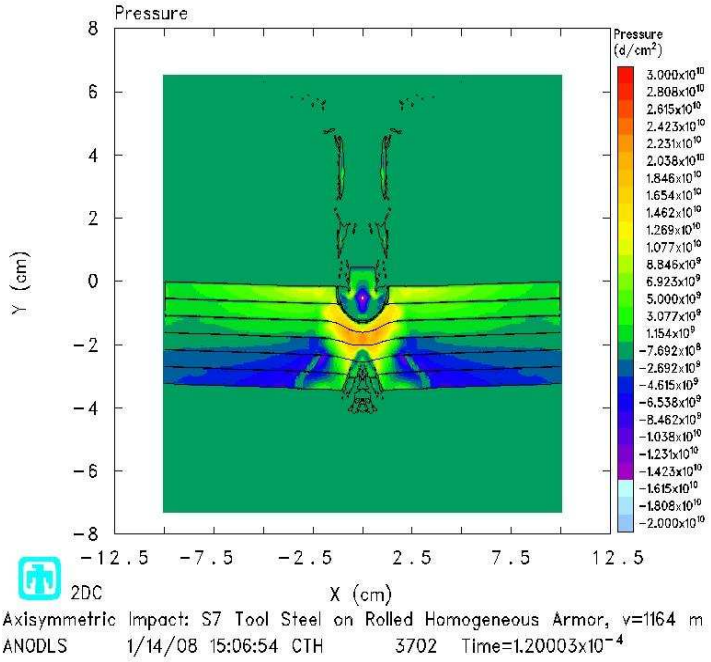

Figure 6.31: Pressure for S7 tool steel projectile impacting RHA target at 1164 m/s with Type 2 boundary condition on right side (120 μs)

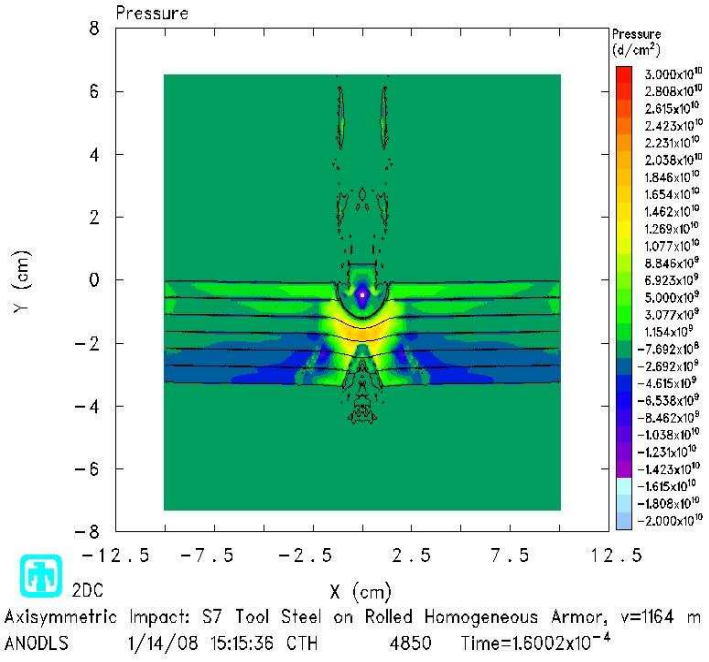

Figure 6.32: Pressure for S7 tool steel projectile impacting RHA target at 1164 m/s with Type 2 boundary condition on right side (160 μs)

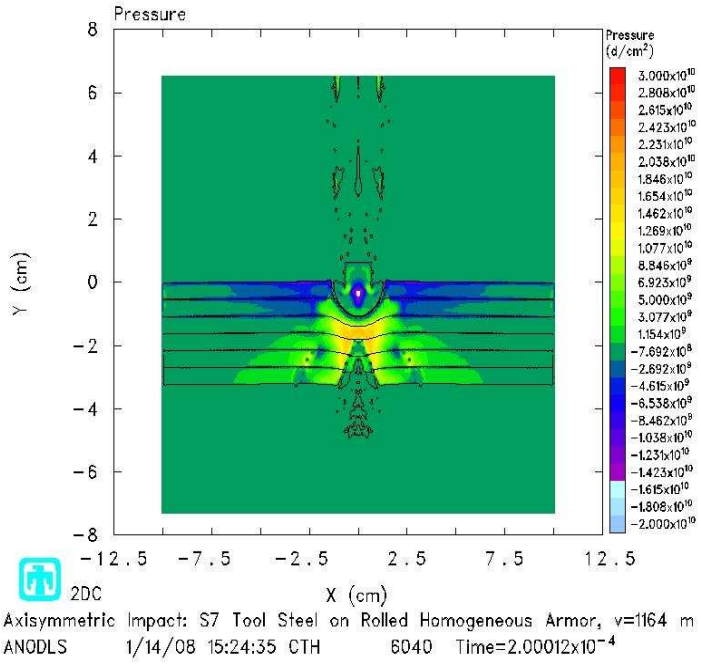

Figure 6.33: Pressure for S7 tool steel projectile impacting RHA target at 1164 m/s with Type 2 boundary condition on right side (200 μs)

it reflects as a compression wave. These wave reflections alternating between tension and compression are indicating that the boundary is being treated as a free edge which is desired to handle cylindrical targets with a finite diameter.

6.1.3 With Gaps versus Without Gaps. As discussed in the previous chapter, most of the time with confined ceramic targets, the ceramic is bonded to the top and bottom metal plugs. Therefore, the multi-layer model was also simulated without the gaps between the layers. Both models were run for speeds of 250 - 1500 m/s. Table 6.2 shows the depth of penetration results for these runs. The depth of penetration was plotted against impact velocity; a polynomial fit was then done to predict the ballistic limit for both targets, refer to Figure 6.34. From the results, it was predicted that the target without the gaps would have a little higher ballistic limit than the other target. It is predicted that v_{BL} for the target without gaps is 1450 m/s and v_{BL} for the target without gaps is approximately 1440 m/s. This means that the target without the gaps should be slightly more resistant to the penetration of the

projectile projectile. Towards the right side of Figure 6.34, the slope of the curve becomes steeper, meaning that for small increases in impact velocities an even larger increase penetration depth results.

Table 6.2: Depth of penetration based on impact velocity for multi-layer target with and without gaps

Impact Velocity	Depth of Penetration (cm)	
(m/s)	With Gaps	Without Gaps
250	0.40	0.37
500	0.53	0.54
750	0.71	0.67
1000	0.93	0.87
1164	1.21	1.11
1250	1.59	1.50
1300	1.88	1.83
1350	2.22	2.11
1400	2.73	2.60
1450	perforates target	perforates target
1500	perforates target	perforates target

The multi-layer plate models were then simulated for velocities between 1400 m/s and 1450 m/s to see what CTH actually would predict for the ballistic limit velocity. These runs resulted in a v_{BL} equal to 1420 m/s for the target without the gaps and 1415 m/s for the target with gaps. The percent error for v_{BL} of the two targets was calculated to be 2.1% for the target without gaps and 1.8% for the target with gaps.

Once the impact velocity reached around 1000 m/s, spallation of the bottom side of the target was created. This was observed in the targets with and without the gaps between the targets. The material impact plots showing this can be seen in Figures 6.35 (a) and (b). The spall for the target with gaps consisted of several fragments where the target without gaps had one larger piece and a few smaller fragments. At higher velocities, it can be seen that as the projectile penetrates deeper in the target it creates a cavity that is cylindrical in shape. This is to be expected for intermediate rods ($L/D \simeq 4$) at high velocities. At velocities near the ballistic limit, it was observed

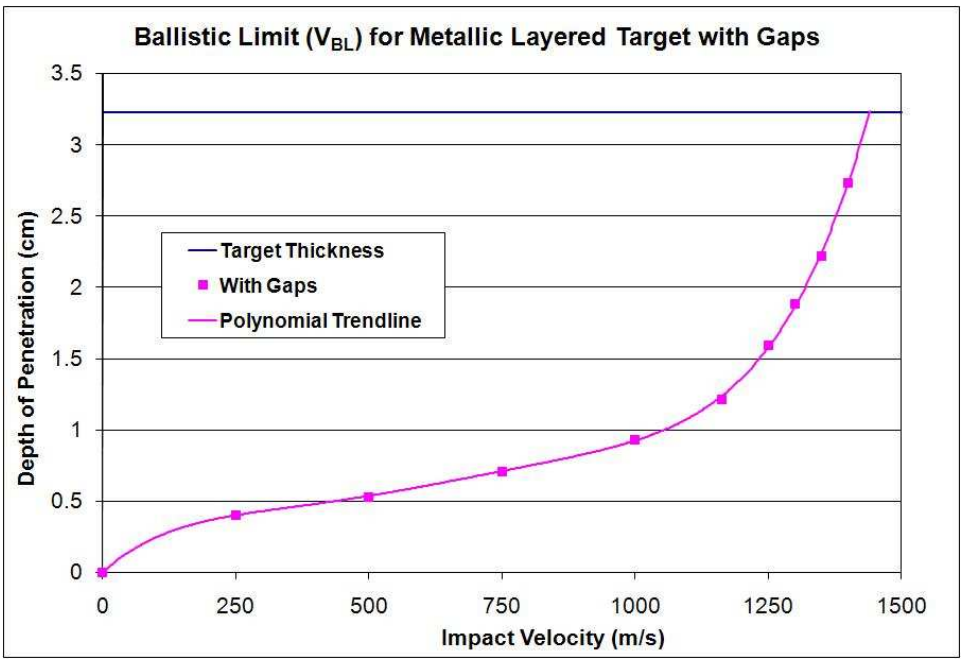

(a) With gaps

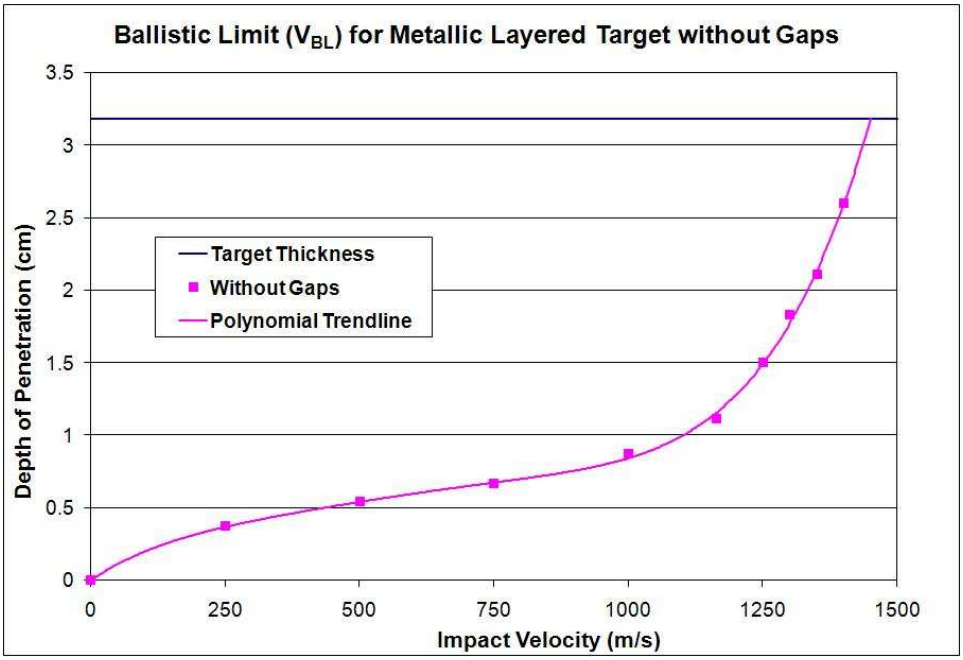

(b) Without gaps

Figure 6.34: Determination of ballistic limit for multi-layer target

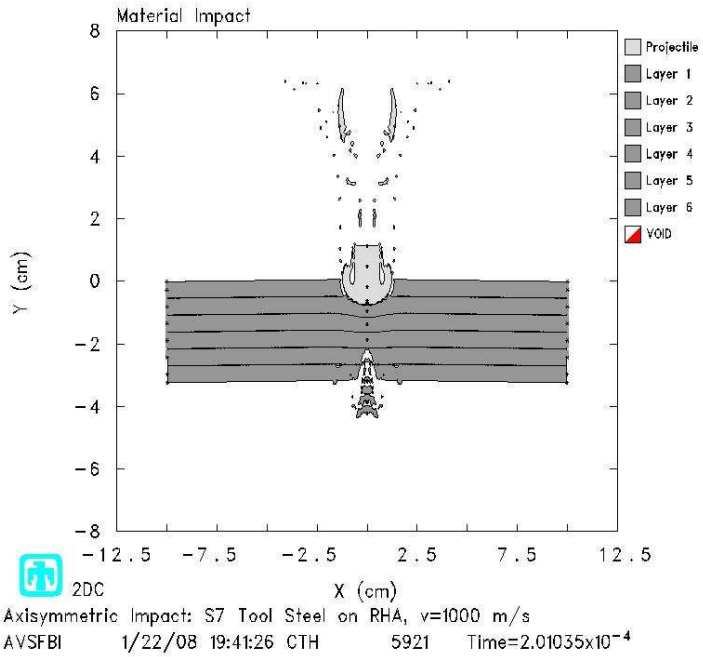

(a) Target with gaps $v_{BL} = 1415$ m/s

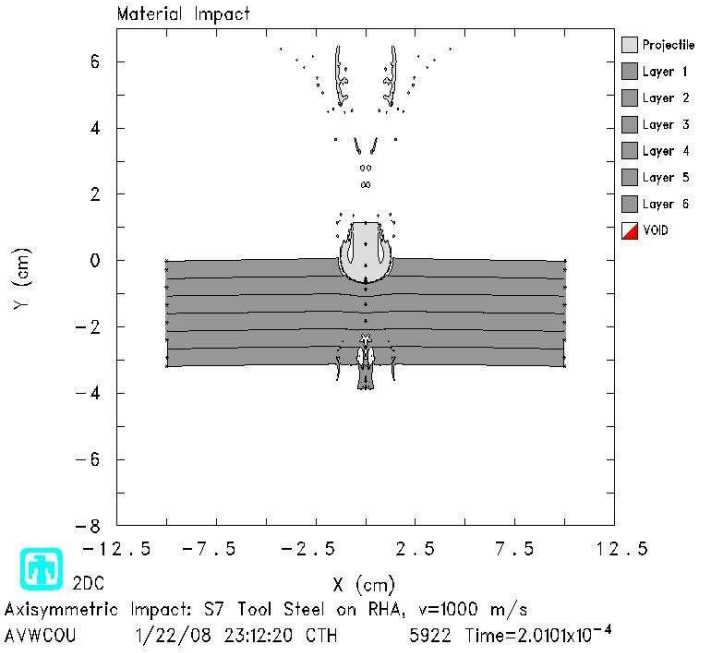

(b) Target without gaps $v_{BL} = 1420$ m/s

Figure 6.35: Spallation of RHA target due to impact of S7 tool steel projectile

that the target exhibited failure due to plugging. The material impact plots for the target both with and without gaps between the layers are shown for its ballistic limit velocity in Figures 6.36 and 6.37 (a)–(d). These figures show the progression of the projectiles as they penetrate into the targets and ultimately perforate the targets shearing out a chunk of material as it goes. From these figures it does not appear that the gaps drastically affect the way the targets fail for impact velocities near the ballistic limit.

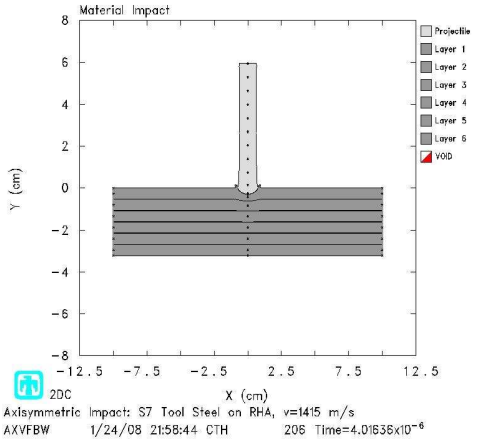

(a) 4 μs

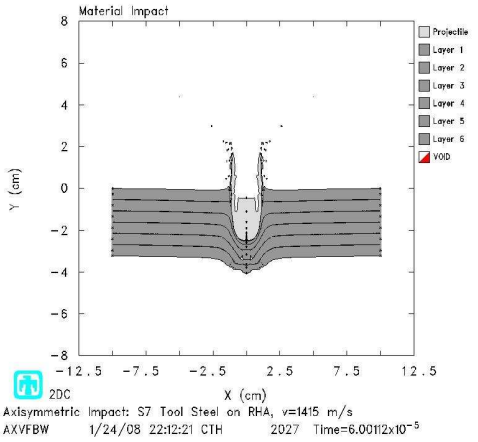

(b) 60 μs

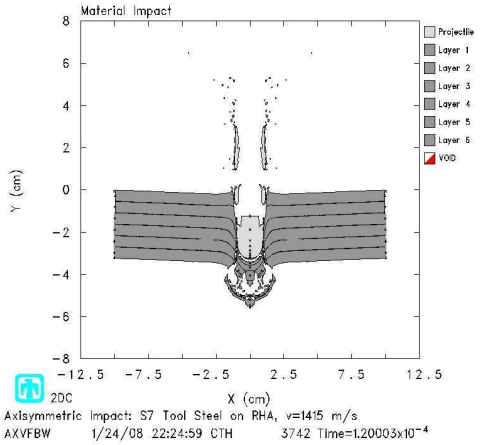

(c) 120 μs

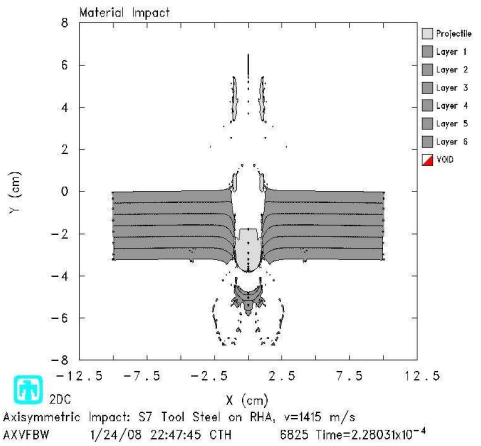

(d) 228 μs

Figure 6.36: Material impact for S7 tool steel projectile and RHA target at 1415 m/s with gaps between layers

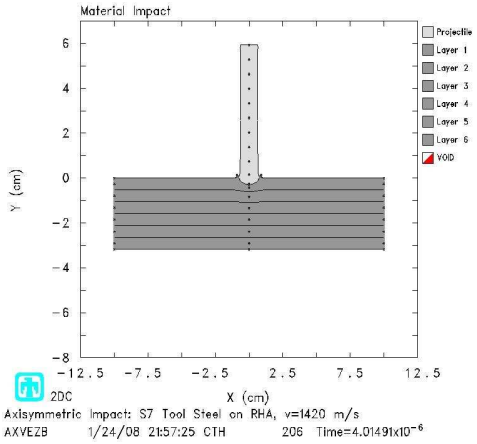

(a) 4 μs

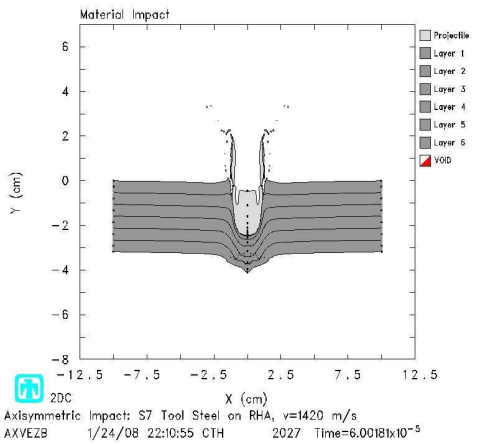

(b) 60 μs

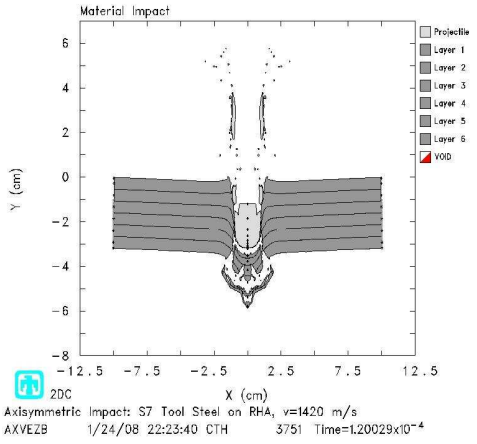

(c) 120 μs

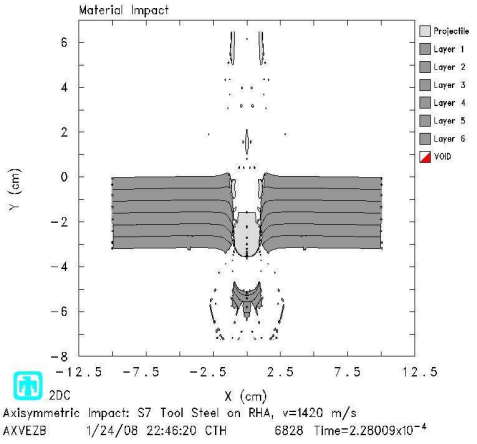

(d) 228 μs

Figure 6.37: Material impact for S7 tool steel projectile and RHA target at 1420 m/s without gaps between layers

The respective pressure plots are also shown for these two cases in Figures 6.38–6.45. Comparing Figure 6.38 and Figure 6.42 the initial compression wave can be seen transmitting through the first four layers in both cases. The compression wave in the for the target without gaps smoothly transmits through the plates; however, the compression wave in the target with gaps is not being transmitted as smoothly due to the plates being able to slide and separate. From there the wave progresses very similarly in both plates with only minor differences in the pressure waves. When

comparing Figures 6.40 and 6.41, it also clear that between these time steps the pressure waves have reached the free edge of the target and reflected. The compression wave in the upper half of the target reflects back as a tension wave, and the tension wave in the lower portion of the target reflects as a compression wave. This confirms that the side boundaries are indeed being treated as free edges. This can also be observed between Figure 6.44 and 6.45 for the target without gaps.

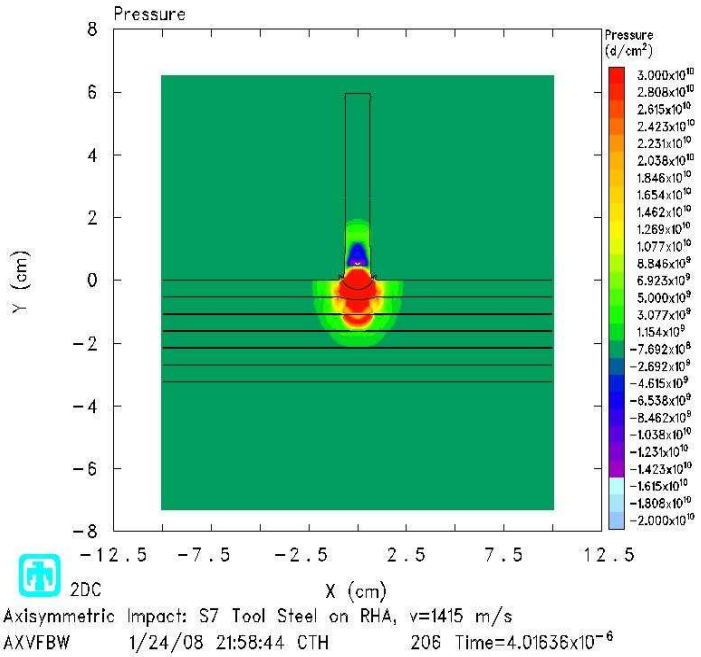

Figure 6.38: Pressure for S7 tool steel projectile impacting RHA target at 1415 m/s with gaps between layers (4 μs)

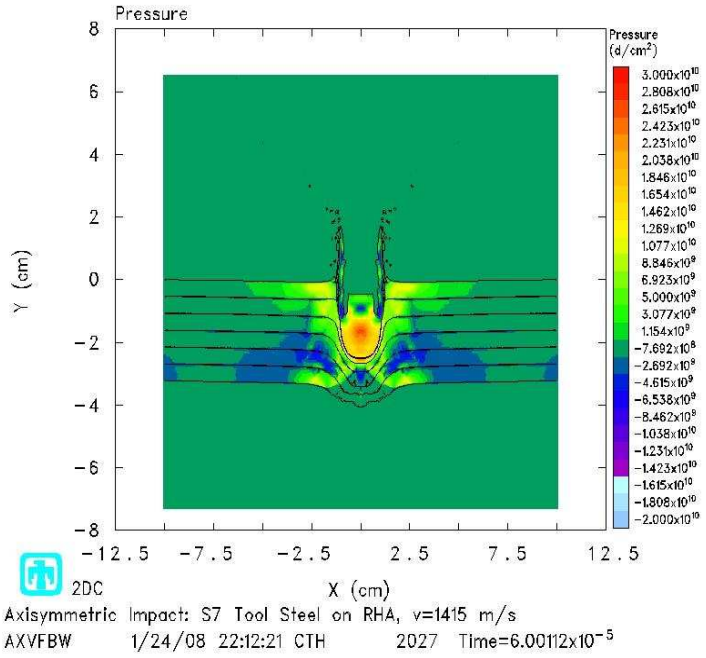

Figure 6.39: Pressure for S7 tool steel projectile impacting RHA target at 1415 m/s with gaps between layers (60 μs)

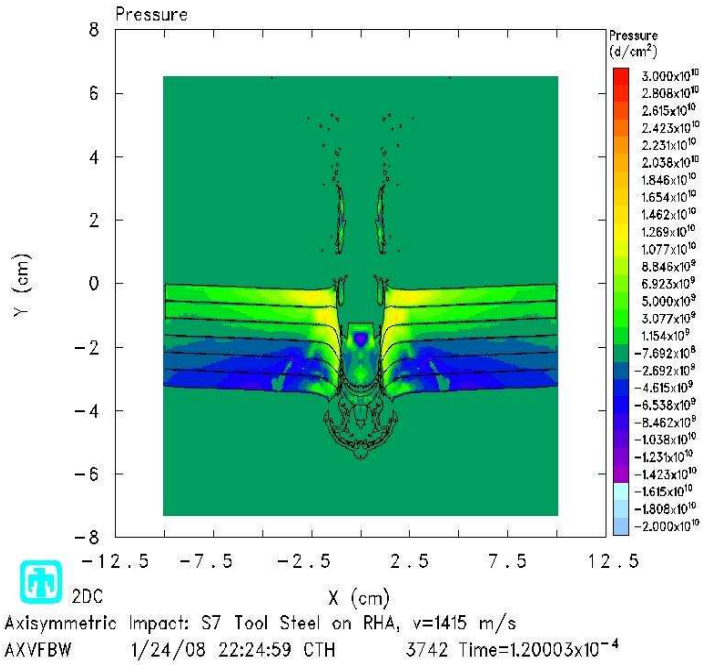

Figure 6.40: Pressure for S7 tool steel projectile impacting RHA target at 1415 m/s with gaps between layers (120 μs)

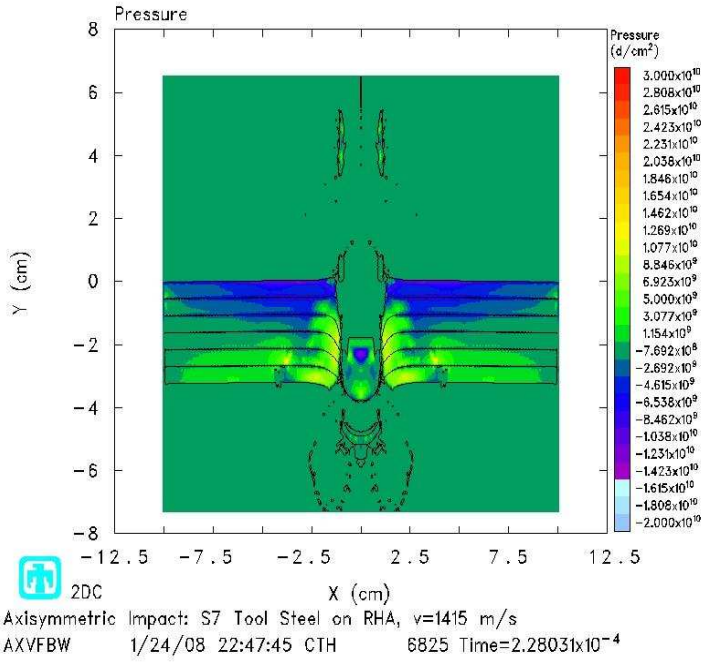

Figure 6.41: Pressure for S7 tool steel projectile impacting RHA target at 1415 m/s with gaps between layers (228 μs)

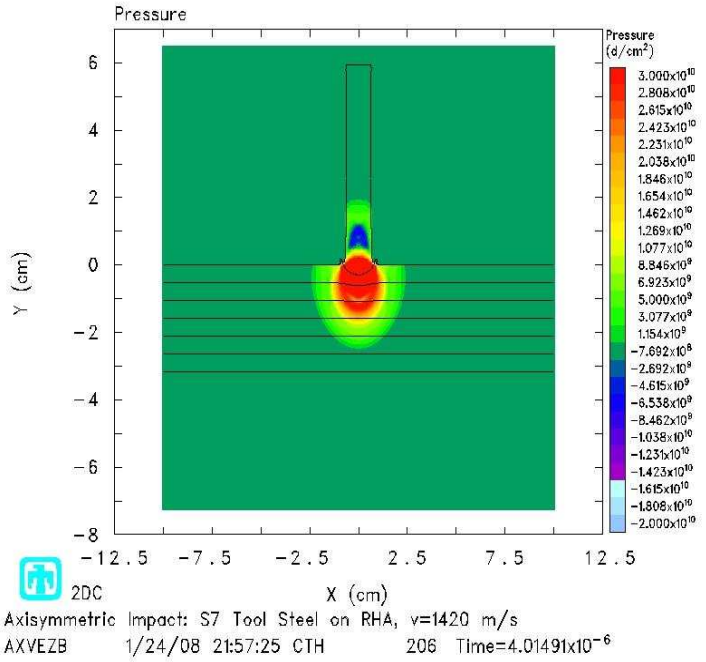

Figure 6.42: Pressure for S7 tool steel projectile impacting RHA target at 1420 m/s without gaps between layers (4 μs)

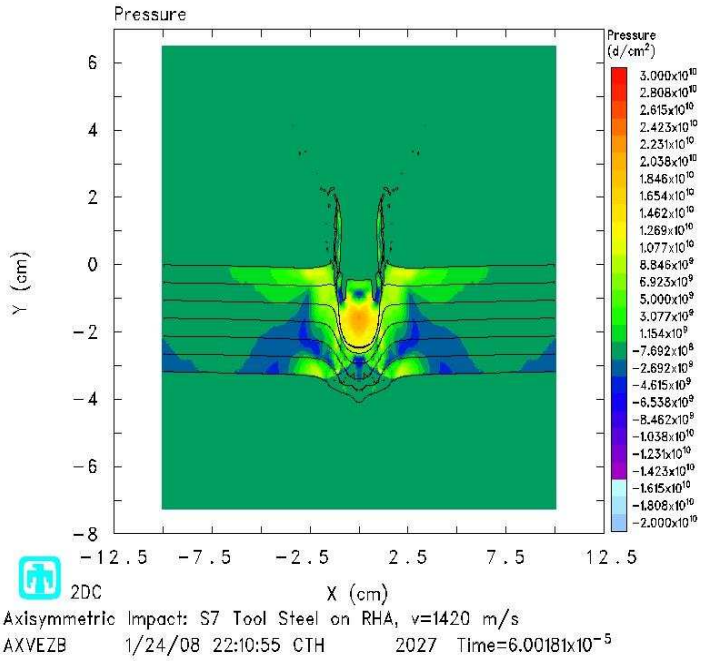

Figure 6.43: Pressure for S7 tool steel projectile impacting RHA target at 1420 m/s without gaps between layers (60 μs)

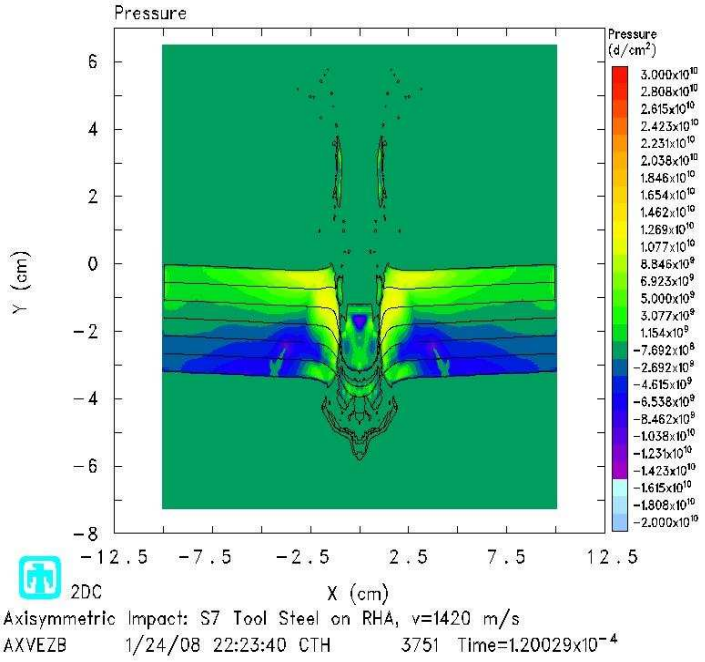

Figure 6.44: Pressure for S7 tool steel projectile impacting RHA target at 1420 m/s without gaps between layers (120 μs)

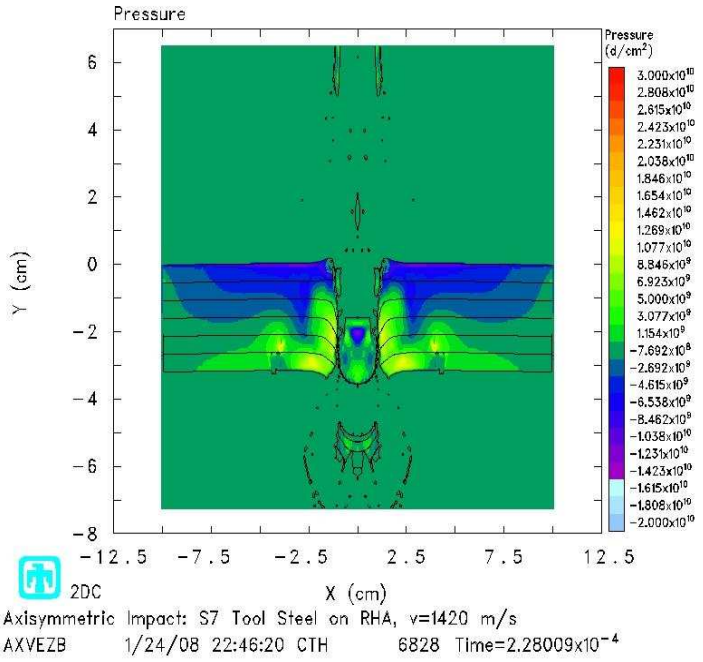

Figure 6.45: Pressure for S7 tool steel projectile impacting RHA target at 1420 m/s without gaps between layers (228 μs)

During discussions with SNL [9], it was mentioned that the pressure history should be looked at to determine what values of pressure the projectile and target were encountering. By first observing the contour pressure plots above, it was determined that ths highest pressures experienced were, as expected, at the projectile tip and the upper target layers. Then by looking at the time history plot of the pressure at the tip of the projectile and the upper layers it was seen that he highest pressure were experienced at initial contact. The point of initial contact, (x,y) = (0,0), is shown for target with and without gaps in Figures 6.46 and 6.47. From these figures, it is seen that immediately upon impact the pressure jumps up to over 15 GPa. Iron experiences an alpha–epsilon phase transition at 13 GPa under shock loading in which the density increases from 7.85 g/cm^3 to 8.219 g/cm^3. The Sesame tabular EOS does not treat this phenomenon; however, the PTRAN EOS discussed earlier does contain a model for iron that can handle this phase change. Therefore, the targets with and without gaps were run again to determine the effect of using the PTRAN model on the ballistic limit of the target. The ballistic limit for the targets

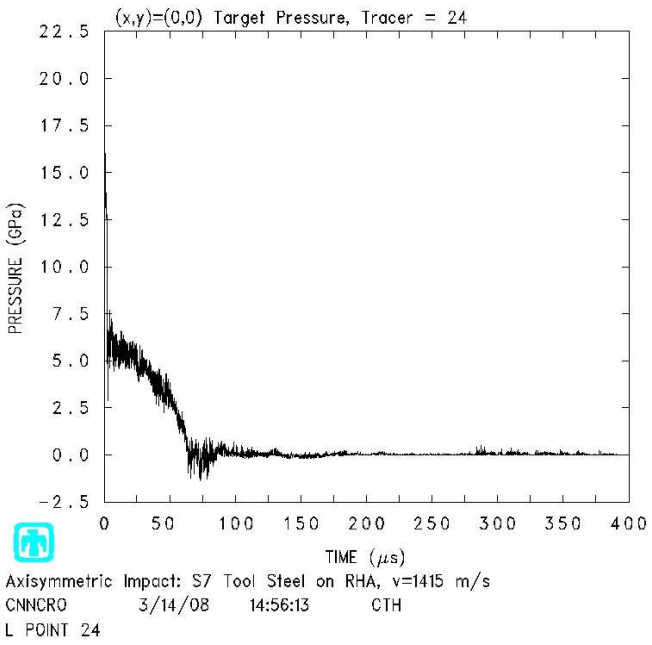

Figure 6.46: Pressure history for S7 tool steel projectile impacting RHA target at 1415 m/s without gaps between layers

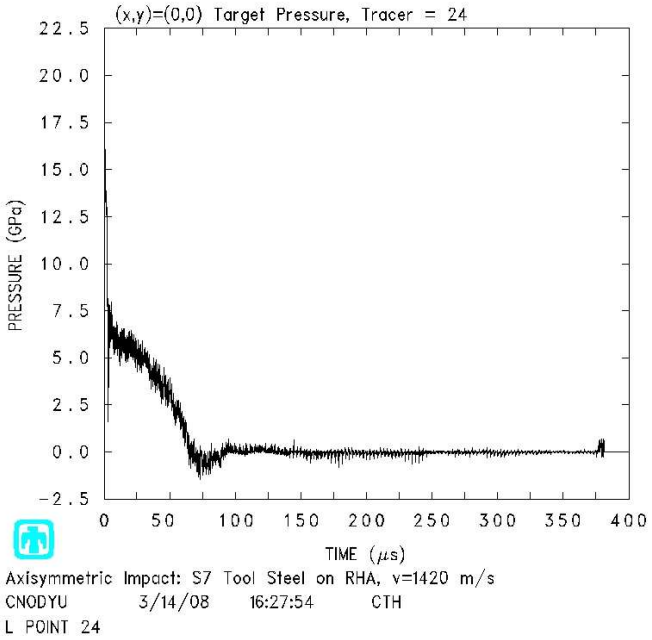

Figure 6.47: Pressure history for S7 tool steel projectile impacting RHA target at 1420 m/s without gaps between layers

with and without gaps was determined to be approximately 1380 m/s and 1385 m/s, respectively. At initial impact, the sharp jump in pressure is occurring mainly in the tip of the projectile and in the first target layer; therefore, those are the main areas that are transitioning to the epsilon phase of iron which has a higher strength than the alpha phase of iron. In effect, the projectile tip and the upper surface of the target are now stronger. Once the projectile penetrates through this upper region of the target, it should penetrate through the remaining portion of the target more easily (i.e. at a lower impact velocity) than if it had not experience this phase change. This could also help to explain why the results for the normalized residual velocity from Zukas and Scheffler did not match as well.

6.2 Confined Ceramic Example

The confined ceramic from Westerling, et al was run for impact velocities equal to 1454, 1581, 1787, 2500 and 2555 m/s. Obviously most of these velocities are greater than the recommended limit for using BLINT; therefore, the BLINT algorithm was only considered for the run with an impact velocity of 1454 m/s. The results actually came out a little better without using the boundary layer interface so it was not used for this problem. The pressures reached immediately upon impact were approximately 20–25 GPa and even larger for the highest impact velocity cases. Since the tungsten projectile is initially impacting the steel case that surrounds the B_4C ceramic, the steel case was modeled using the PTRAN EOS for iron to account for any alpha–epsilon phase change that takes place.

These simulations were modeled using MIX=5 as if it were frictionless, as well as MIX=3. A comparison of the DOP results for the experimental data, the AUTODYN-2D Lagrangian code and CTH at different times is provided for each velocity in Table 6.3. From the data, it is seen that both MIX options match fairly well, but in general, the MIX=3 option matches both the experimental and AUTODYN-2D simulation results better. The CTH results, in general, match the experimental and AUTODYN-2D simulation depths better as the time for each impact event progresses.

The accuracy of these results was also improved for the runs that were performed at higher impact velocities. Overall, the cases where the MIX option equaled three and the impact velocity was 1581 m/s and 1787 m/s agreed the best with the experimental and the AUTODYN-2D results. These penetration depths for both MIX options were

Table 6.3: Depth of penetration at certain time intervals based on impact velocity (*value was not available)

Impact Velocity (m/s)	Time (s)	Depth of Penetration (m)			
		Experiment [49]	AUTODYN-2D [49]	CTH	
				MIX=5	MIX=3
1454	0.00001	0.0010	0.0030	0.0064	0.0061
	0.00002	0.0030	0.0090	0.0123	0.0109
	0.00003	0.0060	0.0130	0.0179	0.0154
	0.00004	0.0100	0.0180	0.0229	0.0193
1581	0.00001	0.0030	0.0040	0.0075	0.0068
	0.00002	0.0110	0.0110	0.0145	0.0129
	0.00003	0.0190	0.0180	0.0207	0.0188
	0.00004	0.0260	0.0240	0.0272	0.0247
1787	0.00001	0.0040	0.0050	0.0092	0.0084
	0.00002	0.0130	0.0140	0.0176	0.0163
	0.00003	0.0230	0.2100	0.0263	0.0241
	0.00004	0.0310	0.0290	0.0339	0.0320
2500	0.00001	0.0120	0.0120	0.0137	0.0146
	0.00002	0.0250	0.0250	0.0294	0.0283
	0.00003	N/A*	N/A*	0.0437	0.0430
2555	0.00001	0.0120	0.0120	0.0151	0.0148
	0.00002	0.0250	0.0250	0.0300	0.0289
	0.00003	N/A*	N/A*	0.0451	0.0441

then plotted against time for each impact velocity. Linear curve fits were applied for each set of data where the slope of these curves are the approximate penetration velocity. Figures 6.48 and 6.49 show the linear curve fits of the depth of penetration versus the time. The results of the penetration velocities for the experimental data, the AUTODYN-2D code and CTH are compared in Table 6.4. The overall trend seems to be one where the MIX=3 option more closely matches the data from the AUTODYN-2D code, while the MIX=5 option tends to align better with the experimental data. The exception to this is for the last case where the velocity equals 2555 m/s. At this

high velocity the MIX=3 option is a better match than the other option for both the experimental and the AUTODYN-2D data. Also in the case where the velocity is 1454 m/s, both MIX options match fairly closely with the AUTODYN-2D code with the MIX=3 option matching closer. However, neither quite agree with the experimental data which has a bilinear curve with a slope of 270 up until 36 μs where the slope then steepens to 710 m/s. CTH did not display this bilinear behavior with either MIX option. If the overall slope of the experimental curve is taken into consideration, then the CTH results seem to be somewhat consistent with the experimentation. The CTH result that is most in agreement with experimental data was the case where the MIX=3 option was used and the impact velocity of the projectile is 2555 m/s, while the best match to the AUTODYN-2D code was the case where the MIX option was set to three and the projectile impacted at a velocity of 2500 m/s. The results for both MIX options improved as the impact velocity increased.

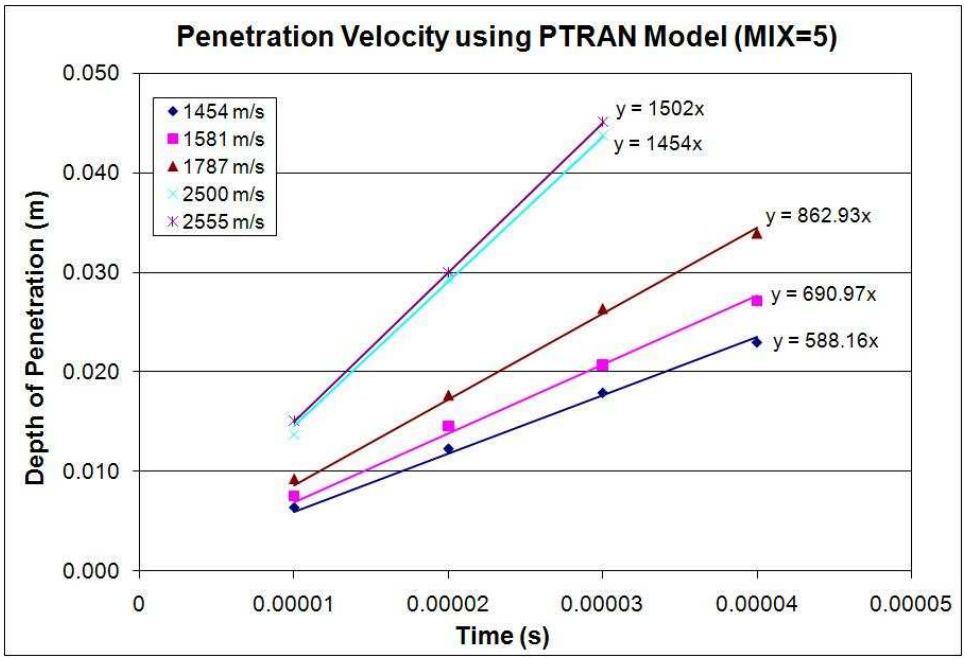

Figure 6.48: Penetration velocity for a confined ceramic based on depth of penetration versus time using MIX=5

The experimental DOP results from Westerling, et al were recorded using X-ray flashes. X-ray pictures of the penetration process are shown in Figure 6.50 for the

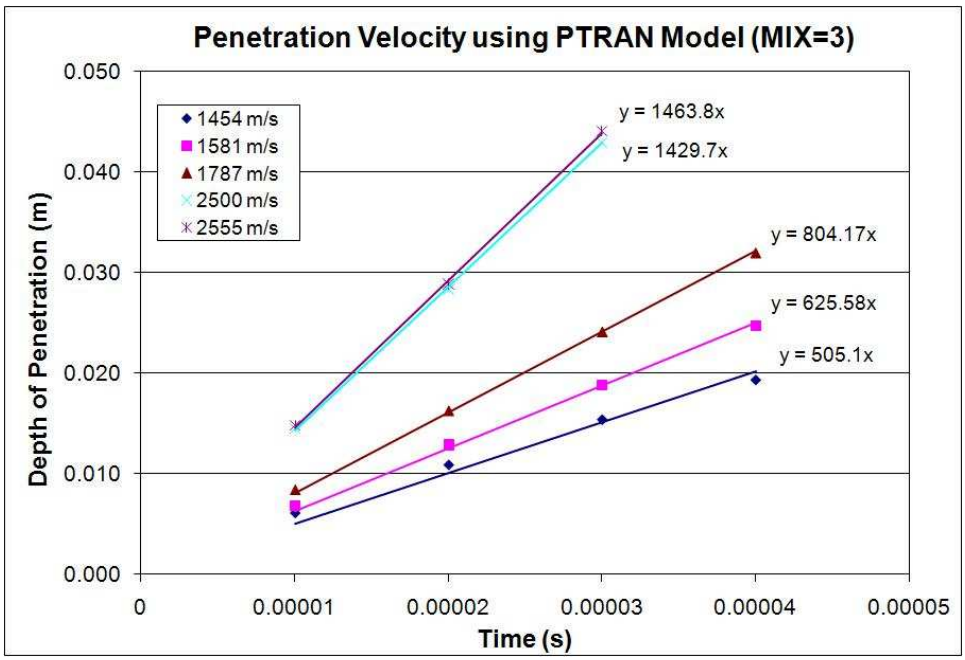

Figure 6.49: Penetration velocity for a confined ceramic based on depth of penetration versus time using MIX=3

Table 6.4: Comparison of penetration velocity from experimentation and simulation of a confined ceramic (*710 m/s, t 36μs)

Impact Velocity (m/s)	Penetration Velocity (m/s)			
	Experiment [49]	AUTODYN-2D [49]	CTH	
			MIX=5	MIX=3
1454	270*	480	588	505
1581	770	615	691	626
1787	920	795	863	804
2500	1485	1440	1454	1430
2555	1450	1480	1502	1464

experimental case where the projectile strikes the target at a velocity of 1581 m/s [49]. The CTH simulation of the material impact is shown in Figures 6.51 through Figures 6.55. The CTH simulation is for the MIX=5 option since this simulation matched the experimental results better. In the CTH simulation figures, pieces of the projectile appear to be breaking off as it penetrates deeper into the ceramic. This process is reducing the mass of the projectile and in turn its kinetic energy. Effectively, the

ceramic is dissipating the kinetic energy of the projectile as both the ceramic target and the tungsten projectile are sustaining damage. This same phenomenon can be seen in the experimental results shown in Figure 6.50. From Figures 6.51–6.55, it can also be seen that the impact of the projectile creates a crater in the B_4C that is approximately twice the diameter of the tungsten projectile.

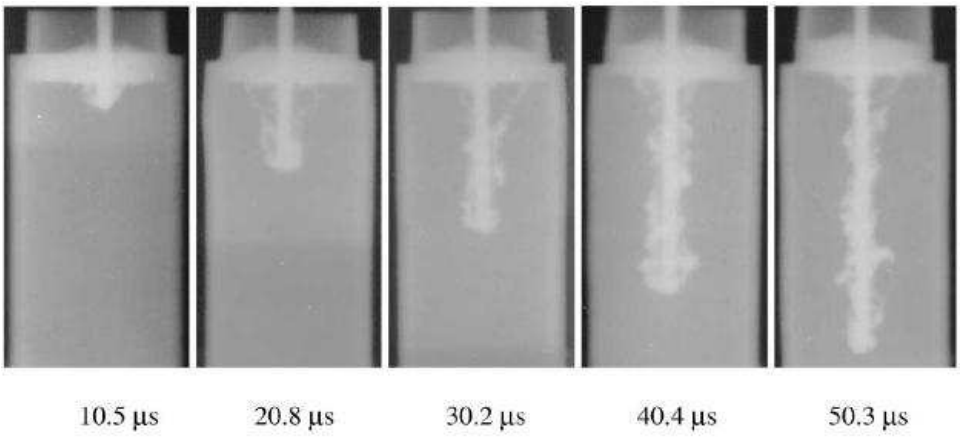

Figure 6.50: X-ray pictures at various instances in time from confined ceramic test where the impact velocity was 1581 m/s [49]

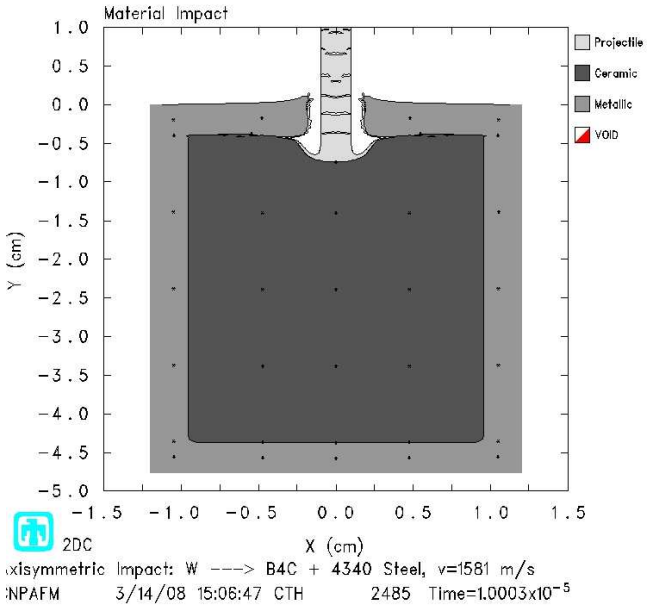

Figure 6.51: Material impact for tungsten projectile on a boron carbide and 4340 steel target at 1581 m/s (10 μs)

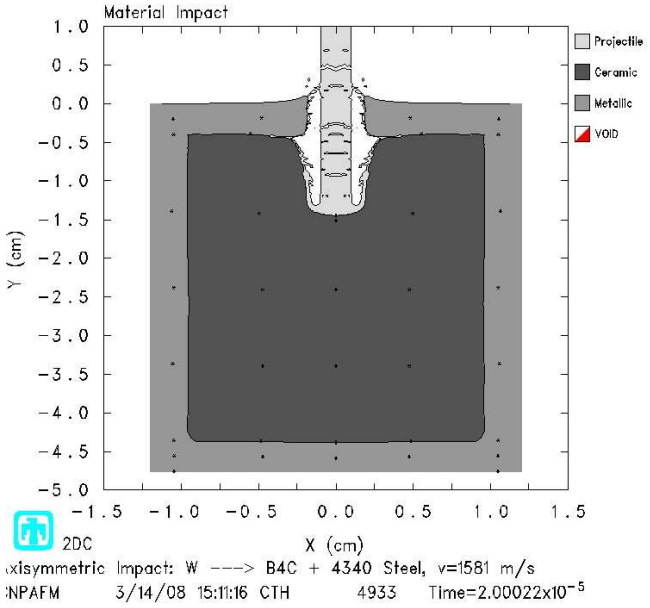

Figure 6.52: Material impact for tungsten projectile on a boron carbide and 4340 steel target at 1581 m/s (20 μs)

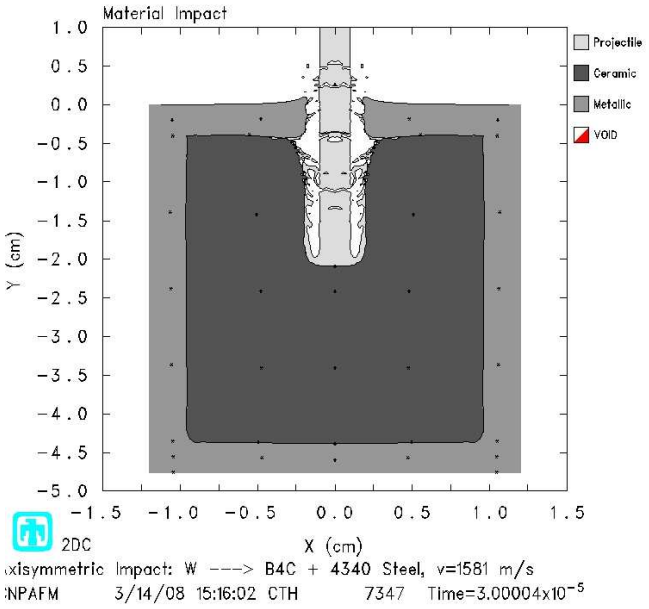

Figure 6.53: Material impact for tungsten projectile on a boron carbide and 4340 steel target at 1581 m/s (30 μs)

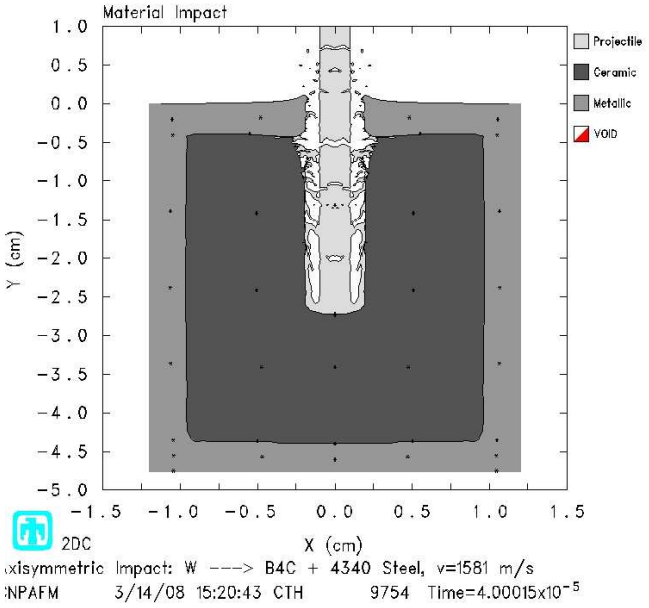

Figure 6.54: Material impact for tungsten projectile on a boron carbide and 4340 steel target at 1581 m/s (40 μs)

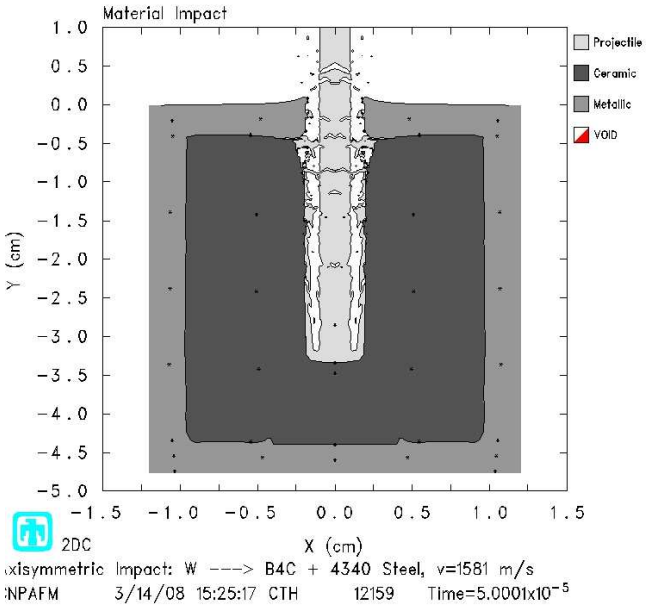

Figure 6.55: Material impact for tungsten projectile on a boron carbide and 4340 steel target at 1581 m/s (50 μs)

6.3 Ceramic Armor

As discussed previously in Section 5.3, the first ceramic target consisted of just one layer of B_4C ceramic that was confined completely by rolled homogeneous armor. The subsequent ceramic armor targets replaced layers of RHA by the appropriate amount of B_4C such that the total target thickness remained the same. Figures 5.6 (a)–(d) show what these models look like. Just like the first layer of ceramic, each additional layer was also approximately 0.5 cm in thickness.

The NOFREEZE option discussed earlier in this chapter, was implemented on the armor arrangement that consisted of two layers for various velocities ranging from 500-1250 m/s. When comparing the results for the depth of penetration from these runs compared to the runs that did not use NOFREEZE, there was no difference in the output; therefore, this option was not implemented in the remaining ceramic armor arrangements.

While hardness values are available for both the S7 tool steel and the B_4C ceramic, no hardness values could be found that used the same hardness scale. No conversion factors could be obtained to equate the different hardness scales for the values found. The hard and soft material designations when using the BLINT algorithm for the interface between the projectile and the ceramic were run two different ways for each target arrangement and then compared. The first way consisted of identifying the projectile as the hard material and the ceramic as the soft material. The second way switched these designations so that the ceramic was identified as the hard material and the projectile was the soft material.

For each ceramic arrangement, CTH was run for a range of impact velocities where the depth of penetration at each velocity was determined. The depths of penetration were then plotted against the impact velocities. A polynomial curve was used to fit the data and then projected forward for each ceramic arrangement. The point where the trendline intersected the line identifying the target thickness was determined to be the approximate ballistic limit of that target for the given projectile.

The depth of penetration versus impact velocity graphs for each of the four ceramic targets are shown in Figures 6.56 through 6.59 for the case where the projectile is designated as the hard material in the BLINT algorithm and the case where the ceramic is designated as the hard material.

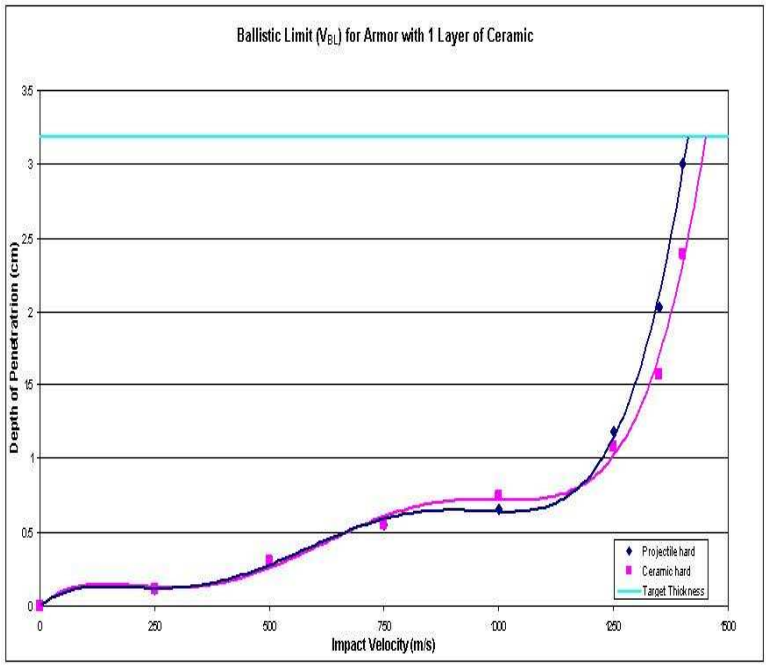

Figure 6.56: Ballistic Limit for armor with 1 layer of ceramic

The estimated ballistic limits for each of the armor arrangements for all four of these target arrangements are listed in Table 6.5. As was expected, the simulations where the ceramic was considered to be the harder material had higher ballistic limits than the runs where the projectile was designated as the hard material. The results in this table show that as the metal layers in the target are replaced by ceramic the ballistic limit decrease, and therefore, the ability of the target to resist penetration is also decreasing. The target that contains four layers of B_4C has a ballistic limit that is approximately 40 percent less than the ballistic limit with just one layer of ceramic.

CTH was then run to show the simulated material impact of the four targets at velocities near their estimated ballistic limits. Figures 6.60 through 6.63 show the

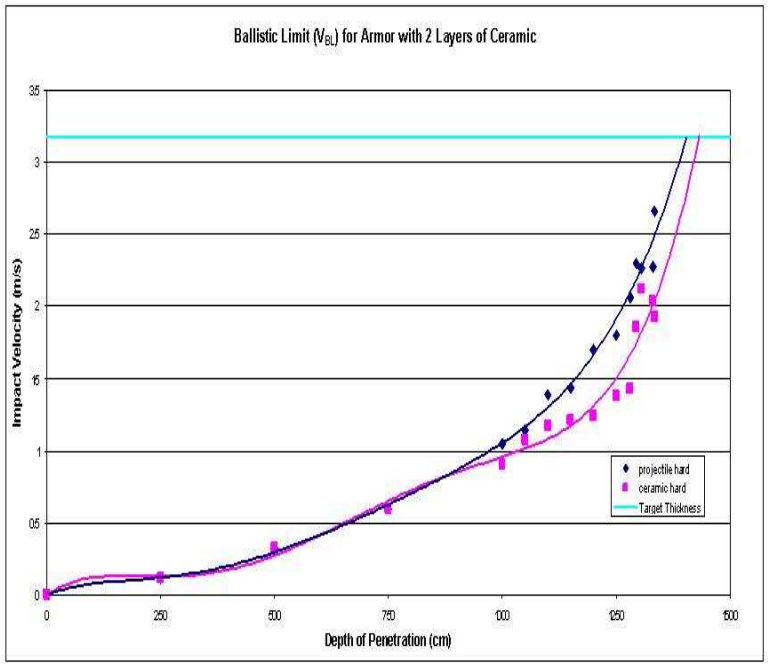

Figure 6.57: Ballistic Limit for armor with 2 layers of ceramic

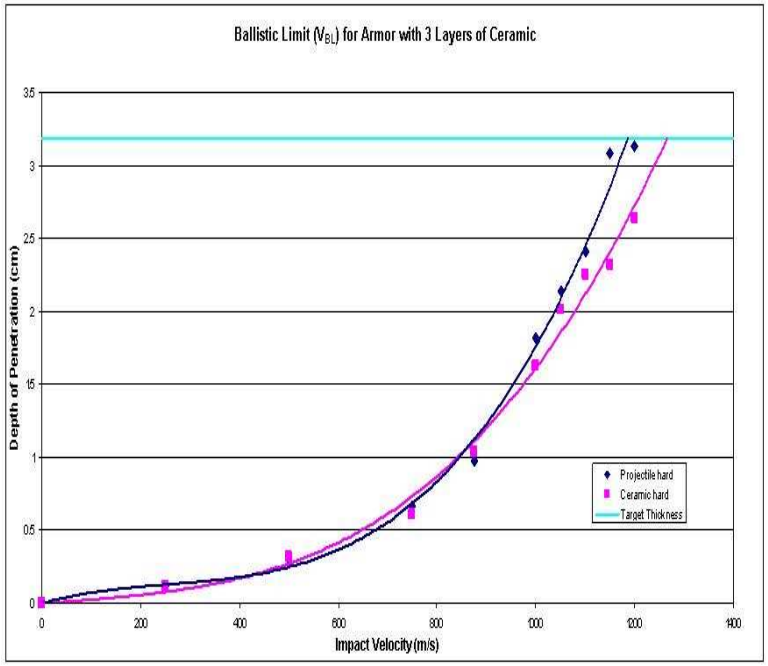

Figure 6.58: Ballistic Limit for armor with 3 layers of ceramic

contour plots of the material impact for each of these four target configurations with the ceramic designated as the hard material in the BLINT algorithm. Figures 6.60

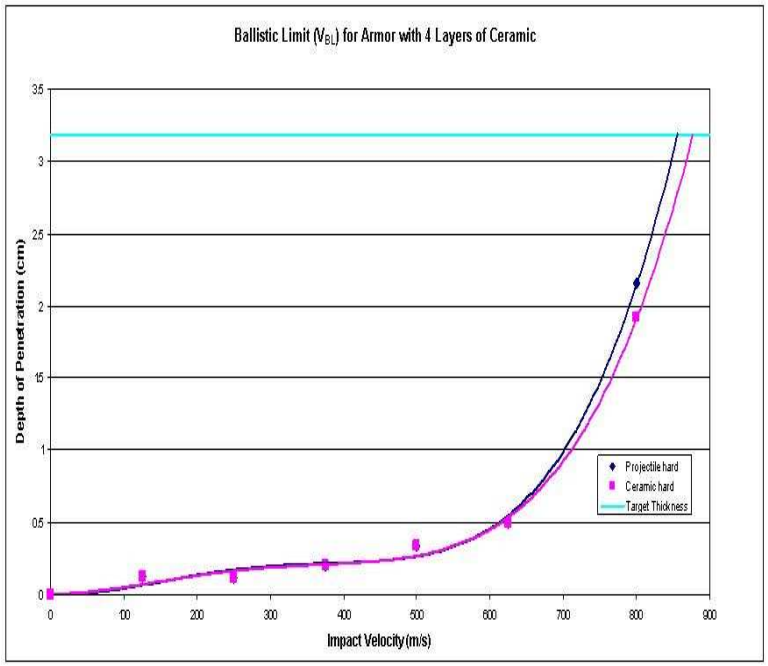

Figure 6.59: Ballistic Limit for armor with 4 layers of ceramic

Table 6.5: Ballistic limit for ceramic armor configurations

Number of ceramic layers	Ballistic limit (m/s)	
	projectile hard	ceramic hard
1	1412	1451
2	1404	1433
3	1190	1265
4	856	877

(a)–(d) shows the impact for the target configuration with only one layer of ceramic where approximately 60 percent of the projectile is eroded. It also shows the projectile producing a cylindrical cavity and the eventual failure of the plate due to plugging.

Figures 6.61 (a)–(d) shows the projectile penetrating through target consisting of two layers of B_4C at an impact velocity of 1350 m/s. This impact velocity is approximately six percent lower than the value predicted to be the ballistic limit. These figures show that the failure mode for the target is due to plugging. The amount of material being sheared out of the target is wider than the projectile; whereas, in the previous case the projectile sheared out a plug that was basically the same width as

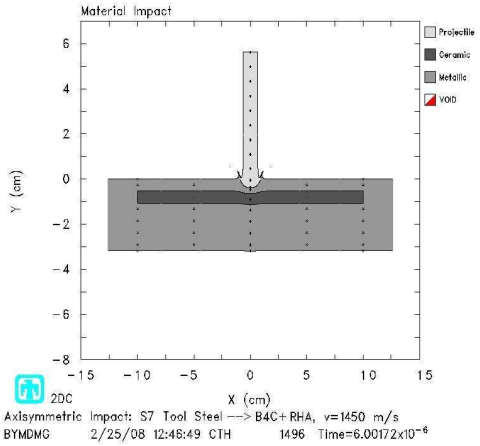

(a) 6 μs

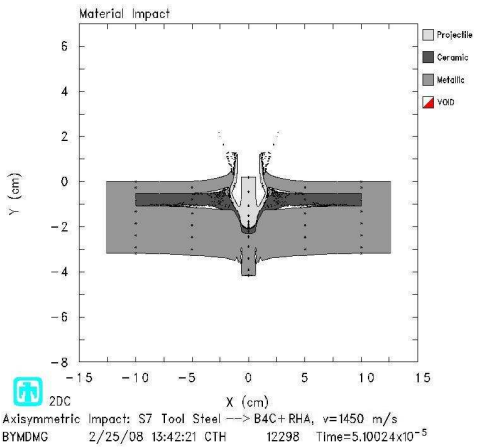

(b) 51 μs

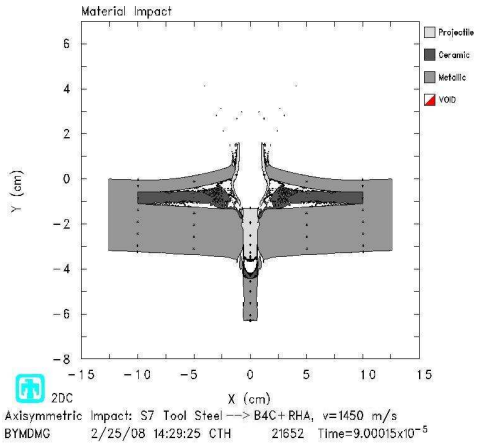

(c) 90 μs

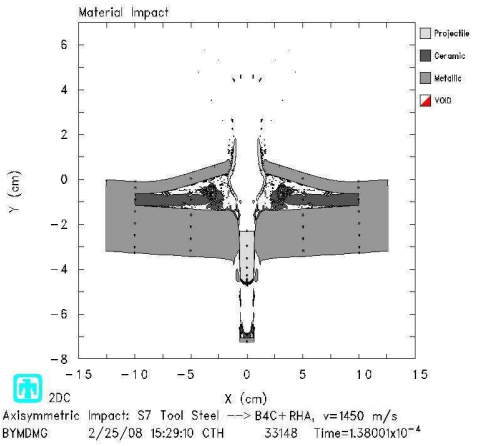

(d) 138 μs

Figure 6.60: Material impact for S7 tool steel projectile on confined one-layer ceramic target at 1450 m/s

the projectile. It is also observed that the approximately 80 percent of the projectile is eroded. At 51 μs, the fracture pattern of the ceramic can be seen. The ceramic fractures diagonally moving outward from the upper surface of the ceramic to the bottom surface. This is a common observance for brittle materials. Thinking about it in three-dimensional terms, the fractured portion of the ceramic is a cone with the point truncated.

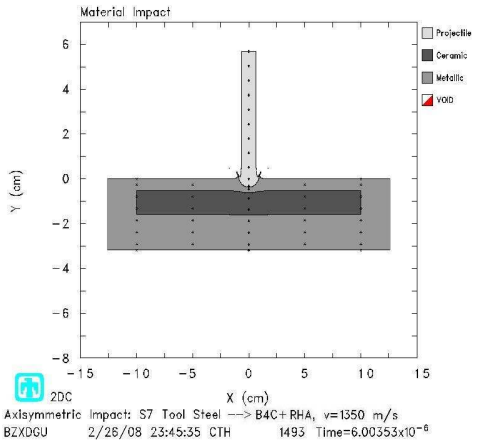

(a) 6 μs

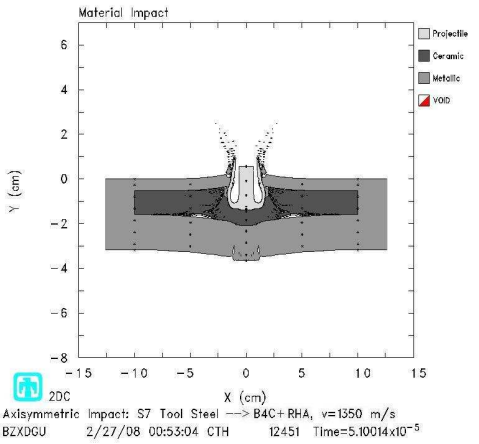

(b) 51 μs

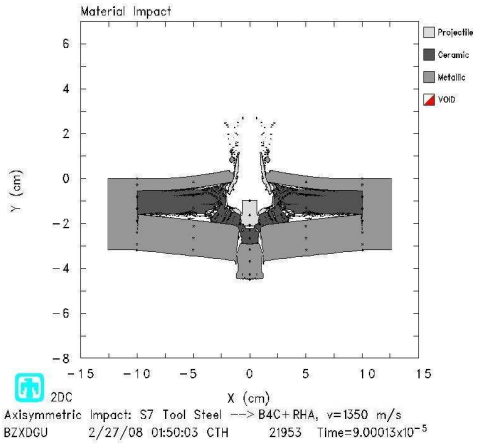

(c) 90 μs

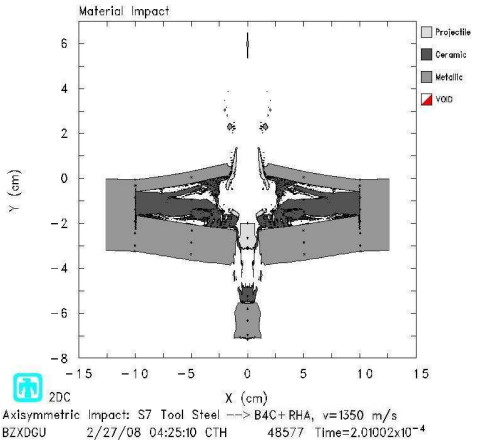

(d) 201 μs

Figure 6.61: Material impact for S7 tool steel projectile on confined two-layer ceramic target at 1350 m/s

The material impact for the three-layer ceramic target as shown in Figures 6.62 (a)–(d) appears to be very similar to the two-layer ceramic target. This target configuration also fails due to plugging of the ceramic and metallic layers. The ceramic once again fractures diagonally, but this time there appears to be more fracturing and cracking of the ceramic material. The projectile does not erode quite as much as the two-layer target configuration, but it fracture more the one-layer ceramic target does.

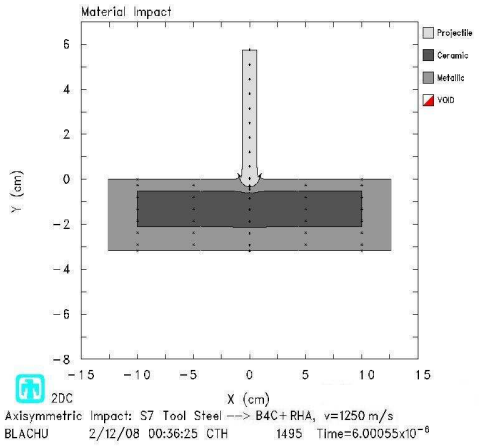

(a) 6 μs

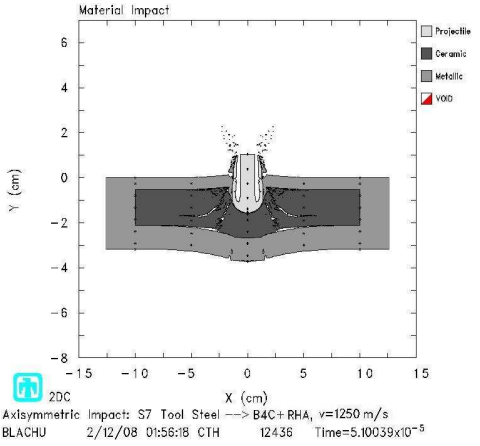

(b) 51 μs

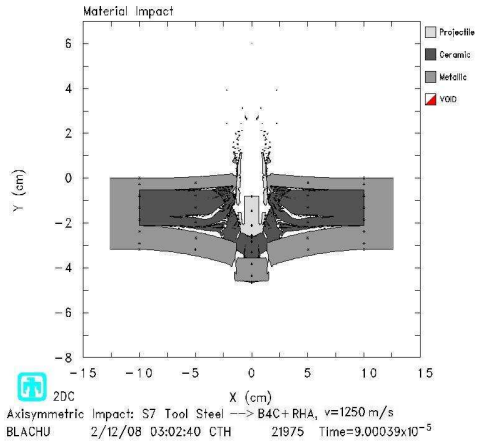

(c) 90 μs

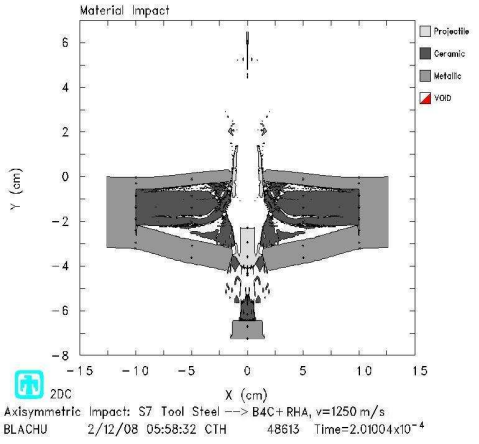

(d) 201 μs

Figure 6.62: Material impact for S7 tool steel projectile on confined three-layer ceramic target at 1250 m/s

The projectile is shown impacting the four-layer ceramic target arrangement in Figures 6.63 at an impact velocity of 850 m/s. In this simulation, the interface pressure where the projectile impacts the target is relatively low causing the projectile to only erode about 40 percent. Plugging failure is also observed for this target configuration. Once again, the diagonal fracture of the ceramic material can be seen very clearly. The upper surface of the ceramic is virtually undisturbed other than at the area of impact.

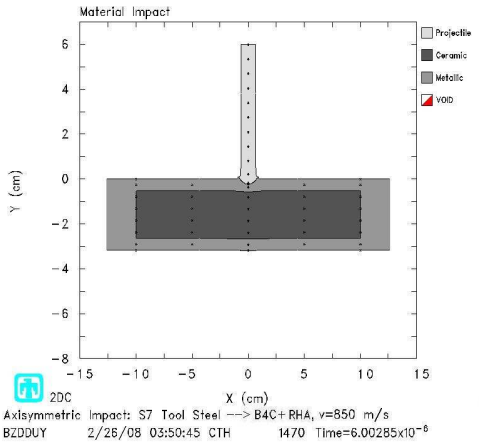

(a) 6 μs

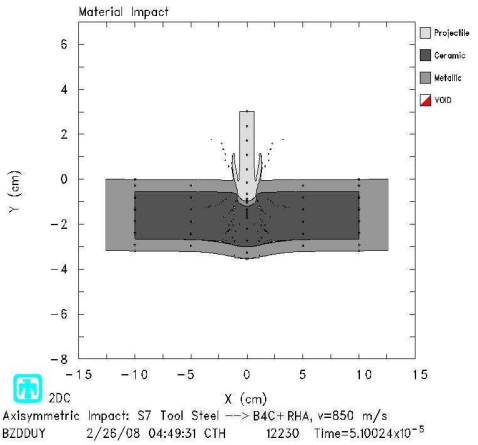

(b) 51 μs

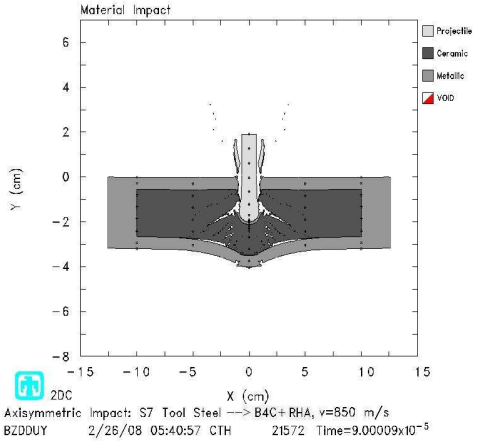

(c) 90 μs

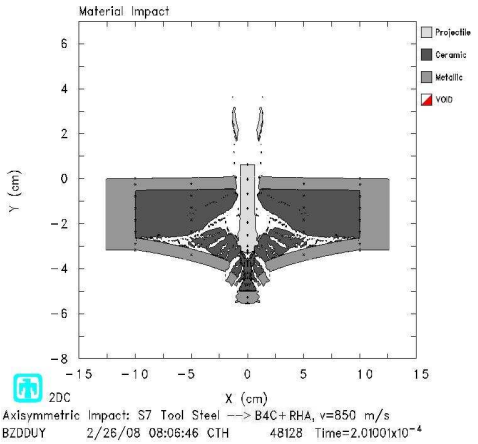

(d) 201 μs

Figure 6.63: Material impact for S7 tool steel projectile on confined four-layer ceramic target at 850 m/s

Figures 6.64 through 6.79 show the pressure history plots for all four target configurations. The first set of pressure plots shown in Figures 6.64–6.67 are for the target that contains only one layer of ceramic. It can be seen that the compression wave travels faster in the B_4C than it does in th RHA by how much wider the wave is, refer to Figure 6.64. By 6 μs, the initial compression wave has already propagated through the entire target and is reflecting of the bottom surface as a tension wave. The tension wave travels all the way up to the top surface of the target. However, the area of the target just below the ceramic and in the center remains in compression throughout the penetration process even as the pressure wave in the rest of the target changes between compression and tension.

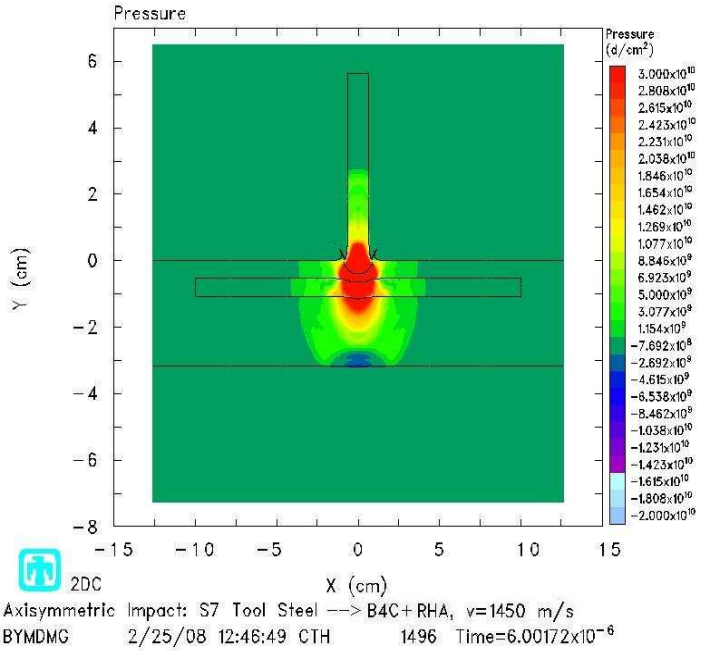

Figure 6.64: Pressure for S7 tool steel projectile impacting confined one-layer ceramic target at 1450 m/s (6 μs)

Figure 6.68 to Figure 6.71 depict the pressure during the impact event for the target consisting of two layers of ceramic. The propagation of the pressure waves in the three-layer ceramic are shown in Figures 6.72–6.75. Lastly, the pressure waves for the target configuration with four layers of ceramic are portrayed in Figures 6.76 through

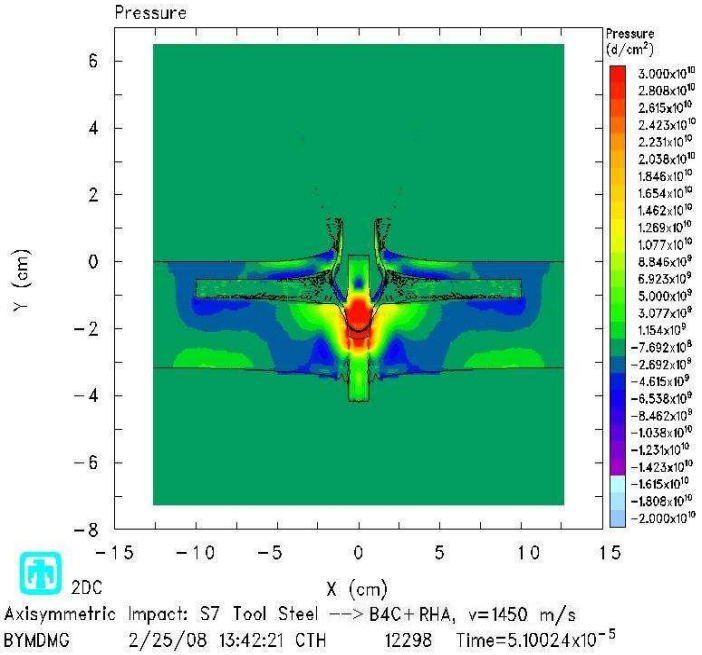

Figure 6.65: Pressure for S7 tool steel projectile impacting confined one-layer ceramic target at 1450 m/s (51 μs)

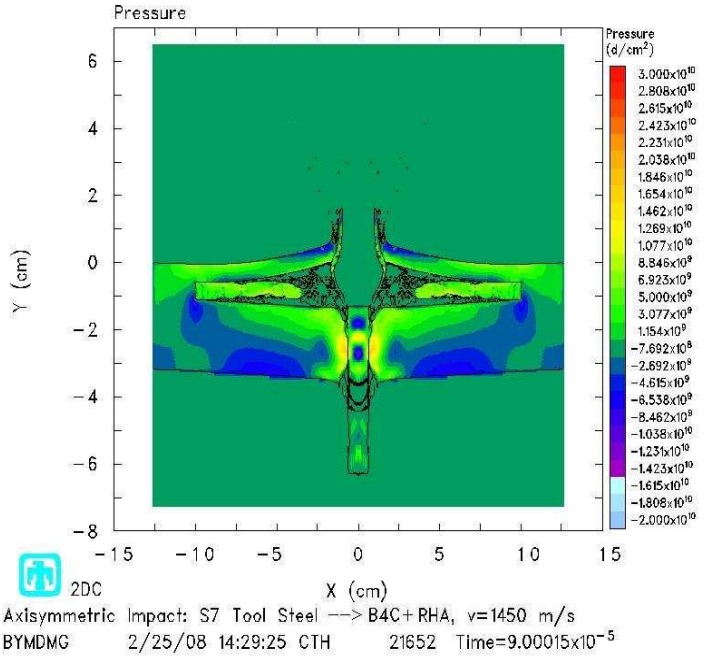

Figure 6.66: Pressure for S7 tool steel projectile impacting confined one-layer ceramic target at 1450 m/s (90 μs)

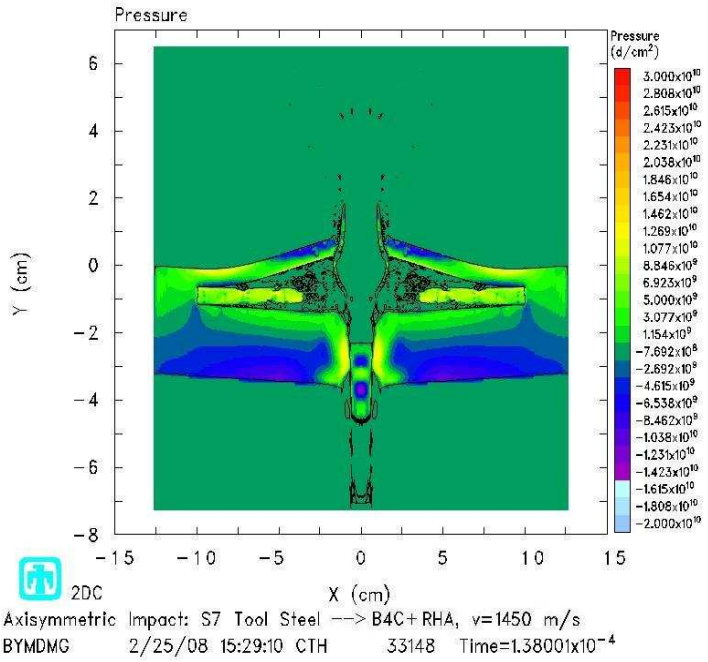

Figure 6.67: Pressure for S7 tool steel projectile impacting confined one-layer ceramic target at 1450 m/s (138 μs)

6.79. The two, three, and four-layer ceramic target arrangements show similar wave responses to the one-layer ceramic configuration. Once the waves reach steady state, a state of compression exists in all these configurations just below the ceramic layers. A state of tension exists at the very bottom of the target while the pressure wave in the metal layer at the top of the target continues to change between compression and tension. As more fracturing occurs in the ceramic, the waves are unable to transmit into and out of the ceramic. In Figure 6.77, there are two diagonal compression waves that are transmitted into the four-layer ceramic. Fracture of the ceramic in this target will eventually take place where the lower of the two diagonal compression waves originates.

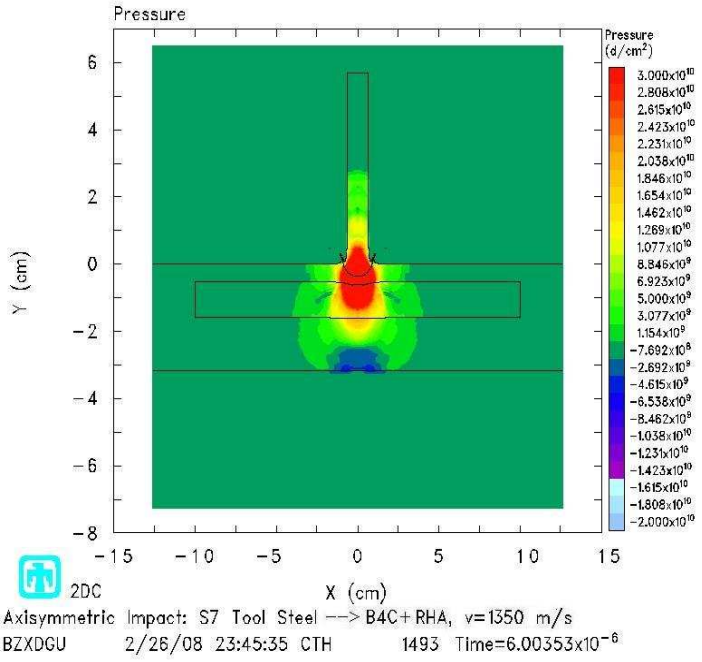

Figure 6.68: Pressure for S7 tool steel projectile impacting confined two-layer ceramic target at 1350 m/s (6 μs)

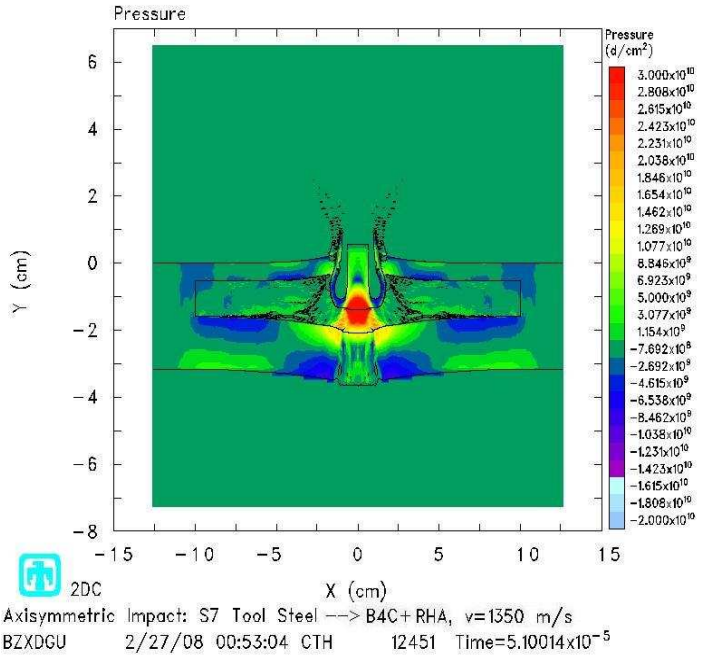

Figure 6.69: Pressure for S7 tool steel projectile impacting confined two-layer ceramic target at 1350 m/s (51 μs)

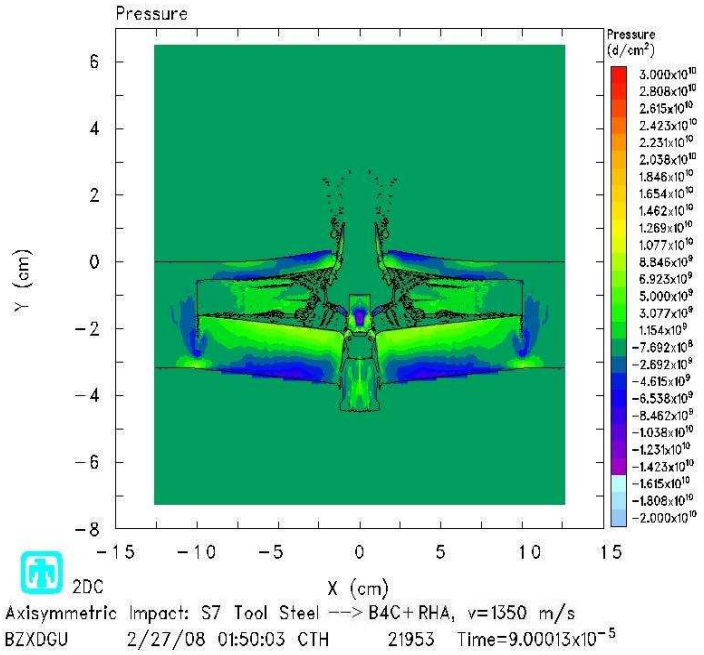

Figure 6.70: Pressure for S7 tool steel projectile impacting confined two-layer ceramic target at 1350 m/s (90 μs)

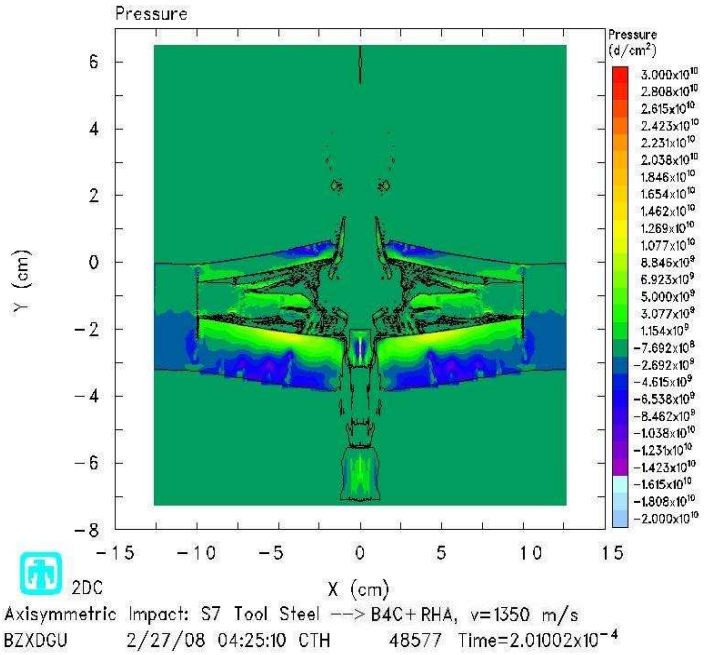

Figure 6.71: [Pressure for S7 tool steel projectile impacting confined two-layer ceramic target at 1350 m/s (201 μs)

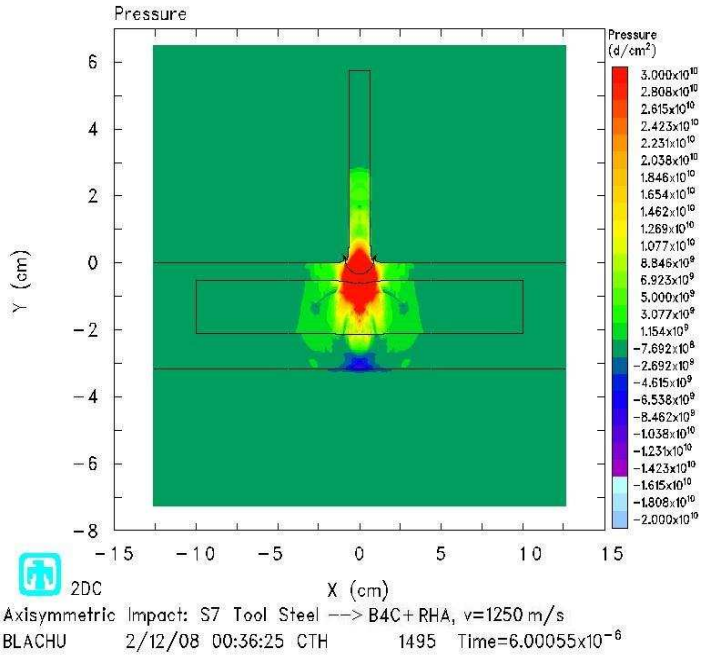

Figure 6.72: [Pressure for S7 tool steel projectile impacting confined three-layer ceramic target at 1250 m/s (6 μs)

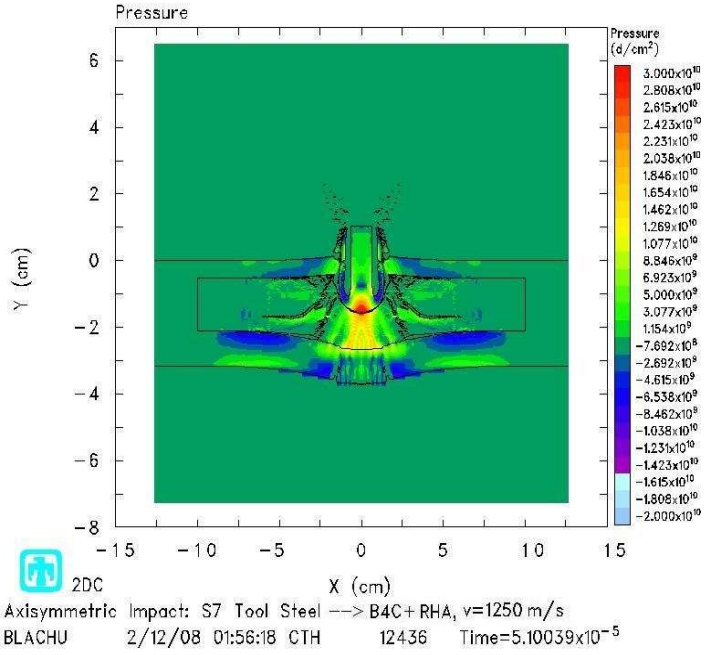

Figure 6.73: [Pressure for S7 tool steel projectile impacting confined three-layer ceramic target at 1250 m/s (51 μs)

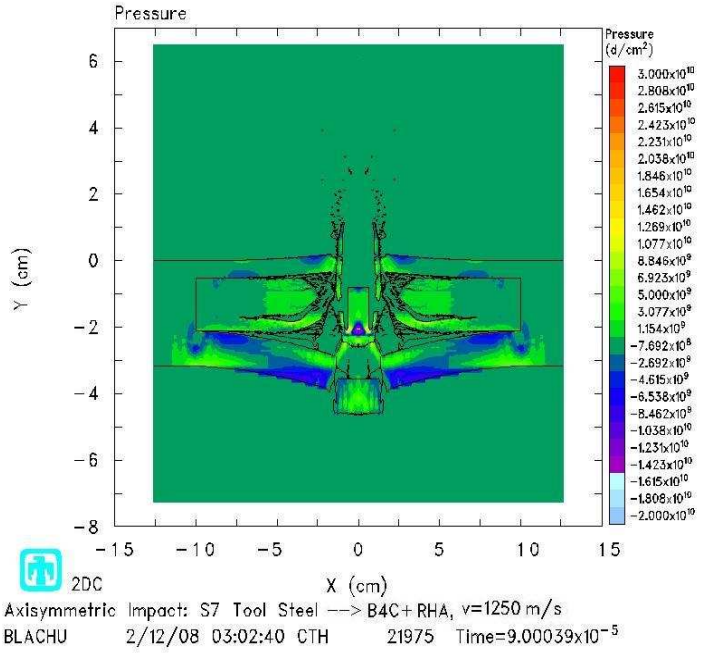

Figure 6.74: Pressure for S7 tool steel projectile impacting confined three-layer ceramic target at 1250 m/s (90 μs)

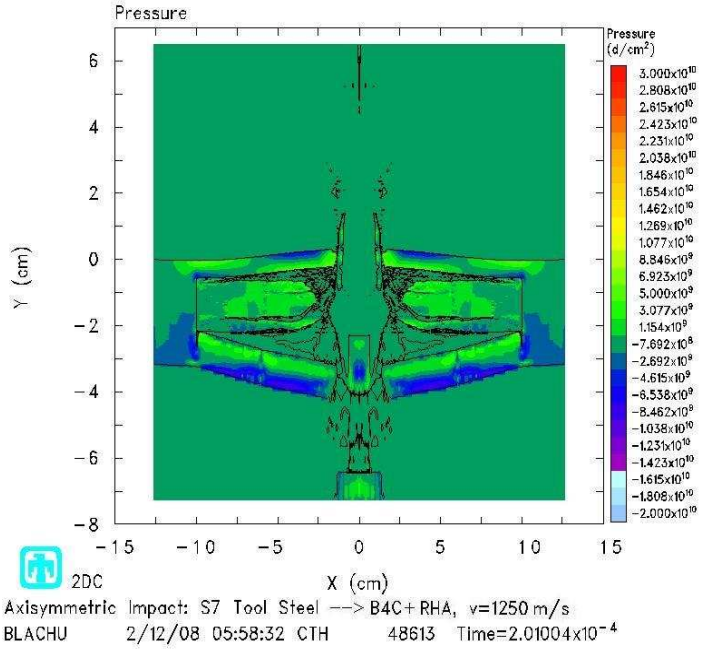

Figure 6.75: Pressure for S7 tool steel projectile impacting confined three-layer ceramic target at 1250 m/s (201 μs)

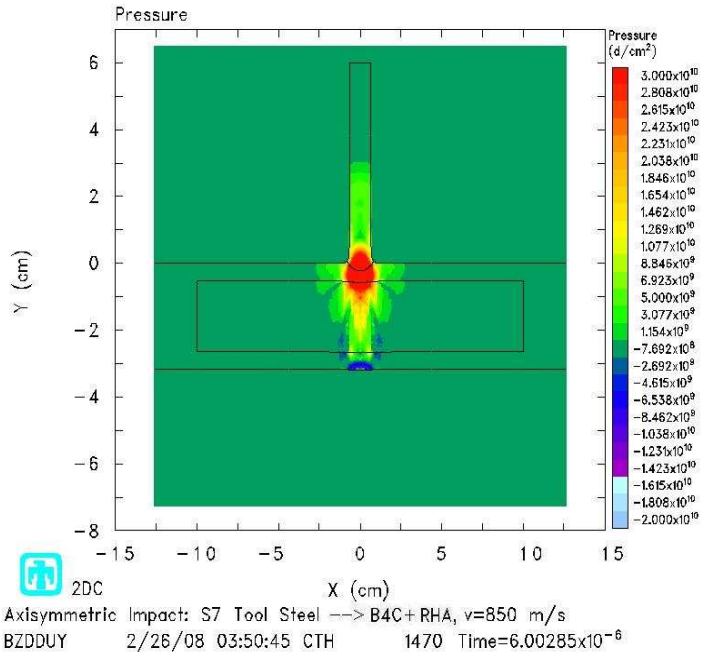

Figure 6.76: Pressure for S7 tool steel projectile impacting confined four-layer ceramic target at 850 m/s (6 μs)

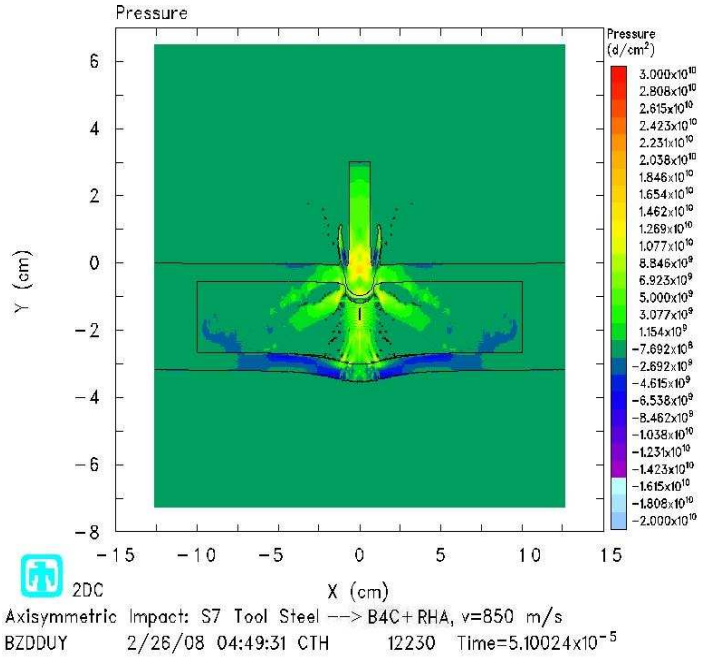

Figure 6.77: Pressure for S7 tool steel projectile impacting confined four-layer ceramic target at 850 m/s (51 μs)

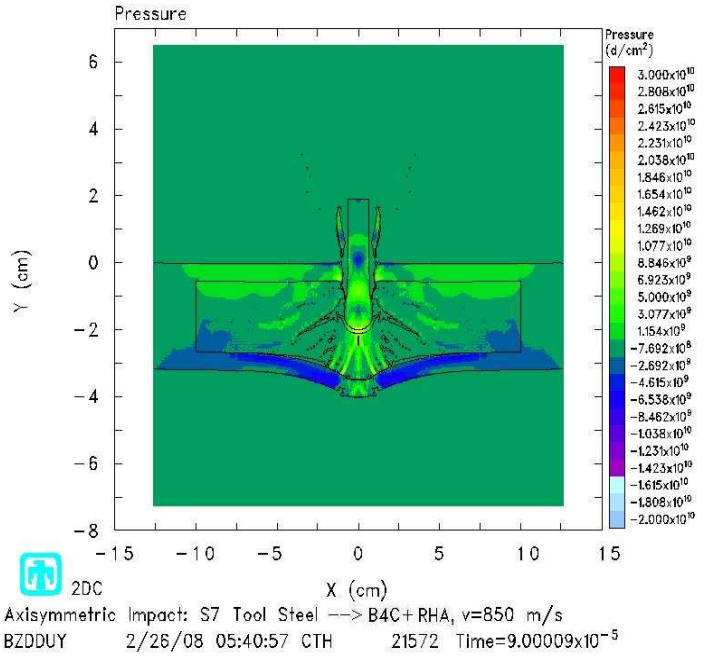

Figure 6.78: Pressure for S7 tool steel projectile impacting confined four-layer ceramic target at 850 m/s (90 μs)

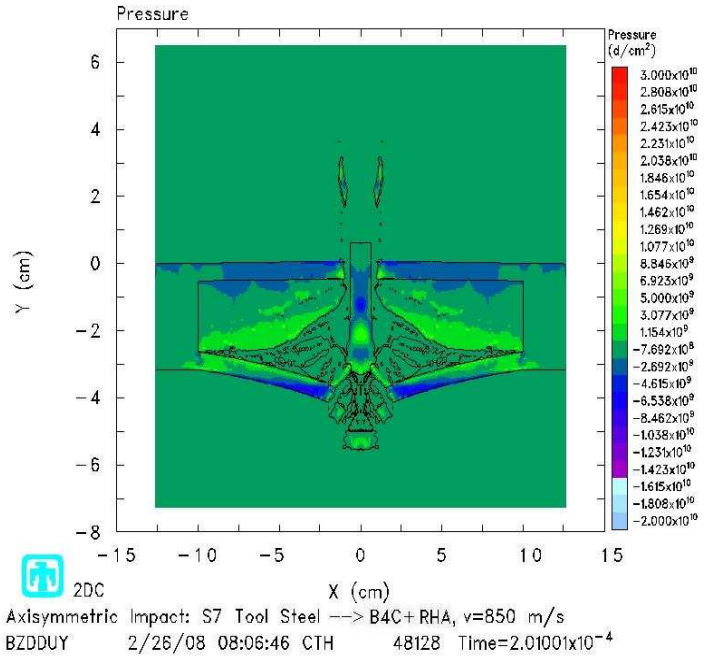

Figure 6.79: Pressure for S7 tool steel projectile impacting confined four-layer ceramic target at 850 m/s (201 μs)

In the case of the confined ceramic target, the ballistic limit for the target with just one layer of ceramic was only slightly less than the metallic target of the same thickness. In fact, when the case where the ceramic is designated as the hard material in the BLINT algorithm is taken into account, the one-layer ceramic target outperforms that same metallic target just considered. However, the targets with more than one layer of ceramic do worse in terms of ballistic limit when compared to the metallic target. When the amount of spall from Figure 6.35 (b) where the impact velocity was 1000 m/s is compared to the equivalent cases of the ceramic target with one, two, and three layers, it is observed that less spall is produced in the confined ceramic target than in the metallic target. In Figures 6.80 (a)–(c), the amount of spall for these three ceramic configurations can be seen in the material impact plots. From Figure 6.80 (a) it is seen that almost no spall is created; whereas, in the metallic target, a decent amount of material is ejected out the bottom of the target. A little more spalling occurred in the two and three-layer cases (Figures 6.80 (b) and (c)), but it was sparse when compared once again to the metallic target.

Just as in the first two models, it was recommended to look at the pressure plots for these targets [9]. The simulations run at the lower velocities managed to stay beneath the 13 GPA cut-off for phase change in iron; however, as the velocity was increased, the pressures produced at initial impact exceeded 13 GPa. This means that this problem should also be run with a model that can account for the phase transition in iron like PTRAN. Due to the amount of computational time required to run these simulations, these problems were not run again. However, it is expected that similar to the results in the first problem, the ballistic limit will be decreased. The projectile tip and the top metal layer will become stronger as they transition to the epsilon phase of iron. While this top layer will be more resistant to penetration, the remaining layers will appear to decrease in strength when compared to the tip of the projectile. This will result in targets that are perforated by the projectile at lower impact velocities (i.e. decreased ballistic limits).

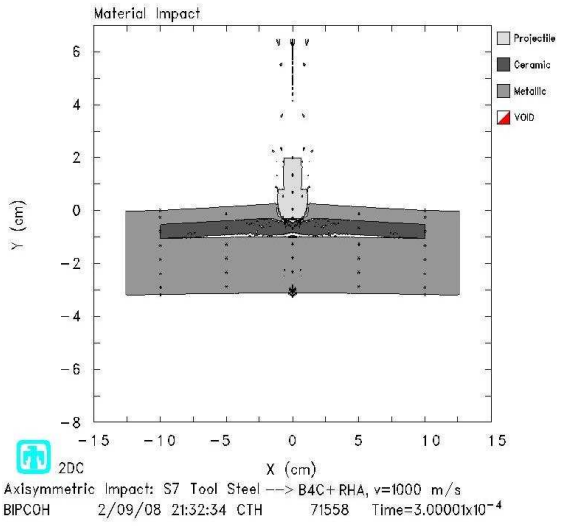

(a) One-layer confined ceramic target

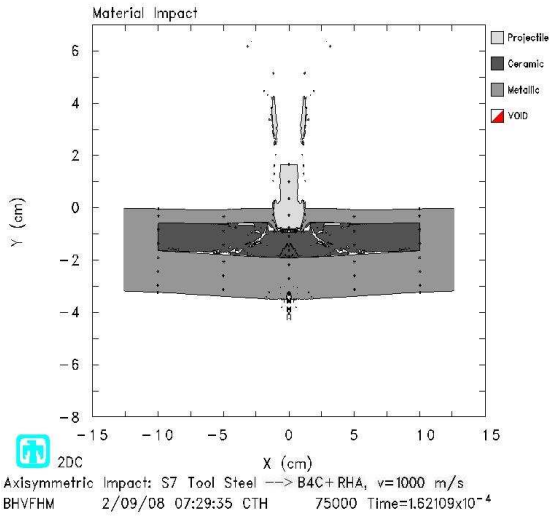

(b) Two-layer confined ceramic target

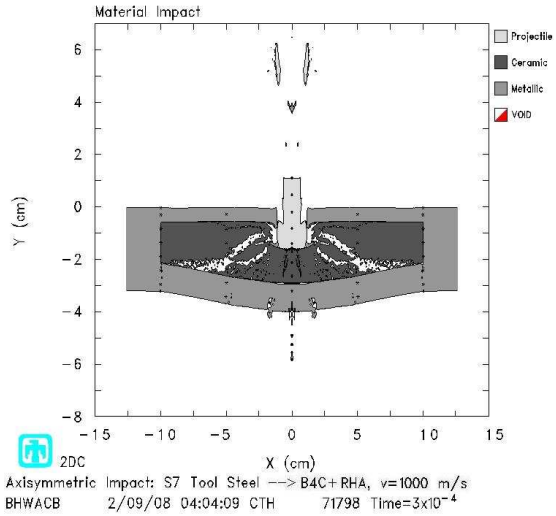

(c) Three-layer confined ceramic target

Figure 6.80: Spallation for confined two, three and four-layer ceramic targets (impact velocity is 1000 m/s)

6.3.1 Long-rod Projectile. One of the obvious differences between the ceramic armor discussed in this section and the confined ceramic example from Westerling, et al is the type of projectile being used. In the confined ceramic example, a tungsten long-rod projectile with a large L/D and a mass of approximately 9 grams

is used; whereas, in the ceramic armor and in the Zukas and Scheffler problem, the hardened steel projectile has a L/D of 5 and a mass of 65 grams. Clearly, the projectile with the higher mass is going to have the higher kinetic energy as well. To get a better feel for this difference, the ceramic armor target with four layers of ceramic was run again with a long-rod projectile impacting it at 1500 m/s. This impact velocity is almost twice as fast as the ballistic limit of the target with the 65-gram projectile. The long-rod projectile has the same dimension as the projectile in the confined ceramic case other than it has a hemispherical tip to be consistent with the other projectile. Also for consistency, the material used for the projectile is the same S7 tool steel giving it a mass of approximately 3.7 grams. The PTRAN EOS for iron was used for the projectile and the steel case.

From the material impact shown in Figures 6.81 (a)–(d), it is observed that the rod is eroding from the very beginning. As the projectile is entering the ceramic, the ceramic begins to fracture along the interface between the ceramic and the top metallic layer. By 54 μs, the projectile does not penetrate any further into the target. With the projectile at max depth, more cracking is witnessed at about one quarter of a centimeter down into the ceramic. The projectile penetrates less than one cm into the target. As discussed previously, this makes sense due to the mass being so much smaller than the 65-gram projectile. Even at nearly twice the impact velocity, the long-rod projectile has less than one-fifth of the kinetic energy that the intermediate-rod projectile has.

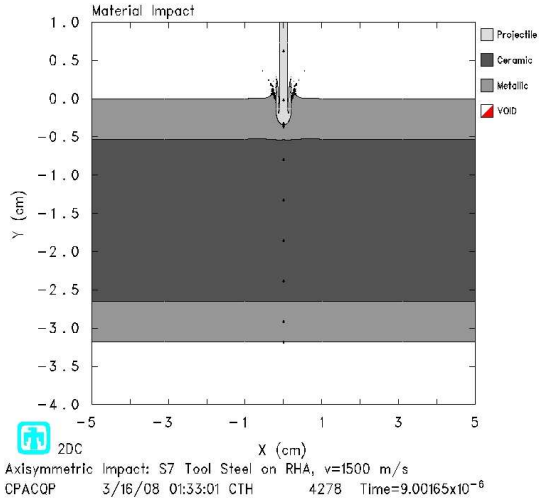

(a)

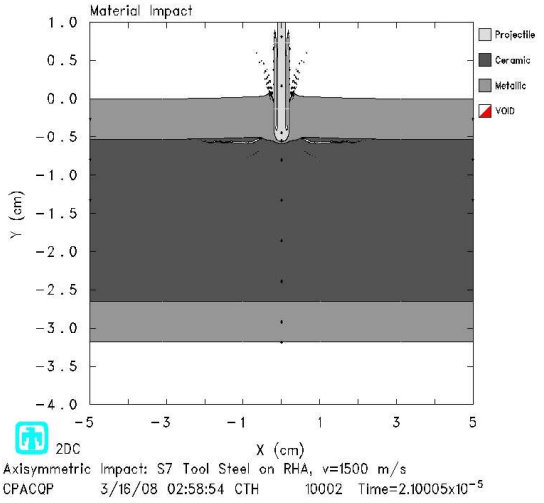

(b)

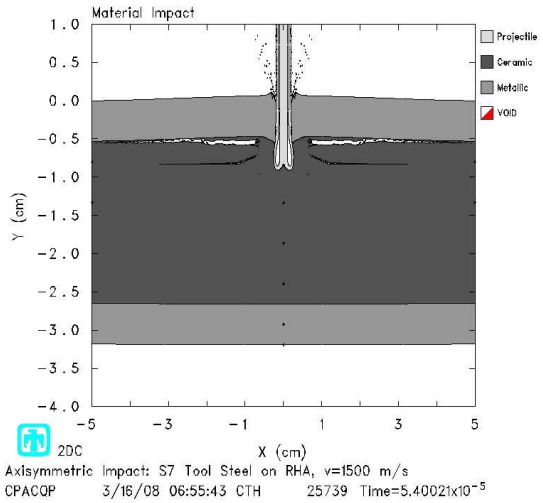

(c)

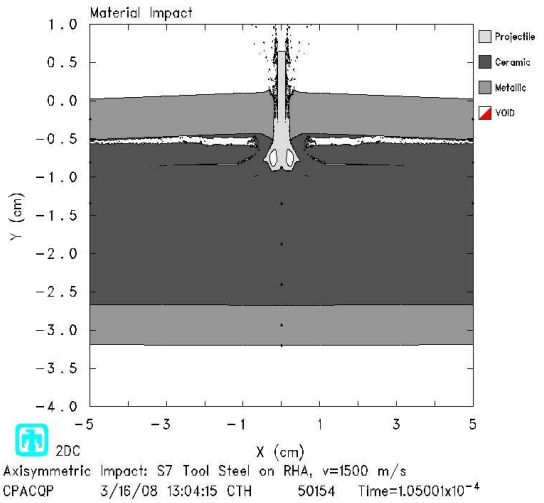

(d)

Figure 6.81: Material impact of a long-rod projectile on four-layer ceramic target impacting at 1500 m/s

VII. Conclusions

In this closing chapter a final overview is given of the research that was accomplished in this thesis. Next, the most important findings and contributions are discussed. This is followed by the recommendations for future areas of research.

7.1 Conclusions

The purpose of this research was to numerically simulate impact of cylindrical projectile with a hemispherical tip into a confined ceramic target in order to determine the feasibility of the ceramic at defeating a given projectile. The Eulerian hydrocode CTH was used to numerically simulate the impact of the projectile into the target. To reach the objective of accurately modeling a confined ceramic armor, multiple different models were used.

The initial model used a multi-layer target previously analyzed by Zukas & Scheffler [56]. This simulation was performed to determine which parameters to use in the ceramic armor simulations. This problem provided experience modeling a target made up of multiple metallic layers that all consist of the same material. This model also provided some comparison for the performance of the confined ceramic target. The values for the normalized residual velocities produced from this simulation did not match those from the Lagrangian code ZeuS. However, the overall trend of the data followed that of the ZeuS data in that increasing the number of layers for a target of a certain thickness makes the target significantly weaker. It was determined that the target without gaps (i.e. bonded layers) had a higher ballistic limit than the target with gaps between the layers (i.e. layers are allowed to slide). It was found that at the the higher impact velocities that the projectile tip and the upper region of the target experienced high pressures immediately upon impact. Since iron exhibits a phase transition under a shock loading of 13 GPa, it was necessary to include an EOS that could handle this phase transition. The PTRAN EOS in CTH takes care of this phase change for iron. When this EOS model was used, the ballistic limits decreased for both the target with and without gaps by about three percent.

A comparison of some of the boundary conditions available in CTH was also performed. Three of the available options in CTH were tried on the side boundary. It was observed that the Type 0 boundary condition behaves like a completely rigid boundary. The Type 1 was seen to be a good option to approximate infinite and semi-infinite boundaries. The Type 2 boundary condition was observed to do a good job of modeling a finite boundary. The Type 2 boundary condition is the option that was used for the side boundary in all of the other simulations.

The next phase involved impact of a confined ceramic target that was studied by Westerling, Lundberg & Lundberg [49]. The results obtained from this simulation were compared to the data produced by the authors using the AUTODYN-2D code. The comparison of this data was done to verify the ability of CTH to accurately handle the confined ceramic problem. A comparison using a couple of the options for the MIX algorithm in CTH was also performed. The MIX=3 option seemed to match the depth of penetration data better for both the experimental data and the simulations from the Lagrangian code AUTODYN-2D. For the high impact velocities that were simulated here, the depth of penetration over the time the impact took place was linear which matched well with both the experimental data and the AUTODYN-2D simulations performed by the authors. A linear curve fit of the data was used to determine the penetration velocity based on the slope of the line for each impact velocity. In general, the MIX=3 option was determined to match the AUTODYN-2D values better while the MIX=5 option compared more favorably with the experimental data. These results showed that CTH can accurately model impact of a long-rod projectile on a confined ceramic target.

Similarly to the second phase of this research, the final part of this effort consisted of projectile impact of a confined ceramic model. The projectile was used from the initial model used by Zukas and Scheffler. The targets consisted of four different arrangements of RHA and B_4C. The target was modeled by taking the target from the initial model and replacing metallic layers two through five one-by-one with B_4C ceramic so that the fourth target iteration consisted of four layers of B_4C. Each re-

placement of a layer constituted a new target arrangement. This effort consisted of a comparison of what happens when the projectile is harder than the ceramic and when the opposite case is true. The ballistic limit of the target where the ceramic was designated as being harder resulted in a ballistic limit that was 2–6 percent higher than the case where the projectile was designated as harder. This, of course, makes sense that setting the ceramic to be harder will result in a target that is more resistant to penetration of the projectile resulting in a higher ballistic limit.

The velocities that the multi-layer ceramic targets failed at were not that high relative to many of the research efforts mentioned in Section 1.2. However, most of those efforts dealt with long-rod projectile with L/D ratios of 10 to 20 with projectile diameters on the order of millimeters. The four-layer ceramic target was impacted by a long-rod projectile to get a better idea of the difference between this type of long-rod projectile and the projectile used by Zukas and Scheffler. The long-rod projectile used was dimensionally similar to the projectile in the confined ceramic example and was made out of S7 tool steel. This projectile impacted at a velocity of 1500 m/s, but due to its significantly smaller mass was unable to penetrate even one-third of the way into the target. This is significant when you consider that the ballistic limit of the four-layer ceramic target impacted by the other projectile was approximately 850 m/s.

7.2 Recommendations for Future Research

This research dealt purely with impact that was normal to the surface of the target. However, most of the time there will be some yaw angle of the projectile relative to the target surface. Therefore, it is necessary that oblique impact of projectiles be investigated for the use of ceramic armor.

This research has shown that the ceramic target of a given thickness did not perform as well as the metallic targets of the same thickness; however, the density of the ceramic is about one-fifth of the density of the RHA steel. It is conceivable that a ceramic target could be designed that is thicker than the metallic target used

yet lighter and with just as good or better ballistic limit. Further efforts need to be carried out to compare metallic and ceramic targets of equivalent mass, instead of equivalent thickness.

Other ceramics as well as functionally graded materials (FGM), which are advanced composites whose properties vary continuously through some dimension of the material, are being used in more and more areas where full advantage of their unique properties can be realized. These varying materials should studied to determine what benefit they have in this field.

Another good area of future research could consist of the material and shape of the projectile. This study used a projectile with a hemispherical nose which was studied by Zukas and Scheffler. However, at high velocities many projectiles have more of a conical nose. Also any new materials that are being used for projectiles should be taken into account.

In the case of this research the side confinements were chosen be a certain thickness. It could be beneficial to see what effect takes place, if any for the penetration of a projectile as the side confinement changes in thickness. The casing should also be examined for materials other than steels, such as alloys of aluminum and titanium. In some body armors the top and bottom plates are made of composites like kevlar, instead of metals. This could also be a valuable area of research, as well as if the target is then encased in a rubber-like material.

The majority of this research consisted of using finite boundary conditions for the sides of the armor plates. However, there is also ceramic armor being made that is molded body armor. This armor consists of the metal reinforcements to prevent the armor from bending and failing in tension; however, since it is a continuous ceramic, the side boundaries, in most cases, can be considered so far from the area of impact that the side boundary conditions can be modeled as semi-infinite so that the reflection of waves off the sides does not come into play.

Appendix A. CTH Input File

This Appendix includes one sample input file for each of the three main problems run in this research. The first input file is for the multi-layer metallic target from Zukas and Schefflers research. The second input file is for the problem that was compared to the confined ceramic target from Westerling, Lundberg and Lundberg study. The last input file was used for the multi-layer metallic and ceramic target.

A.1 Multi-layer Target Example

```
*eor* genin

Axisymmetric Impact: S7 Tool Steel on RHA, v=1380 m/s

*An asterisk "*" is used to comment out a line

control
  mmp
  ep
endcontrol

mesh
* Define the mesh for the problem

  block 1 geom=2dc type=e
 * 2dc is two-dimensional cylindrical geometry
 * e is Eulerian mesh

    x0=0  * smallest value of X coordinate for mesh

    * n is number of cells,
    * w is width of the total region
    * dxf is the width of the first cell in this region
    * dxl is the width of the last cell in this region
      x1  w=10.000  dxf=0.0400  dxl=0.0400

    endx

    y0=-7.23  * smallest value of Y coordinate for mesh

    * The format is the same as for the X records
      y1  w=14.730  dyf=0.0400  dyl=0.0400
```

```
    endy

   * Define the upper and lower bouns of the active X & Y mesh
    xaction=0,0.65
    yaction=-0.53,7.5

  endblock
endmesh

insertion of material
* Required identifier to insert the materials

 endblock
endinsertion

insertion of material

  block 1

 * model half of the projectile and target and then
 * mirror results in cthplt file

   * Define projectile materials, geometry and velocity
    package projectile shaft
      material 1
      numsub 50
      yvel -138000
      insert box
        p1        0     0.65
        p2     0.65      6.5
      endinsert

      delete circle
        center 0    0.65
        radius 0.65
      enddelete
    endpackage

    package projectile tip
      material 1
      numsub 50
      yvel -138000
```

```
  insert circle
    center 0    0.65
    radius 0.65
  endinsert
 endpackage

* Define target materials and geometry
 package target 1
  material 2
  numsub 50
  insert box
    p1        0    -0.53
    p2       10        0
  endinsert
 endpackage

 package target 2
  material 3
  numsub 50
  insert box
    p1        0    -1.07
    p2       10    -0.54
  endinsert
 endpackage

 package target 3
  material 4
  numsub 50
  insert box
    p1        0    -1.61
    p2       10    -1.08
  endinsert
 endpackage

 package target 4
  material 5
  numsub 50
  insert box
    p1        0    -2.15
    p2       10    -1.62
  endinsert
 endpackage
```

```
    package target 5
      material 6
      numsub 50
      insert box
        p1        0    -2.69
        p2       10    -2.16
      endinsert
    endpackage

    package target 6
      material 7
      numsub 50
      insert box
        p1        0    -3.23
        p2       10     -2.7
      endinsert
    endpackage

  endblock

endinsertion

edit
  block 1
    expanded
  endblock
endedit

eos
 * PTRAN EOS for Iron (models phase transition that occurs in
 * Iron under shock loading of 13 GPa)
 * Iron EOS is very close to EOS for Steel
  MAT1 PTRAN IRON
  MAT2 PTRAN IRON
  MAT3 PTRAN IRON
  MAT4 PTRAN IRON
  MAT5 PTRAN IRON
  MAT6 PTRAN IRON
  MAT7 PTRAN IRON
endeos

* Define the constitutive models for the materials
```

```
epdata  * Elastic Plastic data
  vpsave
  mix 3  * mix 3 = normalized vol avg yeild strength

  * Johnson-Cook Viscoplastic Model for S7 tool steel (projectile)
    matep 1 JO S7_TOOL_STEEL
    tmelt 1.0
    * Johnson-Cook Fracture Model for steel
      jfrac steel
      jfpf0 -2e+10 * pressure at failure under conditions of
                   * hydrostatic tension
                   * This value must equal the corresponding PFRAC
                   * value in the FRACTS input set

   * Johnson-Cook Viscoplastic Model for RHA (target layer 1)
    matep 2 JO RHA
    tmelt 1.0
    * Johnson-Cook Fracture Model for RHA (user defined)
      jfrac user
      jfd1 -1
      jfd2 1.25
      jfd3 -0.5
      jfd4 0.001
      jfd5 0.98
      jftm 0.155
      jfpf0 -1.5e+10 * pressure at failure under conditions of
                     * hydrostatic tension
                     * This value must equal the corresponding PFRAC
                     * value in the FRACTS input set

   * Johnson-Cook Viscoplastic Model for RHA (target layer 2)
    matep 3 JO RHA
    tmelt 1.0
    * Johnson-Cook Fracture Model for RHA (user defined)
      jfrac user
      jfd1 -1
      jfd2 1.25
      jfd3 -0.5
      jfd4 0.001
      jfd5 0.98
      jftm 0.155
      jfpf0 -1.5e+10 * pressure at failure under conditions of
                     * hydrostatic tension
```

```
                * This value must equal the corresponding PFRAC
                * value in the FRACTS input set

* Johnson-Cook Viscoplastic Model for RHA (target layer 3)
 matep 4 JO RHA
 tmelt 1.0
 * Johnson-Cook Fracture Model for RHA (user defined)
   jfrac user
   jfd1 -1
   jfd2 1.25
   jfd3 -0.5
   jfd4 0.001
   jfd5 0.98
   jftm 0.155
   jfpf0 -1.5e+10 * pressure at failure under conditions of
                  * hydrostatic tension
                  * This value must equal the corresponding PFRAC
                  * value in the FRACTS input set

* Johnson-Cook Viscoplastic Model for RHA (target layer 4)
 matep 5 JO RHA
 tmelt 1.0
 * Johnson-Cook Fracture Model for RHA (user defined)
   jfrac user
   jfd1 -1
   jfd2 1.25
   jfd3 -0.5
   jfd4 0.001
   jfd5 0.98
   jftm 0.155
   jfpf0 -1.5e+10 * pressure at failure under conditions of
                  * hydrostatic tension
                  * This value must equal the corresponding PFRAC
                  * value in the FRACTS input set

* Johnson-Cook Viscoplastic Model for RHA (target layer 5)
 matep 6 JO RHA
 tmelt 1.0
 * Johnson-Cook Fracture Model for RHA (user defined)
   jfrac user
   jfd1 -1
   jfd2 1.25
   jfd3 -0.5
```

```
      jfd4 0.001
      jfd5 0.98
      jftm 0.155
      jfpf0 -1.5e+10 * pressure at failure under conditions of
                     * hydrostatic tension
                     * This value must equal the corresponding PFRAC
                     * value in the FRACTS input set

   * Johnson-Cook Viscoplastic Model for RHA (target layer 6)
    matep 7 JO RHA
    tmelt 1.0
    * Johnson-Cook Fracture Model for RHA (user defined)
      jfrac user
      jfd1 -1
      jfd2 1.25
      jfd3 -0.5
      jfd4 0.001
      jfd5 0.98
      jftm 0.155
      jfpf0 -1.5e+10 * pressure at failure under conditions of
                     * hydrostatic tension
                     * This value must equal the corresponding PFRAC
                     * value in the FRACTS input set

* Boundary Layer Interface Algorithm
  blint 1   hard 1  soft 2  csl 1.5  cbl 1.5  fric 0
  blint 2   hard 1  soft 2  csl 1.5  cbl 1.5  fric 0
  blint 3   hard 1  soft 2  csl 1.5  cbl 1.5  fric 0
  blint 4   hard 1  soft 2  csl 1.5  cbl 1.5  fric 0
  blint 5   hard 1  soft 2  csl 1.5  cbl 1.5  fric 0
  blint 6   hard 1  soft 2  csl 1.5  cbl 1.5  fric 0
endepdata

* Adds Lagrangian tracer points that can be used to get
* time history data
tracer
  add  0.000   0.650
  add  0.000   1.300
  add  0.000   1.950
  add  0.000   2.600
  add  0.000   3.250
  add  0.000   3.900
  add  0.000   4.550
```

```
  add  0.000   5.200
  add  0.000   5.850
  add  0.000   6.500
  add  0.000   0.080
  add  0.000  -0.265
  add  0.000  -0.805
  add  0.000  -1.345
  add  0.000  -1.885
  add  0.000  -2.425
  add  0.000  -2.965
  add 10.000  -0.265
  add 10.000  -0.805
  add 10.000  -1.345
  add 10.000  -1.885
  add 10.000  -2.425
  add 10.000  -2.965
  add  0.000   0.000
  add  0.000  -3.230
  add 10.000   0.000
  add 10.000  -3.230
endtracer

************************************************************
*eor* cthin

Axisymmetric Impact: S7 Tool Steel on RHA, v=1380 m/s

control
  mmp3               * multiple material temperature and pressure model
  tstop=0.0004
  rdumpf 3600
  nscycle 55000
  ntbad 1e+09        * max number of thermodynamic warnings
  vis  bl 0.1  bq 2  * artificial viscosity
endcontrol

* Identifier for convection control input
Convct

 convection=0 * Convect internal energy using slope determined by
              * internal energy density and the slope of mass density,
              * discard kinetic energy discrepancy
```

```
 * High Resolution Interface Tracker
 interface=high_resolution * recommended for 2D in version 6

endconvct

* Identifier for fracture data
fracts

 pressure * uses pressure to calculate fractures
 * stress * uses stress to calculate fracture

fracts
  pressure
  pfrac1 -2e+10    * fracture pressure of S7 tool steel
  pfrac2 -1.5e+10  * fracture pressure of Rolled Homogeneous Armor
  pfrac3 -1.5e+10  * fracture pressure of Rolled Homogeneous Armor
  pfrac4 -1.5e+10  * fracture pressure of Rolled Homogeneous Armor
  pfrac5 -1.5e+10  * fracture pressure of Rolled Homogeneous Armor
  pfrac6 -1.5e+10  * fracture pressure of Rolled Homogeneous Armor
  pfrac7 -1.5e+10  * fracture pressure of Rolled Homogeneous Armor
  pfmix  -1e+20    * fracture pressure in mixed cells with no void
  pfvoid -1e+20    * fracture pressure in cells with with void
endfracts

edit

 * Identifier for short edits based on time frequency input
 shortt
   tim 0, dt = 1
 endshortt

 * Identifier for long edits based on time frequency input
 longt
   tim 0, dt = 1
 endlongt

 * Identifier for plot dumps based on time frequency input
 plott
   tim 0, dt = 4e-06
 endplott

 * Identifier for material history edits based on time frequency input
 histt
```

```
   tim 0, dt = 1e-07
   htracer all
 endhistt

endedit

boundary
 bhydro * hydrodynamic boundary conditions
   block 1

     * 0 boundary condition is a symmetry condition.
     * 2 boundary condition allows mass to leave mesh
     * but no mass can enter the mesh.  This is useful for
     * letting parts of the problem flow out of the mesh

     bxbot = 0 * boundary condition at bottom of x mesh
               * (x=0 for axisymmetric model)
     bxtop = 2 * boundary condition at top of x mesh
     bybot = 2 * boundary condition at bottom of y mesh
     bytop = 2 * boundary condition at top of y mesh

    endblock
  endhydro
endboundary
```

A.2 Confined Ceramic Target Example

```
*eor* genin

Axisymmetric Impact: W ---> B4C + 4340 Steel, v=1454 m/s

*An asterisk "*" is used to comment out a line

control
 mmp
 ep
endcontrol

mesh
* Define the mesh for the problem

 block 1 geom=2dc type=e
 * 2dc is two-dimensional cylindrical geometry
```

```
 * e is Eulerian mesh

    x0=0 * smallest value of X coordinate for mesh

    * n is number of cells,
    * w is width of the total region
    * dxf is the width of the first cell in this region
    * dxl is the width of the last cell in this region
      x1  w=0.20  dxf=0.010  dxl=0.010
      x2  w=0.95  dxf=0.010  dxl=0.050

    endx

    y0=-4.76 * smallest value of Y coordinate for mesh

    * The format is the same as for the X records
      y1  w=2.400   dyf=0.100  dyl=0.050
      y2  w=1.350   dyf=0.050  dyl=0.010
      y3  w=2.010   dyf=0.010  dyl=0.010
      y4  w=14.000  dyf=0.010  dyl=0.050

    endy

   * Define the upper and lower bouns of the active X & Y mesh
   xaction=0,0.2
   yaction=-1.0,15

 endblock
endmesh

insertion of material
* Required identifier to insert the materials

 block 1

 * model half of the projectile and target and then
 * mirror results in cthplt file

   * Define projectile materials, geometry and velocity
   package projectile shaft
     material 1
     numsub 50
     yvel -145400
```

```
    insert box
      p1     0        0
      p2     0.1     15
    endinsert
  endpackage

  * Define target materials and geometry
  package target 1 * ceramic layer
    material 2
    numsub 50
    insert box
      p1        0    -4.36
      p2       0.95   -0.4
    endinsert
  endpackage

  * Two materials cannot exist in the same space.
  * The material that is identified first will exist
  * where any overlaps take place.
  package target 2 * metallic layers
    material 3
    numsub 50
    insert box
      p1        0    -4.76
      p2       1.15    0
    endinsert
  endpackage

 endblock
endinsertion

edit
 block 1
   expanded
 endblock
endedit

eos * Define the Equation of State for the materials

 * SESAME Model for Tungsten
 MAT1 SES TUNGSTEN

 * Johnson-Holmquist 2 Ceramic Model for Boron Carbide
```

```
 MAT2 JHCR2 B4C

 * PTRAN EOS for Iron (models phase transition that occurs in
 * Iron under shock loading of 13 GPa)
 * Iron EOS is very close to EOS for Steel
 MAT3 PTRAN IRON
endeos

* Define the constitutive models for the materials
epdata * Elastic Plastic data
 vpsave
 mix 3  * mix 3 = normalized vol avg yeild strength

   * Johnson-Cook Viscoplastic Model for Tungsten
     matep 1 JO TUNGSTEN
     tmelt 1.0
   * Johnson-Cook Fracture Model for Tungsten (user defined)
     jfrac user
     jfd1 0.00
     jfd2 3.3e-01
     jfd3 -1.50
     jfd4 0.00
     jfd5 0.00
     jftm 1.506247E-01
     jfpf0 -2.0e+10 * pressure at failure under conditions of
                    * hydrostatic tension
                    * This value must equal the corresponding PFRAC
                    * value in the FRACTS input set

   * Johnson-Holmquist 2 Ceramic Model for Boron Carbide
     matep 2 JHCR2 B4C

   * Johnson-Cook Viscoplastic Model for 4340 Steel
     matep 3 JO 4340_TEMP_MART
     tmelt 1.0
   * Johnson-Cook Fracture Model for Steel
     jfrac steel
     jfpf0 -2e+10 * pressure at failure under conditions of
                  * hydrostatic tension
                  * This value must equal the corresponding PFRAC
                  * value in the FRACTS input set

   * Boundary Layer Interface Algorithm
```

```
   *blint 1   hard 1  soft 2  csl 1.5  cbl 1.5  fric 0 corr
   *blint 2   hard 1  soft 3  csl 1.5  cbl 1.5  fric 0 corr

endepdata

* Adds Lagrangian tracer points that can be used to get
* time history data
tracer
 add  0.000   0.000
 add  0.000   5.000
 add  0.000   10.00
 add  0.000   15.00
 add  0.000   0.100
 add  0.000  -0.200
 add  0.000  -0.400
 add  0.000  -1.390
 add  0.000  -2.380
 add  0.000  -3.370
 add  0.000  -4.360
 add  0.000  -4.560
 add  0.000  -4.760
 add  0.475  -0.200
 add  0.475  -0.400
 add  0.475  -1.390
 add  0.475  -2.380
 add  0.475  -3.370
 add  0.475  -4.360
 add  0.475  -4.560
 add  0.475  -4.760
 add  1.050  -0.200
 add  1.050  -0.400
 add  1.050  -1.390
 add  1.050  -2.380
 add  1.050  -3.370
 add  1.050  -4.360
 add  1.050  -4.560
 add  1.050  -4.760
endtracer

************************************************************
*eor* cthin

Axisymmetric Impact: W ---> B4C + 4340 Steel, v=1454 m/s
```

```
control
 mmp3 * multiple material temperature and pressure model
 tstop=0.0002
 rdumpf 3600
 nscycle 75000
 ntbad 1e+09 * max number of thermodynamic warnings
endcontrol

* Identifier for convection control input
Convct

 convection=0 * Convect internal energy using slope determined by
              * internal energy density and the slope of mass density,
              * discard kinetic energy discrepancy

 * High Resolution Interface Tracker
 interface=high_resolution * recommended for 2D in version 6

endconvct

* Identifier for fracture data
fracts

 pressure * uses pressure to calculate fractures
 * stress * uses stress to calculate fracture

 pfrac1 -2e+10 * fracture pressure of Tungsten
 pfrac2 -0.26e+10 * fracture pressure of Boron Carbide
 pfrac3 -2e+10 * fracture pressure of 4340 Steel
 pfmix  -1e+20 * fracture pressure in mixed cells with no void
 pfvoid -1e+20 * fracture pressure in cells with with void

endfracts

edit

 * Identifier for short edits based on time frequency input
 shortt
   tim 0, dt = 1
 endshortt

 * Identifier for long edits based on time frequency input
```

```
 longt
   tim 0, dt = 1
 endlongt

 * Identifier for plot dumps based on time frequency input
 plott
   tim 0, dt = 2e-06
 endplott

 * Identifier for material history edits based on time frequency input
 histt
   tim 0, dt = 1e-07
   htracer all
 endhistt

endedit

boundary
 bhydro * hydrodynamic boundary conditions
   block 1

     * 0 boundary condition is a symmetry condition.
     * 2 boundary condition allows mass to leave mesh
     * but no mass can enter the mesh.  This is useful for
     * letting parts of the problem flow out of the mesh

     bxbot = 0 * boundary condition at bottom of x mesh
               * (x=0 for axisymmetric model)
     bxtop = 2 * boundary condition at top of x mesh
     bybot = 2 * boundary condition at bottom of y mesh
     bytop = 2 * boundary condition at top of y mesh

   endblock
 endhydro
endboundary
```

A.3 Ceramic Armor

```
*eor* genin

Axisymmetric Impact: S7 Tool Steel ---> B4C + RHA, v=1000 m/s
```

```
*An asterisk "*" is used to comment out a line

control
 mmp
 ep
endcontrol

mesh
* Define the mesh for the problem

 block 1 geom=2dc type=e
 * 2dc is two-dimensional cylindrical geometry
 * e is Eulerian mesh

    x0=0 * smallest value of X coordinate for mesh

    * n is number of cells,
    * w is width of the total region
    * dxf is the width of the first cell in this region
    * dxl is the width of the last cell in this region
      x1  w=1.30  dxf=0.01  dxl=0.01
      x2  w=8.70  dxf=0.01  dxl=0.05
      x3  w=2.60  dxf=0.05  dxl=0.10

    endx

    y0=-7.18 * smallest value of Y coordinate for mesh

    * The format is the same as for the X records
      y1  w=4.000  dyf=0.10  dyl=0.05
      y2  w=1.880  dyf=0.05  dyl=0.01
      y3  w=2.600  dyf=0.01  dyl=0.01
      y4  w=6.200  dyf=0.01  dyl=0.05

    endy

   * Define the upper and lower bouns of the active X & Y mesh
   xaction=0,0.65
   yaction=-0.53,7.5

 endblock
endmesh
```

```
insertion of material
* Required identifier to insert the materials

 block 1
 * model half of the projectile and target and then
 * mirror results in cthplt file

   * Define projectile materials, geometry and velocity
   package projectile shaft
     material 1
     numsub 50
     yvel -100000
     insert box
       p1        0     0.65
       p2     0.65      6.5
     endinsert
   endpackage

   package projectile tip * hemispherical tip
     material 1
     numsub 50
     yvel -100000
     insert circle
       center 0    0.65
       radius 0.65
     endinsert
   endpackage

   * Define target materials and geometry
   package target 1 * ceramic layer
     material 2
     numsub 50
     insert box
       p1        0    -1.06
       p2       10    -0.53
     endinsert
   endpackage

   * Two materials cannot exist in the same space.
   * The material that is identified first will exist
   * where any overlaps take place.
   package target 2 * metallic layers
     material 3
```

```
     numsub 50
     insert box
       p1        0    -3.18
       p2       12.6    0
     endinsert
   endpackage

 endblock
endinsertion

edit
 block 1
   expanded
 endblock
endedit

eos * Define the Equation of State for the materials

 * PTRAN EOS for Iron (models phase transition that occurs in
 * Iron under shock loading of 13 GPa)
 * Iron EOS is very close to EOS for Steel
 MAT1 PTRAN IRON

 * Johnson-Holmquist 2 Ceramic Model for Boron Carbide
 MAT2 JHCR2 B4C

 * PTRAN EOS for Iron (models phase transition that occurs in
 * Iron under shock loading of 13 GPa)
 * Iron EOS is very close to EOS for Steel
 MAT3 PTRAN IRON
endeos

* Define the constitutive models for the materials
epdata * Elastic Plastic data
 vpsave
 mix 3  * mix 3 = normalized vol avg yeild strength

   * Johnson-Cook Viscoplastic Model for S7 Tool Steel
   matep 1 JO S7_TOOL_STEEL
   tmelt 1.0
   * Johnson-Cook Fracture Model for Steel
     jfrac steel
     jfpf0 -2e+10 * pressure at failure under conditions of
```

```
                    * hydrostatic tension
                    * This value must equal the corresponding PFRAC
                    * value in the FRACTS input set

   * Johnson-Holmquist 2 Ceramic Model for Boron Carbide
   matep 2 JHCR2 B4C

   * Johnson-Cook Viscoplastic Model for Rolled Homogeneous Armor
   matep 3 JO RHA
   tmelt 1.0
   * Johnson-Cook Fracture Model
     jfrac user
     jfd1 -1
     jfd2 1.25
     jfd3 -0.5
     jfd4 0.001
     jfd5 0.98
     jftm 0.155
     jfpf0 -1.5e+10 * pressure at failure under conditions of
                    * hydrostatic tension
                    * This value must equal the corresponding PFRAC
                    * value in the FRACTS input set

   * Boundary Layer Interface Algorithm
   blint 1   hard 1  soft 2  csl 1.5  cbl 1.5  fric 0 corr
   blint 2   hard 1  soft 3  csl 1.5  cbl 1.5  fric 0 corr
endepdata

* Adds Lagrangian tracer points that can be used to get
* time history data
tracer
 add  0.000   0.650
 add  0.000   1.300
 add  0.000   1.950
 add  0.000   2.600
 add  0.000   3.250
 add  0.000   3.900
 add  0.000   4.550
 add  0.000   5.200
 add  0.000   5.850
 add  0.000   6.500
 add  0.000   0.080
 add  0.000  -0.265
```

```
 add  0.000  -0.795
 add  0.000  -1.325
 add  0.000  -1.855
 add  0.000  -2.385
 add  0.000  -2.915
 add  5.000  -0.265
 add  5.000  -0.795
 add  5.000  -1.325
 add  5.000  -1.855
 add  5.000  -2.385
 add  5.000  -2.915
 add 10.000  -0.265
 add 10.000  -0.795
 add 10.000  -1.325
 add 10.000  -1.855
 add 10.000  -2.385
 add 10.000  -2.915
 add  0.000   0.000
 add  0.000  -3.180
 add 10.000   0.000
 add 10.000  -3.180
endtracer

************************************************************
*eor* cthin

Axisymmetric Impact: S7 Tool Steel ---> B4C + RHA, v=1000 m/s

control
 mmp3 * multiple material temperature and pressure model
 tstop=0.0003
 rdumpf 3600
 nscycle 75000
 ntbad 1e+09 * max number of thermodynamic warnings
endcontrol


* Identifier for convection control input
Convct

 convection=0 * Convect internal energy using slope determined by
              * internal energy density and the slope of mass density,
              * discard kinetic energy discrepancy
```

```
 * High Resolution Interface Tracker
 interface=high_resolution * recommended for 2D in version 6

endconvct

* Identifier for fracture data
fracts

 pressure * uses pressure to calculate fractures
 * stress * uses stress to calculate fracture

 pfrac1 -2e+10 * fracture pressure of S7 tool steel
 pfrac2 -0.26e+10 * fracture pressure of Boron Carbide
 pfrac3 -1.5e+10 * fracture pressure of Rolled Homogeneous Armor
 pfmix  -1e+20 * fracture pressure in mixed cells with no void
 pfvoid -1e+20 * fracture pressure in cells with with void

endfracts

edit

 * Identifier for short edits based on time frequency input
 shortt
   tim 0, dt = 1
 endshortt

 * Identifier for long edits based on time frequency input
 longt
   tim 0, dt = 1
 endlongt

 * Identifier for plot dumps based on time frequency input
 plott
   tim 0, dt = 3e-06
 endplott

 * Identifier for material history edits based on time frequency input
 histt
   tim 0, dt = 1e-07
   htracer all
 endhistt
```

```
endedit

boundary
 bhydro * hydrodynamic boundary conditions
   block 1

     * 0 boundary condition is a symmetry condition.
     * 2 boundary condition allows mass to leave mesh
     * but no mass can enter the mesh.  This is useful for
     * letting parts of the problem flow out of the mesh

     bxbot = 0 * boundary condition at bottom of x mesh
               * (x=0 for axisymmetric model)
     bxtop = 2 * boundary condition at top of x mesh
     bybot = 2 * boundary condition at bottom of y mesh
     bytop = 2 * boundary condition at top of y mesh

   endblock
 endhydro
endboundary
```

Appendix B. CTH Post-processing File

This appendix includes two sample CTH post-processing files. The first on is a sample CTHPLT file for making contour plots of the material impact and pressure. The second is a sample HISPLT for making history plots of the position, velocity and pressure for certain tracer points.

B.1 Sample Contour Plot

```
*eor* pltin

units,cgsk
noid

*Set viewing area
limit x=0, 12.6 y=-7.26, 6.5

* Color - White background for printing, thesis plots
COLOR, FG=0, SFG=0, BG = 7, IBGROUND=7, FRAME=0, TRACERS=0, IF=0*Material Plots

*Material Plots
all
title Material Impact
material 'Projectile', 'Ceramic', 'Metallic'
color table 4
color mat = 8,26,17
color voids = -1
flegend=m,c
2dplot if mat tr mirror

************************************************
*Pressure
all
title Pressure
flegend=b
color table 5
rbands, b1=-2e+10, b2=3e+10, c1=84, c2=33, skip=1
2dplot if bands = pressure mirror
```

B.2 Sample History Plot

```
*eor* hisin
```

```
*fonts, 11,12,3,13
*nocolor
noid
*TCOLOR
text=0
color, foreground=0 ,text=0, background=7 , logo=0 , interior=7

************************************************
* Position

*title, Projectile Tip x Position, Tracer = 11
*plot time xposition.11
title, Projectile Tip y Position, Tracer = 11
plot time yposition.11

*title, Impact Region x Position, Tracer = 30
*plot time xposition.30
title, Impact Region y Position, Tracer = 30
plot time yposition.30

************************************************
* Velocity

*title, Projectile Tip x Velocity, Tracer = 11
*plot time xvelocity.11
title, Projectile Tip y Velocity, Tracer = 11
plot time yvelocity.11

*title, Impact Region x Velocity, Tracer = 30
*plot time xvelocity.30
title, Impact Region y Velocity, Tracer = 30
plot time yvelocity.30

************************************************
* Pressure

title, Projectile Tip Pressure, Tracer = 11
plot time pressure.11

title, Impact Region Pressure, Tracer = 30
plot time pressure.30
```

Bibliography

1. Anderson, C. E. "An Overview of the Theory of Hydrocodes". *International Journal of Impact Engineering*, 5:33–59, 1987.

2. Backman, M. E. *Terminal Ballistics*. Technical report, Naval Weapons Center, 1976. NWC TP 578.

3. Backman, M. E. and W. Goldsmith. "The Mechanics of Penetration of Projectiles into Targets". *International Journal of Engineering Science*, 16:1–99, 1978.

4. Bedford, A. and D. S. Drumheller. *Elastic Wave Propagation*. John Wiley & Sons, New York, 1994.

5. Benson, D. J. "Computational Methods in Lagrangian and Eulerian Hydrocodes". *Computer Methods in Applied Mechanics and Engineering*, 99:235–394, 1992.

6. Bowden, F. P. and E. H. Freitag. "The Friction of Solids at Very High Speeds". *Proceedings of the Royal Society*, volume 248, 350–367. London, 1958.

7. Chocron, I. S., C. E. Anderson Jr., T. Behner, and V. Hohler. "Lateral Confinement Effects in Long-rod Penetration of Ceramics at Hypervelocity". *International Journal of Impact Engineering*, 33:169–179, 2006.

8. Crawford, D. *CTH Course Notes*. Sandia National Laboratories, Albuquerque, NM, May 2006.

9. Crawford, D. *Alternative Methods of Meshing and Equation of State Options in CTH*. Sandia National Laboratories, 2008. Personal correspondence.

10. Drumheller, D. S. *Introduction to Wave Propagation in Nonlinear Fluids and Solids*. Cambridge University Press, Cambridge, 1998.

11. Gazonas, G. A. "Implementation of the Johnson-Holmquist II (JH-2) Constitutive Model Into DYNA3D", March 2002. Army Research Laboratory, ARL-TR-2699.

12. Goldsmith, W. *Impact: The Theory and Physical Behaviour of Colliding Solids*. Edward Arnold, Ltd., London, 1960.

13. Grace, F. I. and N. L. Rupert. "Analysis of Long Rods Impacting Ceramic Targets at High Velocity". *International Journal of Impact Engineering*, 20:281–292, 1997.

14. Gupta, N. K. and V. Madhu. "An Experimental Study of Normal and Oblique Impact of Hard-core Projectile on Single and Layered Plates". *International Journal of Impact Engineering*, 19:395–414, 1997.

15. Hertel, E. S. and et al. "CTH: A Software Family for Multi-Dimensional Shock Physics Analysis". *Proceedings of the 19th International Symposium on Shock Waves*, July 1993.

16. Hertel, E. S. and G. I. Kerley. *CTH Reference Manual: The Equation of State Package*. Sandia National Laboratories, Albuquerque, NM, April 1998.

17. Hertel, E. S. and G. I. Kerley. *Recent Improvements to the CTH EOS Package*. Sandia National Laboratories, Albuquerque, NM, September 1999.

18. Holmquist, T. J., D. W. Templeton, and K. D. Bishnoi. "Constitutive Modeling of Aluminum Nitride for Large Strain, High-strain Rate, and High-pressure Applications". *International Journal of Impact Engineering*, 25:211–231, 2001.

19. Johnson, W., A. K. Sengupta, S. K. Ghosh, and S. R. Reid. "Mechanics of High Speed Impact at Normal Incidence between Plasticine Long Rods and Plates". *Journal of the Mechanics and Physics of Solids,*, 29:413–445, 1981.

20. Laird, D. J. *The Investigation of Hypervelocity Gouging*. Ph.D. thesis, Graduate School of Engineering, Air Force Institute of Technology (AETC), March 2002. AFIT/DS/ENY/02-01.

21. Lynch, N. J., S. J. Bless, I. G. Cullis, and D. Berry. "The Influence of Confinement on the Penetration of Ceramic Targets by KE Projectiles at 1.8 and 2.6 km/s". *International Journal of Impact Engineering*, 33:390–401, 2006.

22. McGlaun, J. M., S. L. Thompson, and M. G. Elrick. "CTH: A Three-Dimensional Shock Wave Physics Code". *International Journal of Impact Engineering*, 10:351–360, 1990.

23. McGlaun, M. *CTH Reference Manual: Lagrangian Step for Hydrodynamic Materials*. Sandia National Laboratories, Albuquerque, NM, December 1990. SAND90-2645.

24. Meyers, M. A. *Dynamic Behavior of Materials*. John Wiley & Sons, Inc., New York, 1994.

25. Nguyen, M. C. *Analysis of Computational Methods for the Treatment of Material Interfaces*. Master's thesis, Graduate School of Engineering, Air Force Institute of Technology (AETC), March 2005. AFIT/GAE/ENY/05-M15.

26. Nicholas, T. *Impact Dynamics*, chapter 4 Elastic-Plastic Stress Waves. John Wiley & Sons, Inc., New York, 1982.

27. Nicholas, T. and A. M. Rajendran. *High Velocity Impact Dynamics*, chapter 3 Material Characterization at High Strain Rates. John Wiley & Sons, Inc., New York, 1990.

28. Nicholas, T. and R. F. Recht. *High Velocity Impact Dynamics*, chapter 1 Introduction to Impact Phenomena. John Wiley & Sons, Inc., New York, 1990.

29. Orphal, D. L., R. R. Franzen, A.C. Charters, T. L. Menna, and A. J. Piekutowski. "Penetration of Confined Boron Carbide Targets by Tungsten Long Rods at Impact Velocities from 1.5-5.0 km/s". *International Journal of Impact Engineering*, 19:15–29, 1997.

30. Orphal, D. L., R. R. Franzen, A. J. Piekutowski, and M. J. Forrestal. "Penetration of Confined Aluminum Nitride Targets by Tungsten Long Rods at 1.5-4.5 km/s". *International Journal of Impact Engineering*, 18:355–368, 1996.

31. Quan, X., R. A. Clegg, M. S. Cowler, N. K. Birnbaum, and C. J. Hayhurst. "Numerical Simulation of Long Rods Impacting Silicon Carbide Targets Using JH-1 Model". *International Journal of Impact Engineering*, 33:634–644, 2006.

32. R. L. Bell, et al. *CTH User's Manual and Input Instructions*. Sandia National Laboratories, Albuquerque, NM, July 2003.

33. R. L. Bell, et al. *CTHGEN User's Manual and Input Instructions*. Sandia National Laboratories, Albuquerque, NM, July 2003.

34. Rajendran, A. M. and D. J. Grove. "Modeling the Shock Response of Silicon Carbide, Boron Carbide, and Titanium Diboride". *International Journal of Impact Engineering*, 18:611–631, 1996.

35. Rickerd, G. S. *An Investigation of a Simplified Gouging Model*. Master's thesis, Graduate School of Engineering, Air Force Institute of Technology (AETC), March 2005. AFIT/GAE/ENY/05-M19.

36. Rosenberg, Z. and E. Dekel. "The Relation between the Penetration Capability of Long Rods and Their Length to Diameter Ratio". *International Journal of Impact Engineering*, 15:125–129, 1994.

37. Rosenberg, Z. and E. Dekel. "On the Role of Nose Profile in Long-rod Penetration". *International Journal of Impact Engineering*, 22:551–557, 19979.

38. Rosenberg, Z. and E. Dekel. "A Computational Study of the Relations between Material Properties of Long-rod Penetrators and Their Ballistic Performance". *International Journal of Impact Engineering*, 21:283–296, 1998.

39. Rosenberg, Z. and E. Dekel. "More on Secondary Penetration of Long Rods". *International Journal of Impact Engineering*, 26:639–649, 2001.

40. Rosenberg, Z., E. Dekel, V. Hohler, A. J. Stilp, and K. Weber. "Hypervelocity Penetration of Tungsten Alloy Rods into Ceramic Tiles: Experiments and 2-D Simulations". *International Journal of Impact Engineering*, 20:675–683, 1997.

41. Silling, S. A. *CTH Reference Manual: Boundary Layer Algorithm for Sliding Interfaces in Two Dimensions*. Sandia National Laboratories, Albuquerque, NM, September 1995.

42. Silling, S. A. *CTH Reference Manual: Johnson-Holmquist Ceramic Model*. Sandia National Laboratories, Albuquerque, NM, June 1996.

43. Silling, S. A. *CTH Reference Manual: Viscoplastic Models*. Sandia National Laboratories, Albuquerque, NM, June 1996.

44. Silling, S. A. *Use of the Johnson-Cook Fracture Model in CTH*. Sandia National Laboratories, Albuquerque, NM, June 1996.

45. Silling, S. A. *Use of the Johnson-Holmquist 2 Model in CTH.* Sandia National Laboratories, Albuquerque, NM, June 1996.

46. Subramanian, R. and S. J. Bless. "Penetration of Semi-infinite AD995 Alumina Targets by Tungsten Long Rod Penetrators from 1.5 to 3.5 km/s". *International Journal of Impact Engineering*, 17:807–816, 1995.

47. Szmerekovsky, A. G. *The Physical Understanding of the Use of Coatings to Mitigate Hypervelocity Gouging Considering Real Test Sled Dimensions.* Ph.D. thesis, Graduate School of Engineering, Air Force Institute of Technology (AETC), September 2004. AFIT/DS/ENY/04-06.

48. Tedesco, J. W. and D. W. Landis. "Wave Propagation Through Layered Systems". *Computers & Structures*, 32(3/4):625–638, 1989.

49. Westerling, L., P. Lundberg, and B. Lundberg. "Tungsten Long-rod Penetration into Confined Cylinders of Boron Carbide at and Above Ordnance Velocities". *International Journal of Impact Engineering*, 25:703–714, 2001.

50. Woods, R. D. "Screening of Surface Waves in Solids". *Journal of the Soils Mechanics and Foundations Division of the American Society of Civil Engineers*, 94:951–979, 1968.

51. Wright, T. W. *A Survey of Penetration Mechanics for Long Rods.* Technical report, Ballistic Research Laboratory, 1983. ARBRL-TR-02496.

52. Zukas, J. A. *Impact Dynamics*, chapter 5 Penetration and Perforation of Solids. John Wiley & Sons, Inc., New York, 1982.

53. Zukas, J. A. *High Velocity Impact Dynamics*, chapter 9 Survey of Computer Codes for Impact Solution. John Wiley & Sons, Inc., New York, 1990.

54. Zukas, J. A. *High Velocity Impact Dynamics*, chapter 4 Introduction to Penetration Mechanics. John Wiley & Sons, Inc., New York, 1990.

55. Zukas, J. A. *Introduction to Hydrocodes*, volume 49. Elsevier, New York, 2004.

56. Zukas, J. A. and D. R. Scheffler. "Impact Effects in Multilayered Plates". *International Journal of Solids and Structures*, 38:3321–3328, 2001.

Vita

Capt Jason K. Lee graduated from Cedar Hill High School in Cedar Hill, Texas in 1997. He then graduated from Tarrant County Junior College in Arlington, Texas with his Associate of Arts degree in 1999. He followed that up by entering undergraduate studies at the University of Texas at Arlington where he graduated with a Bachelor of Science degree in Aerospace Engineering in 2003.

He was commissioned into the United States Air Force through the Officer Training School at Maxwell AFB in Montgomery, Alabama in September 2003. His first assignment was to Hill AFB, where he designed aircraft repairs as a structural engineer in the Mature and Proven Aircraft Directorate (later reorganized under the 508th Aircraft Sustainment Wing). While at Hill AFB, he also served as an Aircraft Battle Damage Repair Engineer. In August of 2006, he entered the Graduate School of Engineering at the Air Force Institute of Technology. Upon graduation, he will be assigned to the Munitions Directorate of AFRL.

REPORT DOCUMENTATION PAGE

Form Approved
OMB No. 0704–0188

1. REPORT DATE (DD–MM–YYYY)	2. REPORT TYPE	3. DATES COVERED *(From — To)*
17–03–2008	Master's Thesis	Mar 2007 — Mar 2008

4. TITLE AND SUBTITLE

Analysis of Multi-Layered Materials Under High Velocity Impact Using CTH

5a. CONTRACT NUMBER

5b. GRANT NUMBER

5c. PROGRAM ELEMENT NUMBER

6. AUTHOR(S)

Jason K. Lee, Capt, USAF

5d. PROJECT NUMBER

5e. TASK NUMBER

5f. WORK UNIT NUMBER

7. PERFORMING ORGANIZATION NAME(S) AND ADDRESS(ES)

Air Force Institute of Technology
Graduate School of Engineering and Management (AFIT/EN)
2950 Hobson Way
WPAFB OH 45433-7765

8. PERFORMING ORGANIZATION REPORT NUMBER

AFIT/GAE/ENY/08-M19

9. SPONSORING / MONITORING AGENCY NAME(S) AND ADDRESS(ES)

Kirk Vanden, PhD
AFRL/RWAC
101 W. Eglin Blvd Suite #337
Eglin AFB, 32542-6810

10. SPONSOR/MONITOR'S ACRONYM(S)

11. SPONSOR/MONITOR'S REPORT NUMBER(S)

12. DISTRIBUTION / AVAILABILITY STATEMENT

APPROVED FOR PUBLIC RELEASE; DISTRIBUTION UNLIMITED

13. SUPPLEMENTARY NOTES

14. ABSTRACT

Multi-layer armor containing ceramic and metallic layers has become more common in the past two decades. Typically, ceramics have high compressive strength; that feature combined with their low density make them highly desirable for armor applications. This research effort numerically simulates ballistic impact of a cylindrical penetrator with a hemispherical tip on a multi-layer metallic and ceramic targets of finite thickness. The projectile is made of S7 tool steel, while the target consists of rolled homogenous armor and boron carbide ceramic. The Eulerian hydrocode CTH, ideal for studying cases of gross global and local deformation, is used to perform an axisymmetric analysis of the projectile and the target. The Johnson-Holmquist constitutive model (JH-2) for brittle materials is used for the ceramic layers, and the Johnson-Cook constitutive model is used for the metallic layers. Various arrangements of ceramic and metallic layers were simulated over a range of velocities to quantitatively determine ballistic limits. Comparison of the ballistic limits for each configuration will determine which ceramic-metal lay-up arrangement is optimal for resisting penetration of the given projectile. This research shows that replacing multiple metallic target layers with B4C ceramic decreases the resistance of the target to the penetration of the projectile for a target of given thickness.

15. SUBJECT TERMS

High Velocity Impact, Ballistic Limit, CTH, Johnson-Holmquist II (JH-2) Constitutive Model, Boron Carbide, Ceramic Target, Ceramic Armor

16. SECURITY CLASSIFICATION OF:			17. LIMITATION OF ABSTRACT	18. NUMBER OF PAGES	19a. NAME OF RESPONSIBLE PERSON
a. REPORT	b. ABSTRACT	c. THIS PAGE			Dr. Anthony N. Palazotto
U	U	U	UU	198	19b. TELEPHONE NUMBER (Include Area Code) (937) 255-3636, ext 4599; e-mail: Anothony.Palazotto@afit.edu